STRUCTURAL AND FUNCTIONAL INSIGHTS INTO THE CITRATE TRANSPORTER SECITS

Dissertation

zur Erlangung des Doktorgrades

der Naturwissenschaften

vorgelegt beim Fachbereich

Biochemie, Chemie und Pharmazie (FB14)

der Johann Wolfgang Goethe-Universität

in Frankfurt am Main

von

Maria Johanna Grötzinger

aus Berlin

Frankfurt am Main, 2022

(D 30)

Vom Fachbereich Biochemie, Chemie und Pharmazie (FB 14)
der Goethe-Universität als Dissertation angenommen.

Dekan:	Prof. Dr. Clemens Glaubitz
Gutachter:	Prof. Dr. Volker Dötsch
	Prof. Dr. Werner Kühlbrandt

Datum der Disputation: 20.12.2022

Du wirst noch viel erleben.

Du musst diesen Test bestehen.

Es kommt der Tag, an dem du dein Ziel erreichst!

ZUSAMMENFASSUNG

Membranproteine sind eine vielfältige Gruppe von Proteinen, deren Aufgaben verschiedenster Natur sein können. Eine der wichtigsten Funktionen stellt der Transport über die biologische Membran dar. Ganz unterschiedliche Substrate werden mit Hilfe von speziellen Proteinen von einer Seite der hydrophoben Barriere, die durch die zelluläre oder organellare Membran gebildet wird, auf die andere überführt. Dabei verläuft der Transport mit oder auch aktiv gegen den Konzentrationsgradienten des Substrats. Innerhalb der aktiv transportierenden Proteine gibt es eine Gruppe verschiedener Proteine, die einen bestehenden elektro-chemischen Gradienten ausnutzen, um den Transport ihres Hauptsubstrats gegen dessen Konzentrationsgradienten zu ermöglichen. Diese sogenannten sekundär-aktiven Transporter sind eine Gruppe von integralen Membranproteinen, die in allen Zellen und Domänen des Lebens zu finden sind. Sie ermöglichen den Transport von einer Vielzahl von Substraten wie Nährstoffen, Ionen, Metaboliten und anderen Verbindungen, z. B. Medikamenten, über die Membranbarriere. Als Hauptantriebskraft für die meisten Transporter dient der elektrochemische Gradient von entweder Natriumionen oder Protonen, obwohl einige Transporter auch das Potenzial anderer Ionen oder organischer Verbindungen nutzen. Beispielsweise im Falle von Austauschproteinen werden zwei sehr ähnliche Substrate in entgegengesetzter Richtung über die Membran transportiert, das eine gegen seinen elektrochemischen Gradienten, angetrieben durch den Gradienten des anderen Substrates.

Mit der strukturellen Vielfalt der Transporter hinsichtlich der allgemeinen Form, der Oligomerisierung und der Anzahl an Transmembranelementen geht eine mechanistische Vielfalt einher, die jedoch immer nach dem Prinzip der alternierenden Zugänglichkeit erfolgt. Beim Menschen kann die Fehlfunktion von sekundär-aktiven Transportern zu verschiedenen physiologischen Störung wie Epilepsie, Depression oder Adipositas führen.

Der Fokus der vorliegenden Arbeit lag auf der strukturellen und funktionellen Charakterisierung des sekundär-aktiven Transporters SeCitS aus *Salmonella enterica*, einem Symporter der 2-Hydroxycarboxylat-Familie. Der Transport von Citrat als bivalentes Anion wird durch den Cotransport mit Natrium-Ionen ermöglicht, die einen nach innen gerichteten Gradienten über die innere Membran der Salmonellen aufweisen. Transportexperimente

zeigten, dass das Verhältnis der Substrate zwei Natriumionen pro Citratmolekül beträgt, was einen elektroneutralen Transport bedeutet. Im Vergleich zu anderen Mitgliedern der Familie gibt es eine sehr hohe Spezifität des Transporters gegenüber seinem Hauptsubstrat.

Strukturelle Informationen über das Protein wurden zunächst durch 2D-Elektronenkristallographie gewonnen, was die Identifizierung eines ovalen Dimers ermöglichte und erste Hinweise auf eine signifikante Konformationsänderung gab, die das Protein während seines Transportzyklus durchläuft. Mittels 3D-Kristallographie konnte die Röntgenstruktur des Transporters gelöst werden. Das Protein kristallisierte als stabiles, aber konformationell asymmetrisches Dimer. In beiden Protomeren kann gebundenes Citrat leicht identifiziert werden. Sie lassen sich in eine nach außen und eine nach innen gerichtete Konformation anhand der Zugänglichkeit der Citrate zuordnen, wobei die Hauptbindestelle für Citrat in der nach außen gerichteten Konformation liegt.

Die Proteinstruktur zeichnet sich durch eine große Oberfläche aus, die für die Multimerisierung zur Verfügung steht und eine Plattform für eine stabile Dimerisierung der beiden Protomere bietet. Interessanterweise zeigt SeCitS aber keine echte Kooperativität beim Transport seiner Substrate. Unter Berücksichtigung dieser beiden Aspekte stellte sich die Frage, ob eine mögliche gegenseitige Beeinflussung zwischen den Monomeren innerhalb des Dimers stattfindet und den Transport (potentielle negative Kooperativität) oder die Konformationsverteilung innerhalb des Dimers (potentielle Stabilisierung des Proteins innerhalb der Membran) beeinflusst.

Der Ansatz zur funktionellen Beantwortung dieser Frage war die Verwendung von mutierten Varianten des Proteins, die eine Quervernetzung innerhalb eines Monomers erlauben. Es wurden jeweils zwei Seitenketten ausgewählt, die kreuzvernetzt jeweils eine der beiden Konformationen blockieren würde, um die Transportaktivität im verbleibenden Protomer testen zu können. Die hierfür geeigneten Seitenketten wurden anhand der Kristallstruktur abgeleitet (D112 - R205 zum Sperren der nach innen gerichteten Konformation und L337 - S412 für die nach außen gerichtete Konformation). Nach anfänglich vielversprechenden Ergebnissen waren die endgültigen Varianten nicht stabil genug, um in Transporttests analysiert zu werden.

Um die Verteilung der relativen Konformationen innerhalb des Dimers zu analysieren, wurde das Protein in eine möglichst natürliche Lipidumgebung wie Nanodiscs oder Saposin-

Nanopartikel rekonstituiert und mittels Kryo-Elektronenmikroskopie untersucht. Die ersten Bilder ergaben vielversprechende 2D-Klassen, in denen die groben Merkmale des Transporters identifiziert werden konnten. Allerdings ist eine verbesserte Präparation erforderlich, um eine hochauflösende Struktur zu erhalten.

Die wichtigsten funktionellen Aspekte eines Transporters sind seine Fähigkeiten, seine Substrate zunächst zu binden und anschließend zu transportieren. In einer Reihe von Experimenten wurden diese Eigenschaften durch einen Radioliganden-Transporttest und durch isothermale Titrationskalorimetrie (ITC) untersucht. Die Transporteigenschaften des Proteins wurden in einem Filter-Test mit radioaktiv markiertem Citrat als Auslesung bestimmt. Das Protein wurde in Proteoliposomen rekonstituiert und der Test bei verschiedensten Substratbedingungen durchgeführt. Verschiedene Ionen wurden auf ihre Fähigkeit hin getestet, den Transport von Citrat anzutreiben oder bei gleichzeitiger Anwesenheit zu hemmen. Die Messungen ergaben, dass nur ein Gradient von Natrium-Ionen in der Lage war, den Transport zu energetisieren und dieser auch nicht durch die Anwesenheit anderer Ionen behindert wurde. Die Ergebnisse eines Kompetitionsexperiments mit verschiedenen Verbindungen, die strukturelle Ähnlichkeit mit Citrat haben, zeigten, dass Isocitrat, und Malat in geringerem Maße, den Transport von Citrat hemmen konnten.

Die Quantifizierung der Bindung von Substraten an das Protein durch thermodynamische Parameter wurde mit der isothermalen Titrationskalorimetrie durchgeführt. Diese Technik erforderte die Herstellung großer Mengen an substratfreiem Protein. Die größte Herausforderung bei den Messungen war die insgesamt niedrige Signalintensität aufgrund der niedrigen Bindungsenthalpien. Da das Protein als Membranprotein nicht beliebig aufkonzentriert werden konnte, konnte die Signalintensität auch nicht durch eine weitere Erhöhung der Proteinkonzentration überwunden werden, was bei niedrigen Bindungsaffinitäten das Mittel der Wahl ist.

Citrat bindet an die Hauptbindungsstelle des Transporters in einer exothermen Reaktion mit einer insgesamt geringen Änderung der Wärme im System. Der Hill-Koeffizient wurde mit 0,228 deutlich kleiner als 1 bestimmt, was auf eine Stöchiometrie von unter einem Citrat pro Dimer hinweist. Die Bindungsaffinität wurde im einstellig mikromolaren Bereich gemessen. Die Bindungsaffinität von Citrat selbst wurde nicht durch den pH-Wert beeinflusst, jedoch

wurde eine starke Abnahme der Enthalpieänderung bei steigenden pH-Werten durch eine geringere Änderung der Entropie kompensiert. Isocitrat als alternatives Substrat führte zu keiner messbaren Bindung.

Bei der Verwendung von ITC zur Untersuchung der Bindung von Natriumionen an den Transporter erwies sich die Vorbereitung der Proben zur Eliminierung von Natrium als aufwendig. Trotz einer insgesamt geringen Signalintensität konnte ein exothermes Bindungsereignis nachgewiesen werden. Die Bindungsaffinität der Natriumionen konnte bis in den einstellig millimolaren Bereich abgeschätzt werden. Eine Titration mit Natrium in Gegenwart von Citrat zeigte eine Bindungskurve, die neben der Natriumbindung auf einen zusätzlichen Beitrag an Bindungsenergie durch das Binden von Citrat an das Protein hinweist.

Um ein besseres Verständnis der Rolle von Aminosäure innerhalb der Bindungsstelle zu erhalten, wurde ein Mutageneseansatz gewählt, bei dem das Wildtyp- und das mutierte SeCitS in ihrer Bindung, ihrem Transport und ihrer Struktur verglichen wurden. Bei den mutierten Seitenketten handelte es sich hauptsächlich um zwei Arginine in der Nähe der Citrat-Bindungsstelle und um Seitenketten innerhalb der Haarnadelkurve der Helix.

Die Transportaktivität aller gemessenen Mutanten lag unter dem Wildtyp-Niveau, wobei die meisten der Arginin-Mutanten einen fast vollständigen Verlust der Transportaktivität aufwiesen.

In ITC-Experimenten wurden die Mutanten auf ihre Fähigkeit Citrat zu binden getestet. Die Ergebnisse zeigen, dass für keine der Varianten eine Bindung von Citrat innerhalb des messbaren höheraffinen Bereichs nachweisbar war.

Das gereinigte Protein der Mutanten wurde auch zur Kristallisation verwendet. Die Varianten von SeCitS kristallisierten zu verschiedenen Kristallformen und zeigten auch Unterschiede in ihrer Kristallpackung, wobei am häufigsten die Raumgruppe analog zu der Packung des Wildtyp-Selenomethionins SeCitS (P2) zu finden war.

Die höchste Auflösung in einem Kristall eines mutierten Proteins war bei $SeCitS_{R428K}$ mit 3,3 Å zu finden. Der Datensatz wurde auf 3,45 Å prozessiert und die Struktur konnte unter Verwendung des Wildtyp-Proteins zum molekularen Ersatz gelöst werden.

$SeCitS_{R428K}$ kristallisierte mit zwei Dimeren pro Einheitszelle, wobei das eine Dimer in einer asymmetrischen Konformation und das zweite Dimer in einer komplett nach innen

gerichteten Konformation vorliegt. Die Citrat-Bindungsstellen waren durch die zusätzliche Elektronendichte in der Struktur gut zu identifizieren. Vergleicht man das mutierte Protein mit dem Wildtyp-Protein, so haben die asymmetrischen Dimere nur einen RMSD von 0,52 Å. Die größte Abweichung zwischen den Strukturen ist auf die alternative Seitenkette zurückzuführen, die sowohl in der nach außen als auch in der nach innen gerichteten Konformation unterschiedlich orientiert ist. Dies führt zu einer weniger strukturierten Komplexierung des gebundenen Citrats in der mutierten Bindungsstelle.

Diese Beobachtungen zusammen mit den funktionellen Daten lassen den Schluss zu, dass die Geometrie durch die Verlängerung der Seitenkette wesentlich verändert wird und somit von großer Bedeutung für die Transportfähigkeiten des Proteins ist.

SUMMARY

Membrane proteins are a diverse group of proteins that serve a multitude of purposes with one of the most important ones being transport. All kinds of substrates are shuffled over biological membranes with the help of dedicated proteins enabling the transport along and against a concentration gradient. Within the group of actively transporting proteins a diverse set of proteins that rely on an electrochemical gradient to facilitate transport of a substrate against its concentration gradient can be found. Those so-called secondary active transporters are a group on integral membrane proteins ubiquitous to all cells. They allow the transport of all kinds of substrates like nutrients, ions, other metabolites and drugs over the hydrophobic barrier created by the cellular and organellar membrane. The gradients that provide the main driving force for most of the transporters are either sodium ions or protons, although transporters utilizing other ions or organic compounds are found as well. In case of exchangers two very similar substrates are transported in opposing direction over the membrane, one against its electrochemical gradient driven by the other.
Along with a structural diversity of the transporters concerning overall shape, oligomerization and number of transmembrane elements comes a mechanistic variety though still following the principle of alternating access. In humans the malfunction of secondary active transporters can lead to a physiological disorders such as epilepsy, depression or obesity.

The focus of this thesis was the structural and functional characterization of the secondary active transporter SeCitS from *Salmonella enterica*, a symporter of the 2-hydroxycarboxylate family. The transport of citrate as a bivalent ion is facilitated by the flux of sodium ions that have an inward-facing gradient over the inner membrane of *Salmonella enterica*. Transport experiments showed that the transport ratio is two sodium ions per citrate molecule, netting in an electroneutral transport. Compared to other members of the family the specificity of the transporter towards its main substrate is very high.

Structural information on the protein was initially obtained through 2D electron crystallography, which allowed the identification of the oval shaped dimer and a first hint towards a significant conformational change that the protein undergoes during its transport cycle. Using 3D crystallography, the X-ray structure of the transporter was solved. The

protein crystalizes as a stable, but conformationally asymmetric dimer. As bound citrate can be readily identified in both protomers they can be assigned into an outward- and an inward-facing conformation, with the main citrate binding site in the outward-facing conformation.

One interesting feature of the crystal structure was the large surface available for multimerization, providing a platform for tight dimerization of the two protomers. On the other hand, SeCitS did not show a true cooperativity of transport. With those two aspects taken into account the question arose if any potential crosstalk between the monomers within the dimer takes place and influences transport (negative cooperativity) or the conformational distribution within the dimer (stabilization of the protein within the membrane).

The functional approach in answering this question was the use of mutated variants of the protein for cross-linking within one monomer. Two residues were chosen respectively to lock one of either conformation to be able to test for transport activity in the remaining protomer. The suitability of the residues was derived from the crystal structure (D112 – R205 to lock the inward-facing conformation and L337 – S412 for the outward-facing conformation). After initial promising results the final variants were not stable enough to be analyzed in transport assays.

To analyze the distribution of relative conformations within the dimer the protein was reconstituted into native-like lipid environment such as nanodiscs or saposin nanoparticles to be analyzed by cryo-electron microscopy. The first images were recorded and did yield promising 2D classes where the general features of the transporter were identified. Yet, an improved preparation is required to obtain a high resolution structure.

The key functional aspects of a transporter are its ability to bind and transport its substrates. In a set of experiments those features were investigated by a radioligand transport assay and by isothermal titration calorimetry (ITC). The transport properties of the protein were assessed in a filter assay using a radioactively labeled citrate as a read-out. The protein was reconstituted into proteoliposomes and subjected to different substrate conditions. Different ions were tested in its ability to drive or inhibit transport, but only sodium ions were able to drive transport and also not hindered by the presence of other ions. Results of a competition experiment showed that isocitrate and malate, to a lesser degree, were able to inhibit transport of citrate.

Quantifying the binding of substrates to the protein trough thermodynamic parameters was done with ITC. This technique required the preparation of high quantities of substrate free protein. The biggest challenge presented was the overall low signal intensity, due to low reaction enthalpy, that could not be overcome by increasing the protein concentration, which is the option of choice for low binding affinities.

Citrate binds to the transporter's main binding site in an exothermic reaction with an overall small change in heat in the system. The Hill coefficient was determined to be significantly lower than 1 at 0.228, indicating a stoichiometry of below one citrate per dimer. The affinity of binding was measured to be within the single digit micromolar range. The binding affinity of citrate was not affected by the pH, but a strong decrease in enthalpy change with rising pH values was compensated by a smaller change in entropy. Isocitrate as an alternative substrate resulted in no measurable binding.

Using ITC to investigate the binding of sodium ions to the transporter proved to require extensive preparation of the samples to achieve a substrate-free state. Albeit an overall low signal intensity, an exothermic binding event was detected. The binding affinity of the sodium ions was estimated to the millimolar range. A sodium titration in the presence of citrate showed a binding curve that indicates a binding of sodium with an additional contribution in binding energy by the additional binding of citrate to the protein.

To get a better understanding of the role of key residues within the binding site, a mutagenesis approach was taken to compare the wild-type and mutant SeCitS in their binding, transport and structure. The mutated residues were mainly two arginines in the vicinity to the citrate binding site and residues within the helix hairpins.

The transport activity of all measured mutants was below wild-type level with most of the arginine mutants showing almost a complete loss in transport activity.

The mutants were tested for their ability to bind citrate in ITC experiments. The results show that for none of the variants a binding of citrate was detectable within the given setup.

The purified mutant protein was also subjected to crystallization setups. The variants of SeCitS grew into differently shaped crystals with some deviations in the crystal packing with the main representative being the space group of the wild-type seleno-methionine SeCitS (P2).

The crystal of mutant protein with the highest resolution was $SeCitS_{R428K}$ at 3.3 Å. The data set was processed to 3.45 Å and the structure could be solved using the wild-type protein for molecular replacement.

$SeCitS_{R428K}$ crystallized with two dimers per unit cell with one dimer in an asymmetric conformation and on in an all inward-facing conformation. The citrate binding sites were visible through additional electron density within the structure. Comparing the mutant protein to the wild-type protein the asymmetric dimers only have an RMSD of 0.52 Å. The biggest deviation between the structures is due to the alternative side chain, which is oriented differently in both outward- and inward-facing conformations. This results in looser complexing of the citrate bound in in the mutated binding site.

Those observations combined with the functional data allowed for the conclusion that the geometry is 1) substantially altered though the extension of the side chain and 2) of great importance for the transport abilities of the protein.

ABBREVIATIONS

2HTC	2-Hydroxycarboxylate Transporter Family
ABC	Adenosintriphosphate-Binding Cassette
AU	Absorption Unit
BCA	Bicinchoninic Acid
BisTris	Methylaminopropane Buffering Agent
BN	Blue Native
BSA	Bovine Serum Albumin
Cryo-EM	Cryogenic Electron Microscopy
DDM	Dodecylmaltoside
DNA	Deoxyribonucleic Acid
EDTA	Ethylenediaminetetraacetic Acid
EM	Electron Microscopy
GABA	γ-Amino Butyric Acid
GGXG	Sequence: Glycine-Glycine-Variable Amino Acid-Glycine
HEPES	Sulfonic Acid Buffering Agent
HIS-tag	Polyhistidine Sequence
IF	Inward-Facing
IMAC	Immobilized Metal Affinity Chomatography
INDY	Citrate Transporter I'm not dead yet
ITC	Isothermal Titration Calorimetry
K_A	Association Constant
K_D	Dissociation Constant
K_M	Michaelis-Menten Constant
LCP	Lipid Cubic Phase
MalP	maltose binding protein
MES	Sulfonic Acid Buffering Agent
MSP	Membrane Scaffold Protein
MW	Molecular Weight
ND	Nanodisc

NMDA	N-Methyl-D-aspartate
OD	Optical Density
OF	Outward-Facing
OG	Octylglycoside
PAGE	Polyacrylamide Gelelectrophoresis
PCR	Polymerase Chain Reaction
PDB	Protein Databank
RMSD	Root Mean Square Deviation
SAD	Single-Wavelength Anomalous Dispersion
SEC	Size Exclusion Chromatography
SeCitS	Citrate Transporter S from *Salmonella enterica*
ST[3]	Class 3 in MemGen Classification System by Hydropathy Profile Alignment
TC system	Transporter Classification System
TMH	Transmembrane Helix
TMS	Transmembrane Segment
WT	Wild-Type

1. INTRODUCTION

1.1 BIOLOGICAL MEMBRANES AND MEMBRANE PROTEINS

Biological membranes are an essential requirement for all living organisms as they confer structure and define the borders of single-cell organisms, cells and cellular organelles. Membranes are implicated in numerous biological processes by allowing compartmentalization, establishment of electrochemical gradients, uptake and secretion of nutrients and metabolites, signal transduction, control of enzymatic activity and regulation of adhesion and mobility (Cho *et al.*, 2016). Biological membranes consist of a lipid bilayer of 3-6 nm thickness. The composition of lipids in membranes differs not only between prokaryotes and eukaryotes but also between species, cells and organelles. Even within a continuous membrane, different lipid compositions can be found between the two leaflets of the membrane and in defined regions as membrane patches (Stillwell, 2013). Membranes provide an environment for proteins and carbohydrates, which can be bound directly to the lipids or mediated by proteins (Smith, 2012).

Genomic analysis shows that membrane proteins account for 30% of eukaryotic genes (Engel & Gaub, 2008). Lipid membranes contain up to 80% (w/w) membrane-associated proteins (Luckey, 2008). Two types of membrane-associated proteins can be distinguished, peripheral and integral proteins. Peripheral proteins are reversibly attached to the membrane via electrostatic interactions. This kind of transient binding allows specific enzymatic activity, but may also include structural aspects (Hedin *et al.*, 2011). Soluble proteins may be tethered to the membrane via lipid anchors and thus act in a similar manner (Martens & Fracchiolla, 2020). Integral membrane proteins are partially or fully inserted into the membrane. The two common structural domains of integral membrane proteins are α-helix bundles and β-barrels. Those proteins are particularly important for transport and signal transduction (Hedin *et al.*, 2011). Membrane proteins represent more than 50% of drug targets (Bakheet & Doig, 2009). Therefore, these proteins have a high medical importance and detailed information on structure and biochemical properties are required to understand their mode of action. However, the fraction of transmembrane protein entries in the Protein Data Bank (PDB) remains to be low, with a mere 4.2 % of all

entries. This underscores the need for further structure-function studies in order to deepen the unterstanding of membrane proteins in general, to identify new possible drug targets and to guide the development of pharmaceuticals.

1.2 Membrane Transport Proteins

Due to the hydrophobicity of the inner part of the lipid bilayer, membranes are nearly impermeable for hydrophilic as well as charged compounds. As flux of water, ions and nutrients is essential for physiological homoeostasis, a vast variety of transport proteins exist, which enable and regulate transport across membranes with different degrees of specificity (Engel & Gaub, 2008). These proteins can be classified by their functionality (Figure 1.1). Porins, aquaporins and channels enable passive transport along a concentration gradient over their respective membrane. Porins are water-filled β-barrel pores in the outer membranes of mitochondria, chloroplasts and gram negative bacteria. They enable passive diffusion of a large variety of solutes, either with a higher specificity or in an unspecific manner. To allow for a regulation of flow, porins restrict transport activity via their oligomeric state, switchable loops and also depending on their substrate gradient (Fairman *et al.*, 2011). Aquaporins, also known as water channels, have six membrane-spanning α-helices, with both termini on the cytoplasmic side. They occur in bacteria, fungi, plants and animals and facilitate water flow between cells (Li & Wang, 2017). Channels enable diffusion of water and small ions. They are typically highly specific for one species (Gouaux & MacKinnon, 2005). A number of channels are ligand-gated and thus only allow passage for their substrates in the presence or absence of their ligand. Such ligand-gated ion channels are found e.g. as γ-aminobutyrate (GABA), *N*-methyl-D-aspartate (NMDA) or serotonin receptors in the postsynaptic neural membrane. They allow a flow of ions such as Na^+, K^+ and Ca^{2+} across the cell membrane after binding of presynaptically released neurotransmitter molecules (Hucho & Weise, 2001).

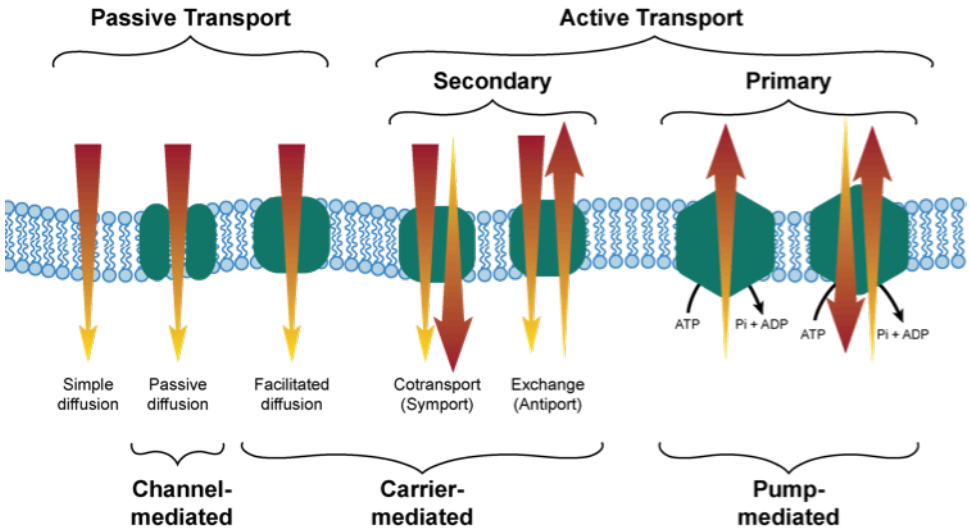

Figure 1.1: Overview of membrane transport processes. Transport across membranes can be divided into active and passive transport. Active transport occurs against the concentration gradient and can be energized by ATP (primary active transporter) or by an electrochemical gradient of a co-substrate (secondary active transporter). Passive transport processes follow the concentration gradient of the substrate and rely on simple diffusion, channel-mediated passive diffusion or carrier-mediated diffusion.

Active transporters translocate their main substrates against their chemical gradient under energy consumption (Luckey, 2008). Depending on the source of energy two groups are distinguished: primary and secondary active transporters. Primary transporters are often also described as molecular ion pumps, which energize the membrane by building up a electrochemical potential across the membrane. This process can be energized by redox processes (e.g. complexes I-III of the respiratory chain), light (e.g. photosynthetic reaction centers), or by hydrolysis of adenosine-triphosphate (ATP) in either P-/V-/F-type ATPases (Morth *et al.*, 2011) or ATP-binding cassette (ABC) transporters (Hinz & Tampé, 2012). The resulting electrochemical potential can be used for an an excitatory postsynaptic potential in case of neuronal cells or for the transport of nutrients and metabolites by secondary active transporters (Saier, 2000).

1.3 Secondary Active Transporters

Secondary active transporters are found in every cell. They allow the uptake of nutrients, the efflux of metabolites and toxic substances and the removal of neurotransmitters from the synaptic cleft. In humans, malfunction of secondary transporters may lead to severe disorders like epilepsy, depression and obesity. This makes them interesting drug targets

(Krishnamurthy *et al.*, 2009). The main substrate is translocated across the membrane against its concentration gradient. The source of energy for this unfavorable transport is derived from the coupling to a co-substrate passage along its concentration gradient, which in turn is typically created by a primary active transporter. The two groups of secondary active transporters are symporters with a unidirectional transport and antiporters, where substrates translocate in a bidirectional fashion, i. e. in opposite directions (Forrest *et al.*, 2011). Secondary transporters are generally classified by two different classification systems. The transporter classification system (TC system) is based on function, mode of transport and phylogeny (Saier, 2000). In this classification, more than 250 families were identified, of which 40 families were assigned to human proteins (Busch & Saier, 2004). Another classification (MemGen) describes classes of proteins based on their hydropathy profile, representing a specific fold (Lolkema & Slotboom, 1998). This approach leads to a high phylogenetic and functional diversity within the classes. One example is the ST[3] class with thousands of different secondary transporters from 32 families (Ter Horst & Lolkema, 2012).

Between the classes and families of secondary transporters, there is a large diversity in amino acid sequences, 3D structure of the proteins and chemical nature of their substrates (Sobczak & Lolkema, 2005*a*). The substrates transported against their concentration gradient range from ions, amino acids, sugars and intermediary metabolites to peptides, sterols, nucleosides/nucleotides and drugs (Forrest *et al.*, 2011). The co-substrates are far less diverse as most secondary transporters rely on gradients of protons or sodium ions. Yet, there are a few special cases: potassium ions and chloride ions can also be coupled to the transport (Krishnamurthy *et al.*, 2009). For the last 15 years the number of 3D structures of secondary transporters and other membrane proteins has been increasing drastically to more than 1100 unique structures. Along a steady amount of new structures solved by X-ray christallography, more and more structures are solved using cryo-EM, allowing identification of unique and common structural features (White, 2020).

The solved structures of secondary active transporters commonly show a general α-helical arrangement with 4-14 transmembrane segments (TMS), 11-13 being the most common. Of those three-dimensional protein structures, common global structural motifs are partially shared by transporters of low primary structure similarity (Tsai & Ziegler, 2010). These proteins are regularly found to be functional dimers or trimers. Within the monomers, an internal structural symmetry of repeats can be identified. As those folds appear in symporters and antiporters alike, the global protein structure cannot be used to indicate,

nor does it dictate the mode of transport (Forrest *et al.*, 2011). Substrate-bound protein structures reveal binding of the main substrate within the center of a monomer, even if the functional transporter has a higher oligomerization state. This shows that the monomer may function as an independent unit but the oligomerization is important for its structural stability and regulatory aspects (Perez *et al.*, 2011). The known exception where the multimerization interface is essential for transport is the H^+/drug antiporter EmrE, which essentially needs the antiparallel dimerization to form a pore for the substrate (Chen *et al.*, 2007).

The common feature of secondary transporters is the internal structural symmetry. Two defined domains which are structurally related appear within one monomer (Forrest *et al.*, 2011). The internal symmetry can be categorized in two forms with different origins. Ancient gene duplication events may have led to the monomeric transporters with defined structural repeats. In sets of two or more those can be helical domains with significant sequence similarity. A symmetry axis then appears along the center of the monomeric protein (Pao *et al.*, 1998). However, even in proteins with low sequence similarity between the domains a pseudo two-fold symmetry appears. An uneven number of helices build up helical repeats which arrange in an inverted orientation. The apparent axis symmetry of the 'inverted topology' runs parallel to the membrane (Abramson & Wright, 2009). These findings strongly suggest a functional role of the structural symmetry for substrate translocation.

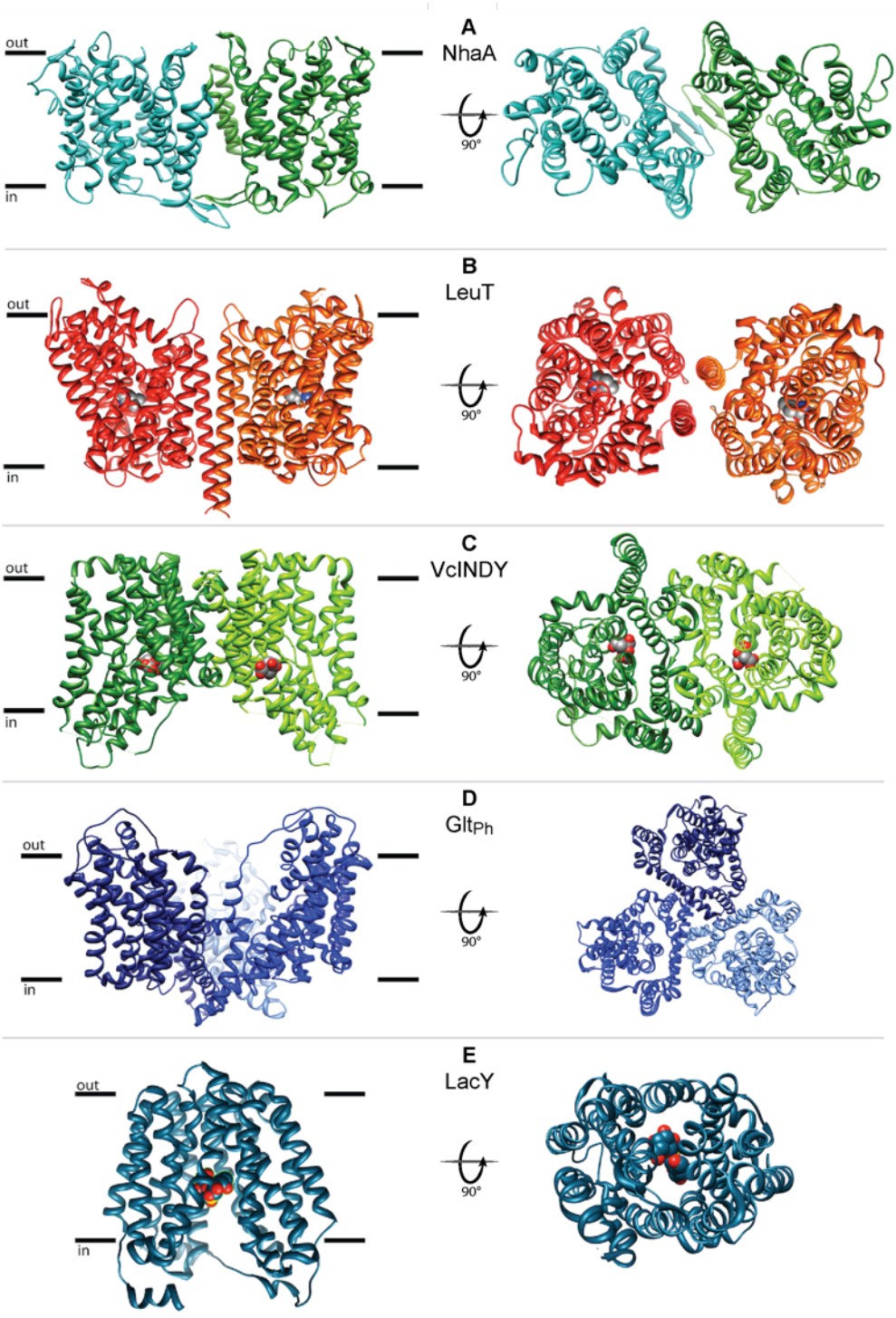

Figure 1.2: Secondary transporters exhibit a large structural diversity. 3D structures of five transporters with different oligomerization states are shown in sideview (left) and extracellular view (right) of (A) sodium proton antiporter NhaA (pdb 3FI1), (B) the bacterial leucine transporter LeuT (pdb 2AG5), (C) the bacterial dicarboxylate transporter VcINDY (pdb 4F35), (D) the glutamate transporter GltPh (pdb 1XFH) and (E) the lactose permease LacY (pdb 1PV7). Differentiation of monomers is achieved with different hues. Black lines indicate membrane boundaries. If available, bound substrates are displayed as spherical molecules. Adopted from (Kebbel, 2013).

1.4 Transport Model of 'Alternating Access'

The first model of transport across membranes by secondary active transporters was proposed in 1966 (Jardetzky, 1966). It suggested an alternating access towards both sides of the membrane. A cycle of defined structural states within the protein allows the translocation. Lately, rising numbers of structures with similar folds or especially in different conformations give insight into the modes and conformational dynamics of transport (Forrest *et al.*, 2011). The current model of a general secondary symport is depicted in Figure 1.3. The initial substrate binding of main substrate and co-substrate occur to the empty outward-facing (OF) protein. The binding triggers a closure of the protein. The occluded substrate-bound state marks the transition towards the inward-facing (IF) closed conformation. The substrates are subsequently released from the protein upon opening. Lastly the protein cycles through an occluded empty state towards the external open empty state for the next transport cycle (Forrest *et al.*, 2011).

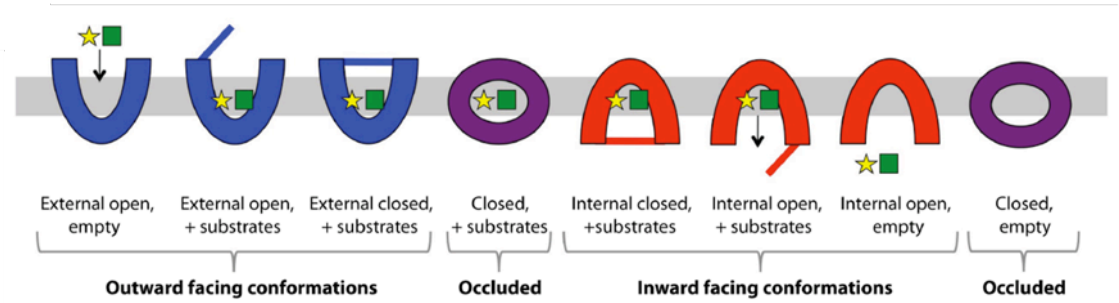

Figure 1.3 Alternating access mechanism of secondary symport. Secondary transporters exist in three main conformations: outward-facing (blue), inward-facing (red) and occluded (purple). For the depicted secondary symport the different states of the outward-facing conformation are the empty state, open + substrate-bound and closed + substrate-bound state. The same states exist for the inward-facing confirmation in inverted order. The occluded states are the transition states, substrate-bound towards inward-facing confirmations and empty towards outward-facing confirmation. The main- and co-substrate are shown as yellow stars and green squares. Adopted from (Kebbel *et al.*, 2013).

There are three main modes of movement of the protein to enable the alternating access cycle. The 'gating' mechanism shows a movement of the substrate within the transport process and is only described for the bacterial homologues of the glutamate transporter GltPh (Reyes *et al.*, 2009). The 'rocker-switch' shows a rocking movement of the two symmetry-related domains. The domains alternately allow access to a central binding side

for the main-substrate in an axis symmetric manner. The 'rocking bundle' also involves the movement of the domains against each other. The domains are not symmetry related, therefore the helical bundle rocks against the other domain but in an asymmetric manner. Another variant of the 'rocking bundle' is the 'elevator' machanism, where one domain remains near static while the other performs a much bigger movement. The latter two mechanisms have in common that the substrate remains at its binding site during the occluded state and leaves the transporter at the other side only after the transition (Garaeva & Slotboom, 2020).

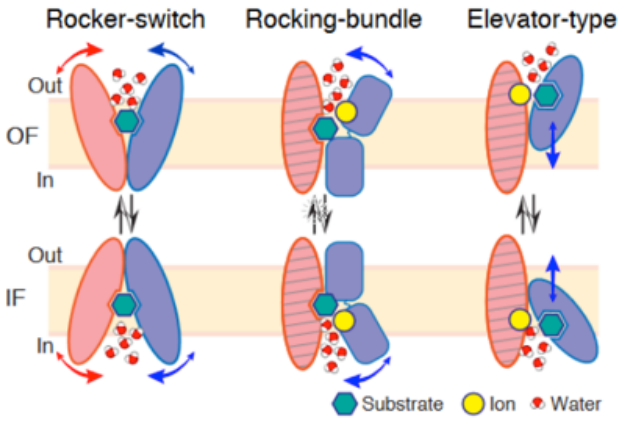

Figure 1.4: Conformational Changes in alternating access models (schematic representation). Transport can occur through rocker-switch (left), rocking-bundle (middle), or elevator-type (right) mechanisms, during which the transporter alternates between the OF (top) and IF (bottom) states. Each transporter is schematically represented as two domains (pink and blue) with stationary domains in shaded colors. Conformational transitions are shown as the changes in the relative angles between the domains and the water accessibility of the transporters. (Jiang *et al.*, 2020)

Movement of the protein during translocation of a substrate is energetically unfavorable, but the free energy barriers are overcome by two main means. Within the cycle of different conformations, the states do not share the same relative energy. The occluded states and the inward-open substrate-bound states are local energy maxima. The protein is at local energetic minima in the inward-open substrate free conformation and in the outward-closed substrate-bound state. For an easy transition through the cycle, the energy curve is smoothened by 'induced transition fit'. The substrate binding site of the empty protein is not a perfect match to the substrate, while a good fit occurs during the substrate-bound occluded state. By that, the transition of the substrate-bound outward state to the occluded state is eased. Secondly the main driving force is the coupling of the transport of the main substrate to a co-substrate, which is transported along its chemical gradient. This allows an exploitation of the electrochemical gradient to trigger the reaction (Jencks, 1989). The rate-

limiting steps during the secondary transport are mainly the independent binding of the substrates to the outward-open state and the conformational change from the inward-facing empty state to the outward-facing empty state (Wright, 1993). On the other hand, higher transport rates can be achieved by low substrate affinities with a K_D in the micromolar range as well as fast diffusion of the substrate away from the transporter in the inward-facing state (Forrest *et al.*, 2011).

1.5 HYDROXYCARBOXYLATE TRANSPORTERS

Hydroxycarboxylate transporters (2HCT) form their own family of secondary active transporters. This exclusively bacterial family represents the best-studied family in the ST[3] class within the MemGen system. It thereby serves as a model family, although structural insights are rare (Ter Horst & Lolkema, 2012). The common feature of the family is the 2-hydroxycarboxylate motif in the substrates of the proteins (Bandell *et al.*, 1997). 2HCT proteins support bacterial nutrient utilization, primarily the fermatation of malate, lactate and citrate. The symporters in the 2HCT family typically transport only one or two 2-hydroxycarboxylates, while the exchangers carry a variety of 2-hydroxycarboxylate substrates (Ishiguro *et al.*, 1992; Bandell *et al.*, 1997; Wei *et al.*, 2000). Among the best-studied members of the 2HCT family are the *Klebsiella pneumoniae* Na^+-citrate symporter CitS, the *Bacillus subtilis* citrate/malate H^+-symporter CimH, as well as the malate/lactate exchanger MleP and the citrate/lactate exchanger CitP found in lactic acid bacteria (Sobczak & Lolkema, 2005*a*).

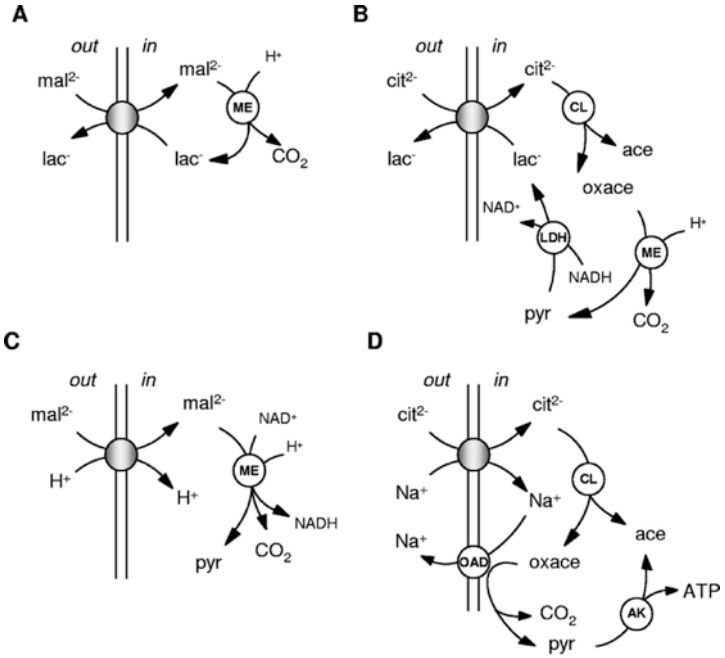

Figure 1.5: Physiological pathways of substrate metabolism for 2HCT family members. 2HCT transporters play a role in (A) Malolactic fermentation; (B) citrolactic fermentation; (C) oxidative malate decarboxylation pathway; (D) citrate fermentation in gram-negative bacteria. Shaded circles represent the 2HCT transporter proteins. Abbreviations: cit, citrate; mal, malate; lac, lactate; oxace, oxaloacetate; ace, acetate; pyr, pyruvate; ME, malic enzyme; CL, citrate lyase; OAD, oxaloacetate decarboxylase; LDH, lactate dehydrogenase; AK, acetate kinase. (Sobczak & Lolkema, 2005)

Secondary active transporters for citrate or other 2HC substrates are also found outside the bacterial domain and are required for a variety of functions in hydrocarboxylate metabolism. A prominent example is the *Drosophila melanogaster* gene that encodes for the citrate transporter INDY (I'm not dead yet) which was also studied in *Caenorhabditis elegans*. Downregulation of *indy* expression in these species extended their life span by a mechanism resembling caloric restriction, yet witout reducing food intake. In *Drosophila melanogaster*, deletion of the *indy* gene reduced body fat content, insulin-like protein concentration and reactive oxygen species production (Willmes & Birkenfeld, 2013).

The human INDY homolog, the citrate transporter NaCT, is involved in fatty acid synthesis, glycolysis via the uptake of citrate into the cytosol of liver cells (Inoue *et al.*, 2002; Gopal *et al.*, 2007). This transporter is therefore considered to be a drug target in fatty liver disease, a frequent co-morbidity of type 2 diabetes and obesity (Willmes & Birkenfeld, 2013; Huard *et al.*, 2015).

A number of structures of a variety of transporters were obtained, presenting either an inward (VcINDY) or an outward conformation (Glt_{Ph}). Due to the lack of crystal structures of the same protein in different conformations, the transport mechanism of ST3 class members is still not fully understood and leaves room for further investigation.

1.6 SODIUM-DEPENDENT CITRATE TRANSPORTER FROM *SALMONELLA ENTERICA*

The functionally and structurally best-characterized member of the 2-hydroxycarboxylate transporter family is a citrate symporter from *Klebsiella pneumonia* (KpCitS), which is induced during and facilitates anaerobic metabolism (Bott *et al.*, 1995). It was identified as a citrate transporter with one putative citrate binding site. The co-substrate was identified to be sodium, and two putative sodium ion binding sites were proposed based on functional analysis ((Lolkema *et al.*, 1994). KpCitS was purified to homogeneity, allowing a more precise determination of its biochemical properties (Pos *et al.*, 1994). After reconstitution of the transporter, uptake measurements revealed that both sodium ion and pH gradients influenced its activity. In addition, counterflow experiments demonstrated that KpCitS acts via a simultaneous type of mechanism, exposing its binding sites to the two sides of the membrane at the same time, most likely in the form of a homodimer.
The questions whether protons play a role in the transport is still unresolved, but the transported citrate was identified as the monohydro-dianionic species ($HCit^{2-}$). Transport is electroneutral as two sodium ions are carried across the membrane together with monohydrocitrate (Pos & Dimroth, 1996).

The 446 amino acids of KpCitS form eleven transmembrane segments (TMS), which are organized in two repeats and share a similar fold. The odd number of TMS allows the typical inverted topology (Lolkema, 2006). The N-terminus forms another helix and is on the cytoplasmic side, whereas the C-terminus is on the periplasmic side of the membrane (van Geest & Lolkema, 2000). The longer loop between helix VIII and IX folds into an amphipathic surface helix (Figure 1.6) (Sobczak & Lolkema, 2005*b*). The amino acids between the helices V and VI, and X and XI form membrane-embedded loops with a conserved GGxG motif, a defining characteristic in the 2HTC family (Dobrowolski & Lolkema, 2009). The detailed topology model based on the hydrophobicity and sequence serves as representative for all 2HTC members (Figure 1.6).

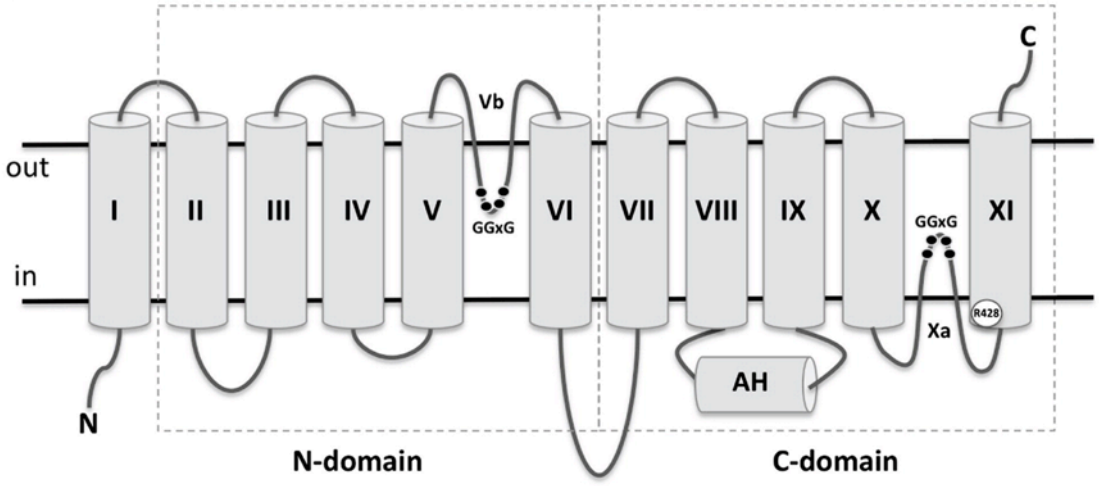

Figure 1.6: Schematic topology of KpCitS. The protein consists of 1+5+5 membrane segments. The N- and C-terminal domains are organized in inversed topology and connected by a cytosolic loop. The loop between helix VIII and IX builds an amphipathic surface helix. The loops between helix IV and V of each domain show a conserved GGxG motif. Adopted from (Kebbel *et al.*, 2013).

The 6 Å 2D projection structure (Figure 1.7a) of KpCitS, obtainied by diffraction analysis of 2D crystals by electron microscopy (Kebbel *et al.*, 2012), showed a homodimer with a high similarity to the sequentially unrelated NhaP1 (Figure 1.7b) (Goswami *et al.*, 2011). The domains of both monomers result in an overall shape of an ellipsoid with two distal helical clusters and a central dimerization interface. The overall architecture also shows a resemblance to VcINDY also (Mancusso *et al.*, 2012).

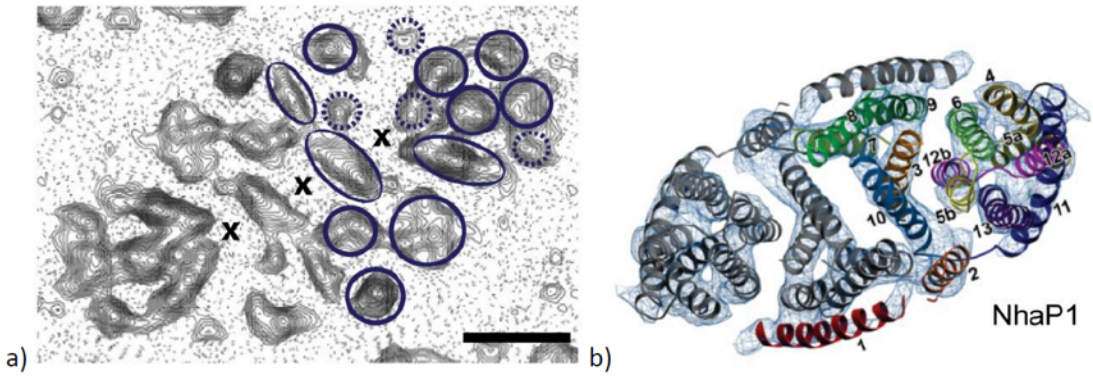

Figure 1.7: Contour plot of KpCitS (a) and model of NhaP1 (b). a) Contour map of a single KpCitS dimer from a merged projection map at 6 Å resolution obtained by electron crystallography. Blue circles mark the prominent electron densities within one dimer; low densities are marked with black crosses. The scale bar is 2 nm. Adopted from (Kebbel *et al.*, 2012). b) Model of NhaP1 in topview. The 13 helices of one monomer are numbered. (Goswami *et al.*, 2011)

A 3D model based on an electron crystallography map shows 13 rod-shaped densities (Figure 1.7a). After assigning the 11 helices per monomer, the two additional densities were proposed to derive from the membrane embedded loops. Difference projection maps obtained from substrate-free and citrate-bound states show a change in the distal helical cluster upon substrate binding (Figure 1.8b) (Kebbel *et al.*, 2013).

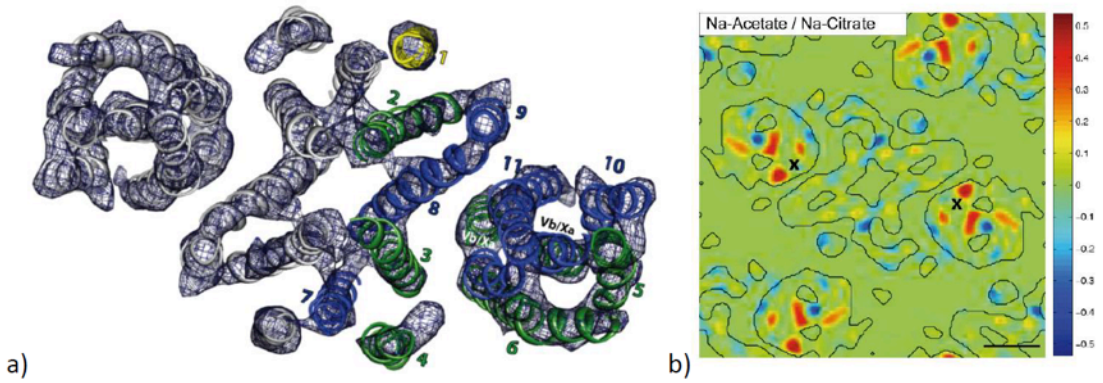

Figure 1.8: Model of KpCitS (a) and difference map in substrate-induced conformational change (b). a) Molecular model of KpCitS. The TMS are depicted in yellow (TMS 1), green (TMS 2-6) and blue (TMS 7-11). b) Difference map with contour of KpCitS in the presence of Na-Acetate/Na-Citrate. Citrate binding causes a density shift within the distal helix cluster. Proposed substrate translocation sites are indicated with crosses. (Kebbel *et al.*, 2013)

1.6.1 Functional Information of SeCitS

The protein of interest in this thesis is the secondary active sodium-dependent citrate transporter *Salmonella enterica* (SeCitS), a member of the 2-hydroxycarboxylate transporter family. As the preparation of KpCitS was insufficient in first experiments, a number of homologues and functionally similar proteins were chosen and SeCitS proved to be most suitable in terms of preparation and stability. Due to the high sequence identity, functional characteristics of SeCitS from *Salmonella* and *Klebsiella* are congruent in a lot of areas.

The transport of citrate and sodium of SeCitS has been analyzed previously (Grötzinger, 2014). It was shown that citrate transport follows Michaelis-Menten kinetics (Figure 1.9). SeCitS has a high affinity for citrate with a K_M of 4.1 µM. Sodium ions are required to drive the transport. They act in a cooperative manner with a Hill coefficient of 1.89 with a half-saturation concentration of 3.3 mM. In combination with these findings, it can be concluded

that the homotropic effect of sodium derives from within the protomer rather than the dimer.

The maximal velocity v_{max} of the transporter is at around 24 nmol/(min mg). This leads to a turnover of 1.2 citrate molecules per minute per protomer. In comparison with KpCitS, the turnover rate is lower (Wöhlert *et al.*, 2015).

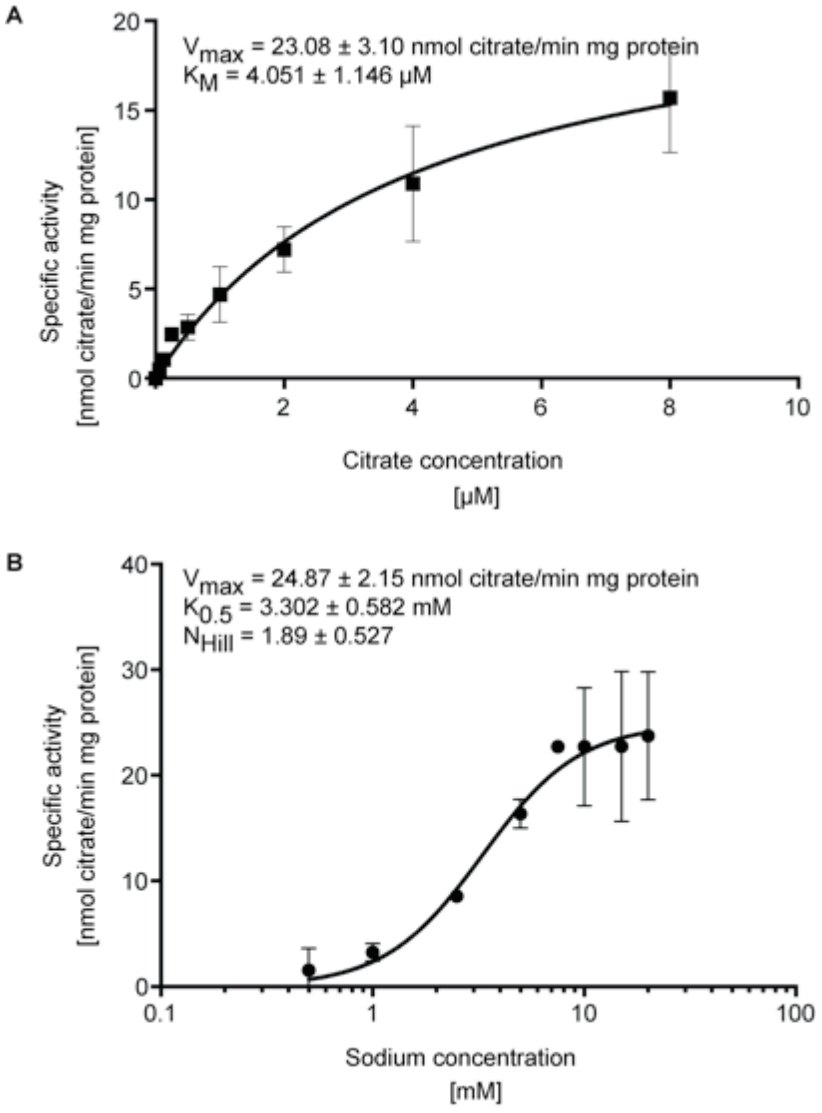

Figure 1.9: Citrate transport kinetics of SeCitS. Transport activity measured by uptake into proteoliposomes A) Citrate transport follows the Michaelis-Menten kinetics with a high affinity for citrate at a K_M of 4.1 µM. B) Sodium is transported in a cooperative manner with a Hill coefficient of 1.89. The half-saturation concentration is 3.3 mM with a v_{max} of 24 nmol/min mg (Grötzinger, 2014).

1.6.2 CRYSTAL STRUCTURE OF SECITS

For a better understanding of the transport mechanisms, the high-resolution crystal structure of SeCitS has been solved by single-wavelength anomalous dispersion (SAD) with seleno-methionine (SeMet) derivatized crystals (Wöhlert *et al.*, 2015). The initial phases obtained by SeMet-SAD were extended to a data set collected from native crystals and the final native structure was refined to 2.5 Å. The structure reveals two homodimers in a unit cell with two asymmetrically oriented protomers per dimer. The two outward-facing conformations were identical, but the inward-facing conformations deviated by small but significant differences. So in total, three different conformations were identified within those two dimers. The overall oval shape of the dimer has a long axis of 96 Å and a short axis of 60 Å (Figure 1.10). Each protomer consists of 13 helical elements with two helix hairpins and 11 transmembrane helices (TMH H1-H5, H7-H11, H13). The hairpins are located between helices H5 and H7 (H6a/b) and helices H11 and H13 (H12a/b). The hairpins and adjacent helices form a bundle on the far sides of the dimer. Helices H1-H4 and H7-H9 form the central contact domain for the dimer interface. The dimer is stabilized through extensive hydrophobic interactions of helices H2, H4, H8 and H10. The loops between the helices are mainly short or form amphipathic α-helices. A longer stretch of the protein, a loop between the helix bundle H7 and the interaction interface domain, is not well resolved mainly due to flexibility of that region.

The general architecture follows the inverted repeats system with helices H2-H7 and H8-H13 forming the repeats. Helix H1 is an additional transmembrane helix at the N-terminus of the protein. The N-terminus is located on the cytoplasmic side and the C-terminus on the outside.

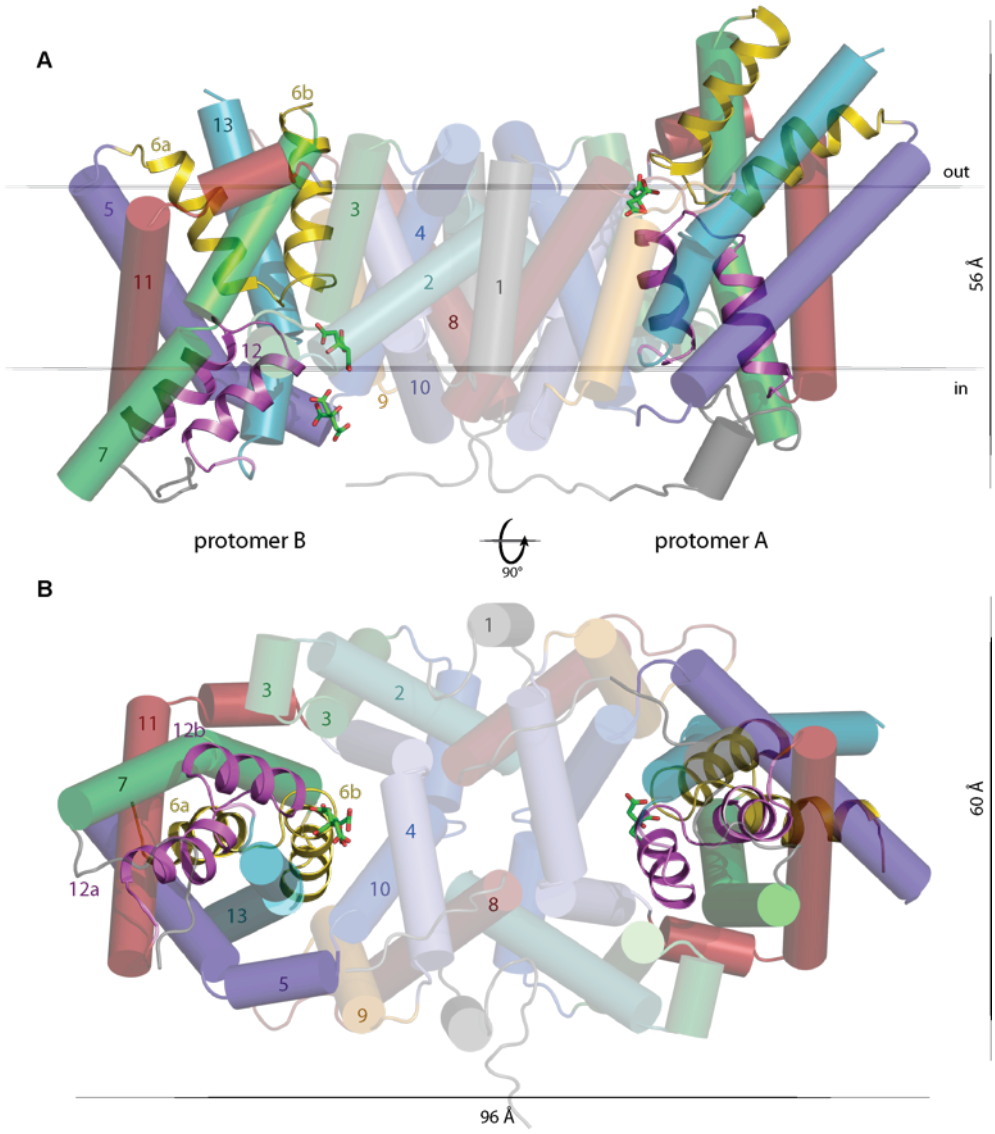

Figure 1.10: Overall structure of SeCitS of *Salmonella enterica*. Side view (A) and cytoplasmic view (B) of the SeCitS dimer that contains 13 TMHs per protomer. Each protomer can be divided in a helix bundle (high opacity) and an interface domain (low opacity). The main substrate binding site is made of two hairpin helices depicted in pink and yellow with the bound citrate shown in green.

An interesting aspect of the crystal structure is the conformations found within the dimer. The two dimers in the asymmetric unit are similar. The RMSD (root mean square deviation) is only 0.5 Å between the two dimers, but the protomers within a single dimer show vastly different conformations with an RMSD of 8.4 Å. Comparing only the interface domains, an RMSD of 0.5 Å shows very little variability. Interestingly, the helix bundles in the different conformations also only have an RMSD of 0.8 Å, but their relative position to the interface domain gives rise to the overall big RMSD between the protomers. In one protomer, the

loops of both hairpins are exposed to the periplasmic side while they are accessible to the cytoplasmic side in the other one. The implications of such a substantial conformational difference are that the states can be assigned as outward- and inward-facing (Figure 1.11 a and b).

The outward-facing state, with the loops of the hairpins opening up to the periplasmic side, has the helix bundle protrude 16 Å above the outer membrane surface. In the inward-facing conformation, the cytoplasmic protrusion is at 13 Å, while the helix bundle is nearly completely submerged in the membrane on the periplasmic side. The relative orientation of the helices within the helix bundle does not change between the two conformations and implies a rigid body movement of the helix bundle during the transition from one conformation to the other. The interface shows no difference thus seems to remain static. Differences between the inward- and outward-facing conformations lead to some structural accommodations made mainly by the loops connecting the domains. The amphipathic helix connecting H2 and H3 moves by 2 Å towards the helix bundle in the inward-facing conformation and so does the loop between H7 and H8. Another accommodation of the movement is seen. Helix H5, which is straight in the outward-facing conformation, features a kink close to the end of the helix preventing its exposure to the cytoplasm.

In between the two protomers a hydrophobic cavity can be found, which also features an electron density that can be assigned to a hydrophobic tail of a detergent or lipid molecule.

Another prominent feature of the protein is a deeper positively charged cavity on the inward-facing conformation. This cavity is completely closed in the outward conformation, but congruently features a small positively charged area on the extracellular side.

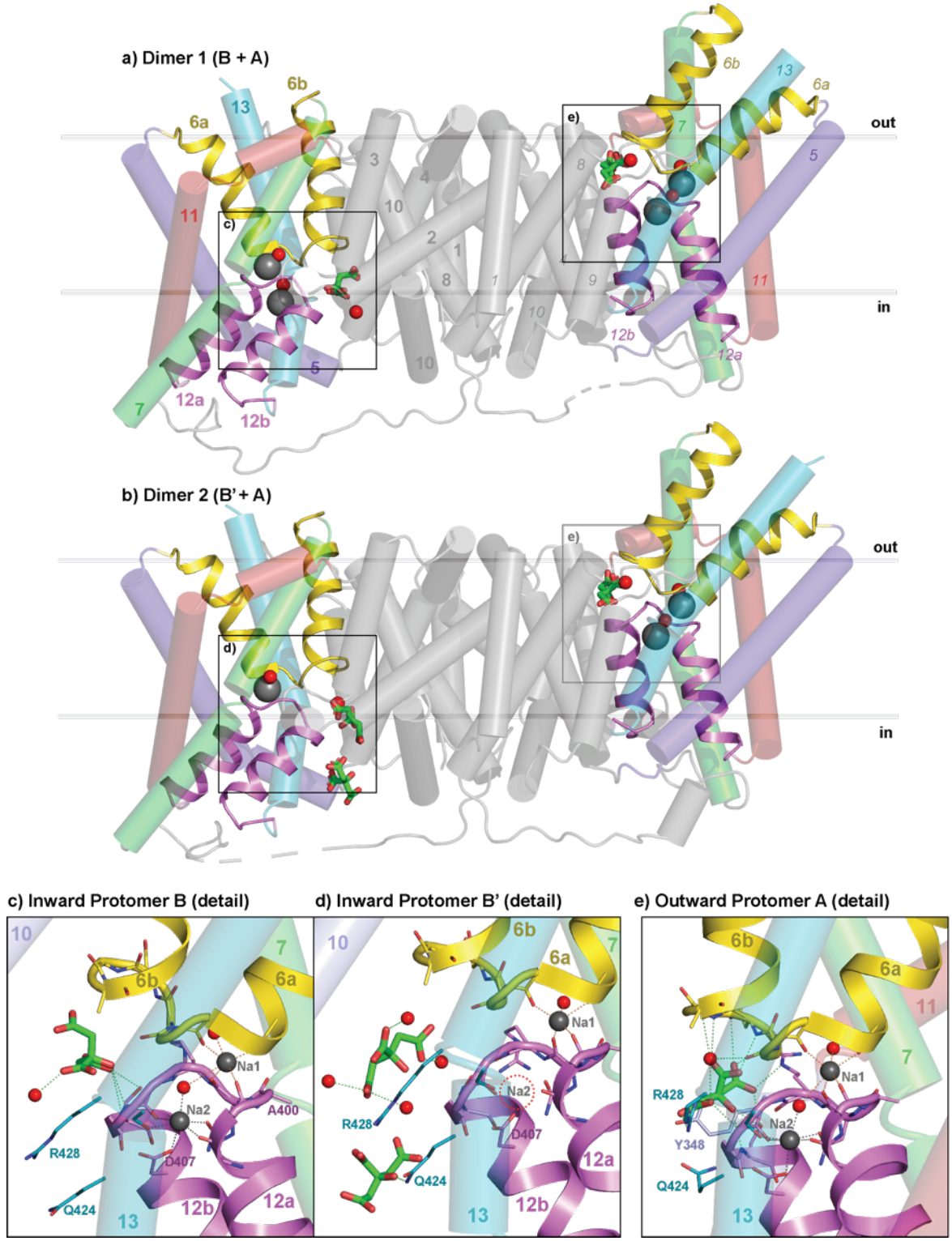

Figure 1.11: Conformational differences and substrate binding sites in the protomers. A) Overview of the substrate binding sites of dimer 1 in the unit cell composed of protomer A and B in outward- and inward-facing conformations. B) Comparison of the binding sites in the second dimer of the unit cell with featuring a structural variation in the inward-facing protomer (B'). The detailed binding of the main substrate citrate with the co-substrates sodium and involved residues are shown for all distinct sites in C), D) and E). The inward-facing protomers can be interpreted as sequential snapshots from protomer B (C) to B' (E), as the second sodium ion is not present anymore and a secondary site for citrate was identified. The sodium ions in the outward-facing protomer are well coordinated by the hairpin loops H6 and H12. (pdb:5A1S)

The two helix hairpins are a particular feature of the transporter. The tips of the hairpins are rich in glycines to allow a tight curvature of the amino acid chain connecting the two halves of the hairpins. A special sequence that can be also found in other members of the 2HCT family is the GGXG motive in the unwound part of the loop. A mutation within this sequence was previously shown to hinder transport (Dobrowolski & Lolkema, 2009). The region of interaction of both hairpins reaching into the protein from either side defines the substrate binding site at the interface of helix bundle and contact domain.

In both conformations, clear electron density for substrates was found between the tips of the helix hairpin H6 and H12. In addition to both hairpins also helix H1 and H13 are involved in substrate coordination (Figure 1.11). In the outward-facing conformation, the electron density located at the tips of the hairpin loops in a 6 Å deep extracellular cavity could be interpreted as a citrate molecule. It is mainly coordinated by the two positively charged arginine side chains R402 and R428 and the polar side chains of S405 and N186. Additionally, the backbone of both hairpins, especially the amide-nitrogen atoms of amino acids N186, G187, G404 and S405, facilitate binding. The benzyl side chain of Y348 is in close proximity to one of the citrate carboxylates at 3.3 Å, enabling a π-π-interaction (Figure 1.11 e). The outward conformation allows the clear identification of two sodium binding sites. The first sodium ion is coordinated by backbone carbonyls in the unwound parts of the helix hairpins, namely I181, G183, M399 and N401. The second sodium ion is bound by the side chains of N401 and S427, the carboxyl group of D407 and the backbone carbonyls of C398 and G403. An additional density suggests a structural water between both sodium ions. The cooperativity of transport in respect to sodium can be assigned to this structural water and the involvement of N401 in coordinating both sodium ions, thus linking binding events of both sodium ions. The sodium ions are occluded, while the citrate is still solvent-accessible. From their respective positioning it appears that the sodium ions need to bind before the citrate to facilitate transport.

The inward-facing binding site of citrate is located in the large cytoplasmic cavity between the helix bundle and the contact domain with a depth of about 13 Å. The location of citrate and sodium differ slightly in the two inward-facing conformations and thus are able to shed more light on the release of the substrates (Figure 1.11 c and d). In one of the two inward-facing protomers the citrate is partially hydrated and loosely coordinated by the hydroxyl of S405 and the backbone carbonyl of G404 at the tip of helix hairpin H12. The two sodium sites are in the same relative position to the citrate as in the outward-facing conformation. In the second inward-facing structure the sodium sites have the same structural makeup but

are only partially populated as no density for the second sodium can be detected. Despite relative proximity of the citrate to the amino acids involved in the coordination in the outward-facing conformation there is no direct coordination. The citrate is hydrated and only indirectly coordinated by R428 via a bridging water molecule. Those results are in line with experiments showing a reduced binding affinity on the inside so the citrate can detach from the transporter. The partial release of citrate could subsequently weaken sodium binding.

A comparison of the binding sites of citrate in the two conformations indicates a near vertical translocation by 16 Å. Similarly, the sodium binding sites are shifted by 11 Å. This transition between the two states is facilitated by an arc-like rotation of the helix bundle by 31° with the center of rotation outside the far ends of the protein in the membrane.

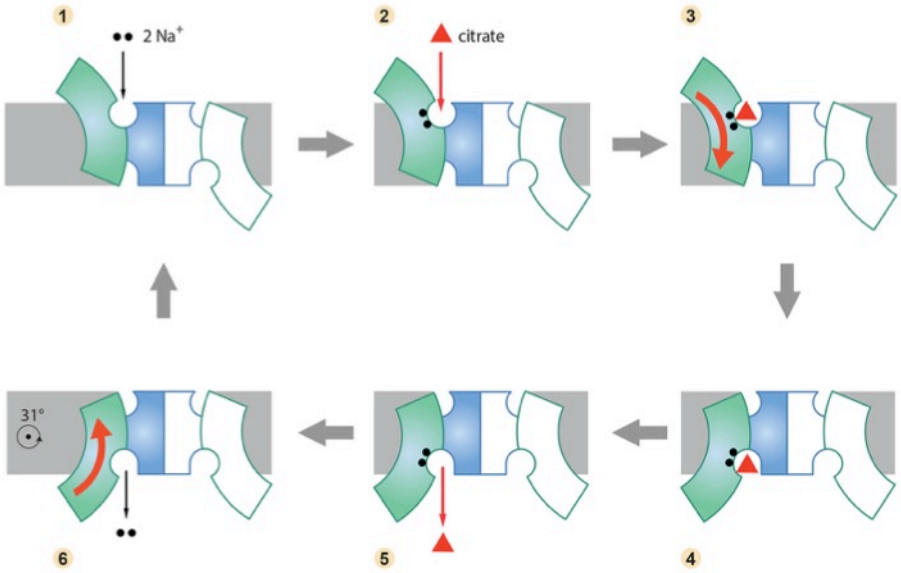

Figure 1.12: Complete proposed transport cycle of SeCitS. 1) Two sodium ions bind to the transporter in the outward conformation 2) citrate binding occurs 3) binding leads to the arc-like rotation of the helix bundle from the outward to inward conformation 4) citrate becomes hydrates and diffuses away 5) sodium ions dissociate 6) reverse arc-like rotation from inward- to outward-facing conformation without any substrates. (Wöhlert *et al.*, 2015)

Similar transport mechanisms may apply to a wide variety of related and unrelated secondary transporters, including important drug targets. While the sodium ions are occluded in the structure, citrate is not.

1.7 PROJECT AIM

Citrate and carboxylate transporters are a large and pathophysiologically important group of membrane proteins that has been studied by a multitude of structural as well as functional investigations. Over the years, a lot of information could be collected, but the SeCitS crystal structure solved in our group was a big step ahead. With the structural information, a new layer of insights could be gathered. The crystal structure also provided a valuable base for further experiments, as some of the key characteristics of the transport remain to be elucidated. One of the main aspects still in question is the origin of the high substrate specificity of the SeCitS. As described earlier, other members of the same family show much higher substrate promiscuity. Through the in-depth characterization of the transporter in its wild-type form and aided by the analysis and comparison of mutant SeCitS, a more comprehensive picture was to be obtained to allow for a better understanding of the protein.

The three central areas of study investigated in this thesis are substrate binding, transport and structure. This project features different experimental approaches to address those aspects of the transporter. The binding parameters were to be identified by isothermal titration calorimetry (ITC). Through this technique, not only the binding of citrate but also of sodium could be investigated. Transport characteristics of the protein were to be determined by reconstitution into liposomes and transport assays using radiolabeled citrate as substrate. Structural analysis was to be carried out by crystallization of SeCitS and especially its mutants and by electron microscopy, to allow for investigation of SeCitS in a more native-like environment.

2. MATERIALS AND METHODS

2.1 MATERIALS

All used reagents not mentioned in detail have been purchased from Carl Roth GmbH & Co. KG (Germany) in 'pure' or higher quality.

2.1.1 REAGENTS

^{14}C-citrate ([1,5-14C]-citric acid)	PerkinElmer LAS GmbH, Germany
Agarose UltraPure	Thermo Fisher Scientific, Germany
cOmplete Mini	
EDTA-free protease inhibitor cocktail	Roche Diagnostics, Germany
Imidazole BioUltra	Sigma-Aldrich Chemie GmbH, Germany
Monoolein	Nu-Chek Prep, Inc., USA
Detergents (DM, OG, DDM)	Anatrace Products, LLC, USA
Water TraceSELECT, for trace analysis	Riedel-de Haën, Honeywell Int Inc., USA

2.1.2 CONSUMABLES

Mini-PROTEAN TGX Precast Gels 4-15%	Bio-Rad Laboratories GmbH, Germany
NativePAGE NOVEX 3-12% Bis-Tris Gel 1.0 mm	Life Technologies GmbH, Germany
Syringe filter 0.22 µm polysulfone	Carl-Roth GmbH & Co. KG, Germany
Centriprep YM-30 concentrator	Millipore GmbH, Germany
Ultrafree Centrifugation filters	
Durapore PVDF 0.65 µm	Millipore GmbH, Germany
Amicon centrifugal filter units	Millipore GmbH, Germany
Centriprep YM-3, 10 and 30 concentrators	Millipore GmbH, Germany
MF-Millipore Membran GSWP02500	Millipore GmbH, Germany
Biobeads SM-2	Bio-Rad Laboratories GmbH, Germany
ECL Prime WB Detection System	Amersham plc, UK
QIAprep Spin Miniprep Kit	QIAGEN GmbH, Germany
QIAquick Gel Extraction Kit	QIAGEN GmbH, Germany
QIAquick PCR Purification Kit	QIAGEN GmbH, Germany

2.1.3 EQUIPMENT

ÄKTApurifier FPLC system	GE Healthcare Europe GmbH, Germany
ÄKTApure FPLC system	GE Healthcare Europe GmbH, Germany
Axiovert 40 CFL microscope	Carl Zeiss AG, Germany
Mini-PROTEAN Tetra Cell Systems	Bio-Rad Laboratories GmbH, Germany
Milli-Q Academic ultrapure water system	Millipore GmbH, Germany
XCell II Blot Module	Life Technologies GmbH, Germany
XCell SureLock Mini-Cell SDS-PAGE system	Life Technologies GmbH, Germany
Ultracentrifuge Optima X	Beckmann Coulter GmbH, Germany
Fixed angle Rotor 45 Ti	Beckmann Coulter GmbH, Germany
Lipid Extruder	Avestin Europe GmbH, Germany
Atomic absorption spectrometer	PerkinElmer LAS GmbH, Germany
Beamline PXII SLS	PSI, Switzerland
MicroCal VP-ITC	MalvernPanalytical Ltd., UK
NanoSight NS300	MalvernPanalytical Ltd., UK
Prometheus NT.48	NanoTemper Technologies GmbH, Germany
mosquito LV	SPT Labtech Ltd., UK
Tecnai Spirit BioTwin	FEI Company, USA
Titan Krios G2 Cryo-TEM	Thermo Fisher Scientific Inc., USA
Vitrobot	FEI Company, USA
ChemiDoc	Bio-Rad Laboratories GmbH, Germany
NanoDrop 1000 Spectrophotometer	Thermo Fisher Scientific, USA

2.1.4 CHROMATOGRAPHY

HiLoad 16/600 Superdex 75	GE Healthcare Germany
HisTrap IMAC FF 5 ml prepacked column	GE Healthcare Germany
Superdex 200 10/300 column	GE Healthcare Germany
Superdex 75 10/300 column	GE Healthcare Germany
Chelating Sepharose Fast Flow	GE Healthcare Germany

2.1.5 SOFTWARE AND WEBSERVERS

Origin	OriginLab Corporation
Pymol 2	Schrödinger
Adobe Illustrator CS5	Adobe Systems
Adobe Photoshop CS5	Adobe Systems
Office 2011	Microsoft Corporation
Prism 5	GraphPad

cisTEM	(Grant *et al.*, 2018)	https://cistem.org/
UCSF Chimera	(Pettersen *et al.*, 2004)	https://www.rbvi.ucsf.edu/chimera
CCP4	(Winn *et al.*, 2011)	https://www.ccp4.ac.uk/
Phenix	(Liebschner *et al.*, 2019)	https://phenix-online.org/
XDS	(Kabsch *et al.*, 2010)	https://xds.mr.mpg.de/
AIMLESS	(Evans & Murshudov, 2013)	https://www.ccp4.ac.uk/html/aimless.html
REFMAC5	(Murshudov *et al.*, 2011)	https://ucl.ac.uk/~rmhasek/refmac.html
Coot	(Emsley *et al.*, 2010)	https://www2.mrc-lmb.cam.ac.uk/personal/pemsley/coot/

Clustal Omega - Multiple sequence alignment	https://www.ebi.ac.uk/Tools/msa/clustalo/
Expasy - Nucleotide Sequence Translator	https://web.expasy.org/translate/
Uniprot - Protein Database	https://www.uniprot.org/
PDB - 3D Protein Structure Database	https://www.rcsb.org/
Oligocalc - Primer melting point calculator	http://biotools.nubic.northwestern.edu/OligoCalc.html

2.2 DNA AND CLONING

2.2.1 CONSTRUCTS

The protein sequence of *Salmonella enterica* CitS (protein accession number: WP_000183608) was used to generate an *E. coli*-optimized expression construct, which was commercially ordered from GenScript (Leiden, The Netherlands). The basic construct consisted of the protein with an N-terminal deca-histidine tag (His10-tag) and a thrombin cleavage site cloned into a pET-21d vector carrying an ampicillin resistance gene (Table 2.1). Further constructs were overall identical to the $SeCitS_{WT}$ construct but contained single and multiple point mutations (Table 2.2 and
Table 2.3). For the remainder of this thesis, the wild-type protein will be indicated as $SeCitS_{WT}$ or SeCitS in a general context, any mutants will be referenced in the text by e.g. $SeCitS_{Base}$, $SeCitS_{Inward}$ and $SeCitS_{N186A}$.

Table 2.1: Sequence of SeCitS$_{WT}$. A) Schematics of the SeCitS$_{WT}$ sequence including restriction sites (red), decahistidine Tag (His10, cyan) and Thrombin cleavage site (pink) flanking the main sequence (underscored). B) Codon-optimized nucleotide sequence of the expression construct. C) Protein sequence of SeCitS$_{WT}$ (' indicating the cleavage site).

A) **NcoI-NheI–His10–Thrombin-NdeI-SeCitS-XhoI**

B)
CCATGGCTAGCCATCACCATCACCACCATCACCACCATCACAGCAGCGGCCTGGTTCCGCGT
GGTTCTCATATGACTAATATGACTCAAGCAAGCGCCACGGAACGCAAGGGTGCAAGCGATTT
ACTGAGATTCAAGATCTTCGGTATGCCTTTACCTTTGTATGCCTTCGCGCTGATCACCCTGT
TGTTGTCTCATTTCTACAACGCTATCCCTACTGATTTAGTCGGTGGCTTTGCCTTGATGTTC
GTAATGGGTGCGATTTTCGGCGAAATCGGTAAACGCCTGCCAATCTTTAACAAGTATATTGG
TGGCGCACCGGTAATGATCTTTTTAGTTGCTGCATATTTCGTGTACGCCGGTATCTTCACAC
AAAAGGAAATCGATGCGATCTCAAACGTTATGGACAAGAGCAATTTTCTGAACCTGTTCATT
GCTGTTCTGATCACCGGTGCAATTTTATCGGTGAACCGTAAACTGTTATTGAAGAGTCTGTT
AGGCTACATTCCAACTATCCTGGCTGGCATTGTTGGTGCATCATTATTCGGCATTGTGATCG
GTTTGTGTTTTGGCATCCCTGTCGATAGAATCATGATGTTGTACGTATTGCCAATCATGGGT
GGCGGTAATGGCGCTGGTGCAGTCCCGCTGTCTGAAATTTACCACTCAGTTACGGGTCGTAG
CAGAGAAGAATATTACAGCACCGCCATTGCGATCCTGACTATTGCCAACATCTTTGCGATTA
TCTTCGCCGCGTTGCTGGACATGGTGGGTAAAAAGTATACATGGTTGTCTGGCGAAGGTGAA
CTGGTTAGAAAAGCCTCTTTTAAGACGGAAGATGACGAAAAAGCTGGTCAGATTACACATCG
CGAAACGGCAGTAGGCATGGTTCTGTCTACCACTTGCTTCTTATTGGCTTATGTTGTGGCAA
AAAAGATCCTGCCGAGTATTGGCGGTGTTTCCATCCACTACTTTGCCTGGATGGTGTTAATT
GTCGCTGCATTGAATGCGAGCGGTCTGTGTAGTCCTGAAATTAAAGCTGGCGCAAAGCGTTT
GTCCGATTTCTTTTCTAAACAACTGTTATGGGTGCTGATGGTTGGCGTGGGTGTCTGCTATA
CAGATCTGCAGGAAATTATCGACGCCTTAACGTTCGCGAATGTCGTAATTGCCGCGATTATC
GTTGTGGGTGCAGTCGTAGGCGCTGCAATCGGCGGTTGGTTAATTGGTTTTTATCCGATCGA
ATCTTCAATTACTGCCGGTTTGTGTATGGCGAACCGCGGCGGTAGTGGCGATCTGGAAGTTT
TATCCGCTTGCAATCGTATGAACCTGATCTCGTACGCACAAATTTCTTCCCGTTTAGGCGGC
GGTATCGTCTTAGTAATCGCTAGTATCGTATTTTCTATGATGGTTCTCGAGTGA

C)
MASHHHHHHHHHSSGLVP'RGSHMTNMTQASATERKGASDLLRFKIFGMPLPLYAFALITLL
LSHFYNAIPTDLVGGFALMFVMGAIFGEIGKRLPIFNKYIGGAPVMIFLVAAYFVYAGIFTQ
KEIDAISNVMDKSNFLNLFIAVLITGAILSVNRKLLLKSLLGYIPTILAGIVGASLFGIVIG
LCFGIPVDRIMMLYVLPIMGGGNGAGAVPLSEIYHSVTGRSREEYYSTAIAILTIANIFAII
FAALLDMVGKKYTWLSGEGELVRKASFKTEDDEKAGQITHRETAVGMVLSTTCFLLAYVVAK
KILPSIGGVSIHYFAWMVLIVAALNASGLCSPEIKAGAKRLSDFFSKQLLWVLMVGVGVCYT
DLQEIIDALTFANVVIAAIIVVGAVVGAAIGGWLIGFYPIESSITAGLCMANRGGSGDLEVL
SACNRMNLISYAQISSRLGGGIVLVIASIVFSMMVLE

Table 2.2: SeCitS -Cys mutations of cysteines and cross-link variants.

Residue	Mutation
base mutant:	
C165	C165S
C317	C317S
C347	C347S
C414	C414S
C278	-
C398	-
inward:	
D112	D112C
R205	R205C
outward:	
L337	L337C
S412	S412

Table 2.3: SeCitS mutations of functional residues.

Residue	Mutation
N186	N186A
	N186M
	N186V
R205	R305E
R402	R402A
	R402M
	R402Q
D407	D407N
R428	R428A
	R428E
	R428K
double/triple mutants	R402M/N186M
	R402L/N186I
	R402M/N186M/L337T

2.2.2 Polymerase Chain Reaction (PCR)

The polymerase used for polymerase chain reaction (PCR) was the Phusion polymerase (NEB, Frankfurt am Main, Germany). Primers (Table 2.4) were designed to have a predicted melting point of 52°C for the complementary sequence. For QuikChange primers, the nucleobase to be replaced was flanked by sequences of the same melting point. The melting point was calculated using OligoCalc and adjusted to terminate by either cytosine or guanine. Oligonucleotides were ordered at Eurofins (Ebersberg, Germany) and metabion (Planegg, Germany). A standard PCR reaction mix of 50 µl contained 200 µM of dNTPs, 5 µl of 10X Pfu buffer, 10-20 ng of the suitable template plasmid, respective primer oligonucleotides at a final concentration of 10 µM each and 1 U of Phusion polymerase.
A thermocycler was used for PCR reactions. The reaction cycle started with an initial denaturation (98°C, 1 min) followed by 20-35 repeats of the thermocycle itself for insert preparation and QuikChange reactions respectively. The three steps in the cycle were a denaturation step (98°C, 10 sec), an annealing step (30 sec) and the elongation step (72°C, 30 sec per 1000 bp). The annealing temperature was adapted to the primer melting temperature and set to 50°C. The PCR ended with a final elongation at 72°C for 10 min. The PCR product was purified via gel extraction or the QIAquick PCR Purification Kit in 30 µl of water.
Single point mutations in SeCitS were introduced by a classical site-directed mutagenesis protocol using forward and reverse mutagenesis primers (Table 2.4). After the described PCR, template DNA was digested with 0.2 U/µl DpnI (NEB, Ipswich, MA, USA) at 37°C for at least 3 h. The reaction was quenched by incubation of the PCR batch at 95°C for 15 min. Concluding, 10 µl of the PCR batch were introduced into 200 µl of chemocompetent *E. coli* DH5α by transformation (Section 2.2.6).

2.2.3 *Double Site Mutagenesis*

To simultaneously introduce two mutations at different sites of SeCitS, a two stage mutagenesis protocol was used, reminiscent of restriction-free cloning (Van Den Ent & Löwe, 2006). Firstly, a traditional insert PCR was run, which employed the forward mutagenesis primer of the upstream located mutagenesis site and the reverse mutagenesis primer of the downstream located mutagenesis site on the appropriate plasmid (Table 2.4). The resulting PCR product was purified with the QIAquick Gel Extraction Kit (Qiagen, Germany) according to manufacturer's instructions, where DNA was finally collected in autoclaved Milli-Q H_2O. Using a NanoDrop 1000 Spectrophotometer (Thermo Fisher Scientific, USA), its concentration was determined via absorption at 260 nm. In a second PCR, which finally introduced both mutations into the respective plasmid, hence called plasmid PCR, the PCR product assumed the function of complementary primers. Subsequently, the resulting PCR batch was subjected to DpnI digestion, employing 0.2 U/µl DpnI (NEB, USA) at 37◦C for at least 2 h. The reaction was quenched by incubation at 95◦C for 5min. Finally, 10 µl of the PCR batch were used to transform 200 µl of chemocompetent *E. coli* DH5α (Section 2.2.6). For analysis purposes, 5 µl were subjected to agarose gelelectrophoresis (Section 2.2.4).

Table 2.4: Primer list of oligonucleotides used for mutagenesis. Primer are sorted by category. The exchanged nucleotide is indicated by lower case lettering. The respective forward and reverse primer were used together to obtain the desired mutations. Triple mutants were created based on respective single mutants adding subsequent mutations.

Category	Name	Sequence
Cystein-less Variants	C278S.fwd	GGCATGGTTCTGTCTACCACTaGCTTCTTATTGG
	C398S.rev	CGCGGTTCGCCATACTcCAAACCGGCAGTAAT
	C165S.fwd	GCATTGTGATCGGTTTGaGTTTTGGCATCCCTGTC
	C317S.rev	GCTTTAATTTCAGGACTACtCAGACCGCTCGCATTCAA
	C347S.fwd	GTTGGCGTGGGTGTCaGCTATACAGATCTGCA
	C414S.rev	CAGGTTCATACGATTGCtAGCGGATAAAACTTCCAGATC
	C165V.fwd	ATTCGGCATTGTGATCGGTTTGgtTTTTGGCATCCCTGTCGATAG
	C317V.rev	CGCCAGCTTTAATTTCAGGACTaacCAGACCGCTCGCATTCAATG
	C278L.fwd	GGCATGGTTCTGTCTACCACTctgTTCTTATTGGCTTATGTTGTGGC
	C398A.rev	CGCCGCGGTTCGCCATagcCAAACCGGCAGTAATTGAAGATTC
Cystein-Cross-links	D112C.fwd	GCGATCTCAAACGTTATGtgCAAGAGCAATTTTCTGAACC
	R205C.rev	CGGTGCTGTAATATTCTTCgcaGCTACGACCCGTAACTG
	A302C.fwd	GTGTTTCCATCCACTACTTTtgCTGGATGGTGTTAATTGTC
	V436C.rev	GAAAATACGATACTAGCGATgcaTAAGACGATACCGCCGC
	L337C.fwd	GATTTCTTTTCTAAACAACTGtgcTGGGTGCTGATGGTTGG
	S412C.rev	GTTCATACGATTGCTAGCGcATAAAACTTCCAGATCGCC
Single Point Mutants	N186A.fwd	CCAATCATGGGTGGCGGTgcgGGCGCTGGTGCAGTCC
	N186A.rev	GGACTGCACCAGCGCCcgcACCGCCACCCATGATTGG
	N186M.fwd	CCAATCATGGGTGGCGGTatgGGCGCTGGTGCAGTCC
	N186M.rev	GGACTGCACCAGCGCCcatACCGCCACCCATGATTGG
	N186V.fwd	CCAATCATGGGTGGCGGTgtTGGCGCTGGTGCAGTCC
	N186V.rev	GGACTGCACCAGCGCCAacACCGCCACCCATGATTGG
	R205E.fwd	CAGTTACGGGTCGTAGCgaAGAAGAATATTACAGCACCG
	R205E.rev	CGGTGCTGTAATATTCTTCTtcGCTACGACCCGTAACTG
	R402A.fwd	CCGGTTTGTGTATGGCGAACgcgGGCGGTAGTGGCGATCTG
	R402A.rev	CAGATCGCCACTACCGCCcgcGTTCGCCATACACAAACCGG
	R402M.fwd	CCGGTTTGTGTATGGCGAACatgGGCGGTAGTGGCGATCTG
	R402M.rev	CAGATCGCCACTACCGCCcatGTTCGCCATACACAAACCGG

	R402Q.fwd	CGGTTTGTGTATGGCGAACCagGGCGGTAGTGGCGATCTG
	R402Q.rev	CAGATCGCCACTACCGCCctgGTTCGCCATACACAAACCG
	D407N.fwd	CGCGGCGGTAGTGGCaatCTGGAAGTTTTATCCGCTTGC
	D407N.rev	GCAAGCGGATAAAACTTCCAGattGCCACTACCGCCGCG
	R428A.fwd	GTACGCACAAATTTCTTCCgccTTAGGCGGCGGTATCG
	R428A.rev	CGATACCGCCGCCTAAggcGGAAGAAATTTGTGCGTAC
	R428E.fwd	GTACGCACAAATTTCTTCCgaaTTAGGCGGCGGTATCG
	R428E.rev	CGATACCGCCGCCTAAttcGGAAGAAATTTGTGCGTAC
	R428K.fwd	GTACGCACAAATTTCTTCCaaaTTAGGCGGCGGTATCG
	R428K.rev	CGATACCGCCGCCTAAtttGGAAGAAATTTGTGCGTAC
	N186I.fwd	CCAATCATGGGTGGCGGTAtTGGCGCTGGTGCAGTCC
	N186I.rev	GGACTGCACCAGCGCCAaTACCGCCACCCATGATTGG
Triple Mutants (Additional)	R402L.fwd	CGGTTTGTGTATGGCGAACCtgGGCGGTAGTGGCGATCTG
	R402L.rev	CAGATCGCCACTACCGCCcaGGTTCGCCATACACAAACCG
	L337T.fwd	GTCCGATTTCTTTTCTAAACAACTGaccTGGGTGCTGATGGTTGGC
	L337T.rev	GCCAACCATCAGCACCCAggtCAGTTGTTTAGAAAAGAAATCGGAC

2.2.4 DNA AGAROSE GEL AND GEL PURIFICATION

DNA fragments and plasmids were separated from primers via agarose gel electrophoresis. Agarose was prepared with ethidium bromide (0.5 µg/ml) and 50X TAE buffer and the mixture was cast in a gel chamber and allowed to solidify. 6X DNA sample buffer was added to the sample (PCR insert, vector, restriction mixture) and loaded onto the gel, as well as a reference standard (1 kb DNA Ladder). The run was performed at 90 V with time depending on the size of the samples (60 min for vectors, 30 min for inserts). DNA was visualized under UV light and desired bands were cut out of the gel. DNA was purified using the QIAquick Gel Extraction Kit according to the instructions in the manual.

2.2.5 COMPETENT CELLS

E. coli strains BL21-C41(DE3) and BL21-C43(DE3) were used for expression of SeCitS protein and strain DH5α for cloning. Competent cells were produced (Hanahan, 1983), starting with the inoculation of 2xYT medium (100 ml, Table 2.6). After an optical density ($OD_{600\ nm}$) of 0.5 was reached, the cells were chilled on ice for 15 minutes and pelleted at 4 000 g and 4°C for 5 minutes. The pellet was resuspended in 35 ml of ice-cold RF1 buffer and incubated on ice for 15 minutes. Subsequently the cells were pelleted as described above and resuspended in 8 ml of ice cold RF2 buffer and incubated on ice. After 15 minute the cells were aliquoted (200 µl each), flash-frozen in liquid nitrogen and stored at -80°C until further use.

Table 2.5: Buffers for competent cells.

RF1	pH 5.8 (AcOH)
RbCl	100 mM
$MnCl_2$	50 mM
KAc	30 mM
$CaCl_2$	10 mM
glycerol	15%

RF2	pH 6.5 (KOH)
MOPS	10 mM
RbCl	10 mM
$CaCl_2$	75 mM
glycerol	15%

2.2.6 TRANSFORMATION

Competent cells were thawed on ice for 5 minutes. 10 ng of plasmid DNA from mini preparations or 50 ng of QuikChange-PCR product were mixed with the cells and incubated for 20 minutes on ice. After a heat shock of 42°C for 45 seconds, the cells were supplemented with 1 ml of SOC medium (Table 2.6) and shaken for 30 minutes at 37°C. After spinning down the cells at 4 000 g for 5 minutes, the volume was reduced, and the cells were transferred onto agar plates supplemented with ampicillin (Table 2.6). Single colonies were visible after incubation at 37°C overnight.

Table 2.6: Media and media components.

LB (1 l)	
Tryptone	5 g/l
Yeast extract	10 g/l
NaCl	10 g/l

2xYT (1 l)	pH 7.0 (NaOH)
Tryptone	16 g
Yeast extract	10 g
NaCl	5 g

Autoinduction medium	
Tryptone	1%
Yeast extract	0.5%l

50x5052	
Glycerol	25% (w/v)
Glucose	2.5% (w/v)
Lactose	10% (w/v)

Trace elements	
Solution 1	2x
$CaCl_2$	40 mM
$MnCl_2$ / $ZnSO_4$ (each)	20 mM
$CoCl_2$ / $CuCl_2$ / $NiCl_2$ / Na_2MoO_4 / Na_2SeO_4 / H_3BO_3 (each)	4 mM

SOC	
Tryptone	2% w/v
Yeast extract	0.5% w/v
NaCl	10 mM
KCl	2.5 mM
$MgCl_2$	10 mM
Glucose	20 mM

LB Agar (plates) (1 l)	
Tryptone	10 g
Yeast extract	5 g
NaCl	10 g

50xM9	
Na_2HPO_4	1.25 M
KH_2PO_4	1.25 M
NH_4Cl	2.5 M
Na_2SO_4	0.25 M

Solution 2	2x
$FeCl_3$	100 mM
HCl	100 mM

2.2.7 DNA PREPARATION

For plasmid DNA preparation, mini-cultures of transformed DH5α cells were grown in test tubes with 5 ml LB medium supplemented with 0.1 mg/ml ampicillin. The culture, inoculated with a single colony from an agar plate, was grown for 8-16 hours. The plasmid DNA was extracted from the cells using the QIAprep Spin Miniprep Kit (Qiagen). The concentration was determined via absorption at 260 nm using a Nanodrop 1000 spectrophotometer

(ThermoFisher). The sequence of the DNA was verified by using the sequencing service by Microsynth (Balgach, Switzerland).

2.2.8 Glycerol Stocks

Glycerol stocks were prepared using LB medium (Table 2.6) inoculated with a single colony from an agar plate. The culture was grown to an optical density ($OD_{600\,nm}$) of 0.6. 0.5 ml of cells were mixed with an equal amount of glycerol and frozen in liquid nitrogen for storage at -80°C.

2.3 Protein Purification and Analysis

2.3.1 Protein Expression

For large-scale expression of $SeCitS_{WT}$ and its mutants *E. coli* BL21-C41(DE3) cells were grown in auto-induction medium (Table 2.6). Precultures of expression constructs were prepared by inoculation of 300 ml LB using either an agar plate colony or a glycerol stock and grown overnight. The standard expression volume was six flasks (5 l, baffled) with 2 litres of medium each. The expression medium was prepared by adding 20 ml 50xM9, 20 ml 50x5052, 200 µl trace elements, 2 ml magnesium sulphate (1 M), 1 ml ampicillin (100 mg/ml) and 25 ml of the preculture per litre medium. Cells were grown at 37°C and 130 rpm for 8-10 hours and harvested by centrifugation at 10 000 g for 7 minutes. The cell pellet was collected and frozen at -20°C.

2.3.2 Protein Purification

The thawed cell pellet was resuspended in 250 ml lysis buffer (Table 2.7) supplemented with DNase, lysozyme, protease inhibitor (1 pill cOmplete, Roche) and 2.5 mM β-mercaptoethanol (β-ME). After Dounce homogenization and filtration, the cells were disrupted in three passages at 8 MPa using a microfluidizer (Microfluidics Corp.). To remove cell debris, the lysate was centrifuged at 20 000 g and 4°C for 30 minutes. The supernatant was subjected to an ultracentrifugation step (1 h at 100 000 g and 4°C) to harvest crude membranes. The membrane pellet was resuspended in membrane buffer to a concentration of 15 mg/ml total protein. An expression of 12 l routinely yielded two aliquots of 45 ml of crude membranes which were flash-frozen in liquid nitrogen and stored at -80°C.

Table 2.7: Buffers for protein purification.

Lysis buffer	pH 7.4
Tris	20 mM
NaCl	100 mM
NaCitrate	1 mM
EDTA	5 mM

Solubilization buffer	pH 7.4
Tris	20 mM
NaCl	150 mM
NaCitrate	2 mM
DM	1.2-1.5 g
Glycerol	30%

Thrombin cut buffer	pH 8.2
Tris	20 mM
NaCl	150 mM
NaCitrate	1 mM
DM	0.15%
$CaCl_2$	2.5 mM

Gel filtration buffer	pH 7.4
Tris	20 mM
NaCl	150 mM
DM	0.15%
TCEP	1 mM
(NaCitrate	1 mM)

Membrane buffer	pH 7.4
Tris	20 mM
CholineCl	140 mM
NaCitrate	1 mM
Succrose	250 mM
TCEP	1 mM

Equilibration buffer	pH 7.4
Tris	20 mM
NaCl	300 mM
NaCitrate	1 mM
DM	0.15%
Imidazole	45 mM

Washing buffer	pH 8.2
Tris	20 mM
NaCl	300 mM
NaCitrate	1 mM
DM	0.15%

The crude membranes were mixed 1:1 with solubilisation buffer containing ~3 % decylmaltoside (DM) and 0.5 % β-ME, subjected to one freeze-thaw cycle and incubated under agitation for at least 2 h at 4°C. The solubilisate was centrifuged at 100 000 g and 4°C for 1 h. A slurry of 5 ml chelating sepharose beads (Fast Flow, Sigma-Aldrich) loaded with nickel was equilibrated and mixed with the supernatant, which was then adjusted to 45 mM imidazole using a 2 M stock solution. After binding for 2 h at 4°C, the mixture was loaded onto an empty column and a gel sample of the flow-through was collected. The column was washed with equilibration buffer (50 ml) and cutting buffer (80 ml), taking gel samples at every step. 5 ml of cutting buffer containing 6 U of thrombin (Sigma-Aldrich) were cycled over the column overnight to cleave the protein off its His10-tag. On the next day the cleaved protein was collected. Additionally, the column was washed with cutting buffer (5 ml) and washing buffer (10 ml) to elute remaining protein from the column. Next, the protein was concentrated to 600 µl using a 30 kDa cut-off concentrator. After filtration through a 200 nm filter the sample was applied to a gel filtration column (Superdex 200 10/300 GL, GE LifeSciences) equilibrated with gel filtration buffer. Fractions were collected and checked on a SDS-PAGE for purity. The fractions containing the protein were pooled and concentrated to 5 mg/ml using a 30 kDa cut-off concentrator. The protein was aliquoted and flash frozen in liquid nitrogen for storage at -80°C.

2.3.3 *UNCLEAVED HISCITS*

The wild-type protein was also used in its uncleaved His10-tagged form, $SeCitS_{His}$. After application of the bead-solubilisate mixture to the column, the column was washed with equilibration buffer (50 ml) and the protein eluted with 2 x 10 ml of equilibration buffer containing 250 mM imidazole. The eluate was dialysed against gel filtration buffer overnight. After concentrating to 600 µl, the sample was subject to gel filtration like the sample without a His-tag. Pure $SeCitS_{His}$ was aliquoted and flash frozen in liquid nitrogen at -80°C.

2.3.4 *BLUE NATIVE PAGE*

Samples for blue native PAGE were prepared by mixing 5 µg of protein and 4X NativePAGE sample buffer to a final volume of 20 µl. In the sample the detergent concentration was adjusted to 0.5% DM and the Coomassie brilliant blue G-250 concentration to 0.125%. Samples containing 1% SDS were used to disrupt potential oligomers as a reference.
A NativPage gel (4-16% Bis-Tris 1,0mm X 15well, Invitrogen) was used and the blue native PAGE was conducted according to the instructions of the NativePAGE Novex BisTris Gel System (Invitrogen). The anode buffer was changed to 25 mM imidazole (Wittig *et al.*, 2006).

2.3.5 *SDS-PAGE*

Self-cast gels were prepared in a Bio-Rad gel apparatus, starting with the separating gel (10%). To achieve an even surface during polymerization, isopropanol was layered over the separating gel. After 15 minutes, the isopropanol was removed and the stacking gel (4%) poured, the comb inserted and left for polymerization.
Samples were taken from different steps of the purification. 2X loading dye was added to the samples and 20 µl of sample were used per lane. The PageRuler Prestained Protein Ladder (Thermo Scientific) was used as reference marker. Electrophoresis was carried out at a constant current of 30 mA per gel.
To stain the gel, it was heated in solution 1 and rocked for 5 minutes at room temperature. Solution 1 was replaced with solution 2 supplied with 200 µl of 0.25% Coomassie brilliant blue. The gel was heated to near boiling and incubated overnight for a good staining result.

Table 2.8: Solutions for SDS-PAGE and staining.

Separating gel	15 ml
H_2O	7.22 ml
1.5 M Tris pH 8.8	3.75 ml
40% Acrylamide	3.75 ml
10% SDS	150 µl
10% APS	105 µl
Temed	26.25 µl

Stacking gel	5 ml
H_2O	3.77 ml
1.5 M Tris pH 6.8	625 µl
40% Acrylamide	500 µl
10% SDS	50 µl
10% APS	40 µl
Temed	6 µl

Solution 1 (fixing)	
Ethanol	50%
Acetic acid	10%

Solution 2 (staining)	
Ethanol	5%
Acetic acid	7.5%

2.3.6 *Western Blot*

For Western blot analysis, self-cast gels as for SDS-page (Section 2.3.5) or precast gradient gels were used. The PageRuler Prestained Protein Ladder (Thermo Scientific) and additionally a HIS-marker (BenchMark, Invitrogen) were used as reference markers. Sample preparation and electrophoresis were carried out as before. The gel was subjected to a semi-dry blotting onto pre-cut polyvinylidene fluoride (PVDF) membrane (Immobilon-P, 0.45 µm, Merck, Germany) at 140 mA (max 25 V) for 35 minutes. The layering setup was anode – two anode buffer I soaked Whatman papers – one anode buffer II soaked Whatman paper – methanol activated PVDF membrane – SDS-PAGE, equilibrated in cathode buffer – three cathode buffer soaked Whatman paper – cathode. The blots were blocked with 5% bovine serum albumin (BSA) in TBS-T (Tris buffered saline with Tween) for 1 h at room temperature. The first antibody was added at a 1:1 000 dilution in 5% BSA in TBS-T and incubated overnight at 4°C. After washing the blot thrice, the second antibody was added (1:2 000 dilution in TBS-T) and after 1 h incubation the blot was analysed. The blots were developed either with alkaline phosphatase substrate (Sigmafast BCIP/NBT, Sigma) or Western Blot Signal Enhancer (ECL Start, Sigma) and visualized on a ChemiDoc MP Imaging System (BioRad).

Table 2.9: Buffers for Western blotting.

Anode Buffer I	pH 10.4 (HCl)
Tris	300 mM
MeOH	10% (v/v)

Anode Buffer II	pH 10.4 (HCl)
Tris	25 mM
MeOH	10% (v/v)

Cathode buffer	pH 9.4 (HCl)
Tris	25 mM
MeOH	10% (v/v)
Glycine	40 mM

TBS-T	pH 7.5 (HCl)
Tris	10 mM
NaCL	150 mM
Tween20	0.05% (v/v)

A Western blot was also used to normalize the protein concentration in cells used for the cell-based transport assay. Equal amounts of cells at the same OD were harvested and resuspended in 2X loading dye. The samples were run and blotted like other samples with special care during application of the samples to the gel due to a high viscosity. Intensities of bands in the developed Western blots were quantified to normalize the protein concentration.

2.3.7 *Protein Concentration Determination*

The concentration of protein solutions was measured by different techniques depending on the circumstance and accuracy needed.

Total protein concentration of membranes and quick approximations of protein concentration of purified protein was measured using a commercial Bradford solution (Bradford Reagent, Sigma). Absorption at 280 nm using a spectrophotometer

(BioPhotometer Plus, Eppendorf) was routinely used to measure isolated protein. For high accuracy protein concentration measurements for ITC, a BCA assay was performed (BCA Protein Assay, Thermo Scientific). Commercial assays were carried out according to the supplier's instructions.
To verify the concentration measured by BCA for ITC measurements, samples of the protein were sent to the Functional Genomics Center Zurich (University/ETH Zurich) for an amino acid analysis performed by Dr. Peter Hunziker.

2.4 TRANSPORT ASSAY

2.4.1 SECITS RECONSTITUTION INTO PROTEOLIPOSOMES

Purified SeCitS protein was reconstituted in liposomes for radioactive transport assays. 1 ml of *E. coli* polar lipids (20 mg/ml, Avanti Polar Lipids, Alabaster, USA) were dried under nitrogen flow and resuspended in 1 ml of reconstitution buffer containing 15 mM of β-mercaptoethanol. The mixture was extruded through a 400 nm filter to form unilamellar, similarly sized vesicles. The vesicles were diluted to 5 mg/ml and n-octyl-β-D-glucopyranoside (OG, 20%) was slowly added to destabilize the vesicles. The destabilization was monitored by light scattering at 540 nm and the optimum was achieved at the biggest decrease is scattering at about 1% of OG. The vesicles were aliquoted at 2 ml. One sample was left without protein for reference and the other aliquot was supplemented with protein (5 mg/ml) to reach a lipid to protein ratio (LPR) of 50. After incubation for one hour at room temperature, samples were transferred to dialysis bags with a 14 kDa cut off and placed in 200 ml of reconstitution buffer for overnight dialysis. To eliminate all detergent, 1.2 g of absorbent Bio-Beads SM-2 (Bio-Rad) were added to the dialysis buffer. The dialysed proteoliposomes were pelleted by ultracentrifugation at 200 000 g and 22°C for 25 minutes. The vesicles were resuspended in 600 µl reconstitution buffer for washing and again centrifuged as before. The vesicle pellet was then resuspended in 160 µl reconstitution buffer (lipid concentration 50 mg/ml) for further use.

Table 2.10: Buffers for proteoliposome reconstitution and transport assays

Reconstitution buffer	pH 6.0 (HCl)
Tris	20 mM
Bistris	20 mM
Acetic acid	20 mM
CholineCl	50 mM

Washing buffer	pH 6.0 (HCl)
Tris	20 mM
Bistris	20 mM
Acetic acid	20 mM
NaCl	50 mM

Reaction buffer	pH 6.0 (HCl)
Tris	20 mM
Bistris	20 mM
Acetic acid	20 mM
NaCl	50 mM
[1,5]^{14}C-citric acid	5 mM

2.4.2 *Analysis of Proteoliposomes*

The reconstitution efficiency was checked by freeze-fracture. Proteoliposomes were applied between two copper platelets and plunge-frozen in liquid ethane to achieve a thin layer of frozen sample. The sample was fractured and shaded with 3 nm platinum/carbon in an angle of 45°. The indentation was intensified with 24 nm carbon at an angle of 90°. Throughout the fracture and shading process the sample was kept at -130°C. The pressure for shading and enhancement was ~$7x10^{-7}$ mbar (BAF 060 freeze-fracture system, BAL-TEC). The samples were thawed in 45% chrome sulfuric acid to remove any organic residues and rinsed with water. These carbon replicas were placed on a Formvar coated 300 mesh copper TEM Grid and imaged. The analysis was done on an electron microscope (EM 208S, 80 kV, FEI). The freeze-fracture was performed by Friederike Joos and Mark Linder.
As a second means of analysis the particles were analysed with a NanoSight LM10 instrument (Malvern, Kassel, Germany). This particle-tracing device allows the determination of the size distribution of the proteoliposomes. Different preparations of proteoliposomes were tested. Samples were either prepared by filtration through a 400 nm filter, by three freeze-thaw cycles or sonication to eliminate multilamellar vesicles. Liposomes with and without protein were injected and measured for 30 seconds. The results include a statistical analysis of the amount of particles at the respective sizes. The measurement was performed with the help of Michael Urban.

2.4.3 *Amido Black Assay*

The amido black assay was used to determine the protein concentration in proteoliposomes. As a standard, BSA was used, and each filter membrane included a standard series with 1 mg, 2 mg, 5 mg and 10 mg of BSA. 5 µl of the liposome sample were diluted with water to a final volume of 225 µl. After the addition of 30 µl of 1 M Tris/HCl pH 7.4 with 2% SDS and 50 µl 90% trichloracetic acid (TCA), the solution was mixed vigorously and incubated for 2 minutes at room temperature on a shaker.

Table 2.11: Solutions for the amido black assay

Staining solution	
Amido Black	0.25% w/v
Methanol	45% v/v
Acetic acid	10% v/v

Destaining solution	
Methanol	90% v/v
Acetic acid	2% v/v

Elution solution	
NaOH	25 mM
EDTA	50 µM
Ethanol	50% v/v

The solution was then filtered onto a nitrocellulose membrane (pore size 0.45 µm) and washed with 6% TCA. Then the filter was incubated with the staining solution for 10 minutes. After washing the membrane with water, the destaining solution was added twice for 2 minutes each. After washing once again with water, the membrane was dried, protein spots were cut and placed into reaction cups filled with 1 ml elution solution. After

15 minutes of shaking, the solution was vortexed and decanted into cuvettes. Absorption was measured at 630 nm. The protein concentration in liposomes was determined by correlating the absorption of the sample to the standard curve of BSA. Samples were measured in duplicates.

2.4.4 *Radioactive Transport Assay*

Freshly prepared proteoliposomes were used for radioactive transport assays. The standard measuring conditions were a reaction buffer at pH 7 with 50 mM NaCl and 5 µM [1,5]^{14}C-citric acid. A filter plate apparatus was used for the transport assays. A connected vacuum pump enabled a fast stop of the reaction. Nitrocellulose filters (0.2 µm) were soaked in washing buffer before the start of the reaction.
The reaction mix was prepared with radioactive citrate and transferred to a reaction cup. The time-dependent reaction of citrate transport started upon the addition of the proteoliposomes at 1 µl per 100 µl reaction mix (generally a total volume of 880 µl for four timepoints). At discrete time points, 200 µl of sample were taken from the mix, applied to the filter and washed thrice with washing buffer to terminate the reaction. Typical time steps were 15, 30, 45 and 60 seconds. The filters were then transferred into scintillation vials. After the addition of 4 ml of scintillation fluid (Rotiszint, Carl Roth, Karlsruhe, Germany), the entrapped [1,5]^{14}C-citrate was determined by liquid scintillation counting. Experimental values were corrected by measuring empty liposomes or measurement with choline instead of sodium as non-transported cation. Substrate specificity was tested by adding 100 mM of the alternative substrate or cold citrate to the standard reaction mix. A single set of measurements consisted of 3 to 5 time points within the linear range of the uptake. A linear regression fit was applied to the data to obtain the transport rate. The experiment was repeated thrice, and the rates were averaged. Using the protein concentration acquired by amido black assay (Section 2.4.3), the rates were correlated, and specific and relative transport activity were determined.

2.4.5 *Cell-based Transport Assay*

E. coli BL21-C43(DE3) cells were transformed with wild-type or mutant plasmid. From a single-colony preculture, a culture of 100 ml was inoculated at an optical density (OD) at 600 nm of 0.3. The culture was grown to OD 1.0 and then protein expression was induced with 2 mM IPTG for 2 hours. Cells were harvested by centrifugation at 5 000 g for 5 minutes, washed with choline buffer (20 mM Bis-Tris pH 7.0, 50 mM choline chloride) and concentrated to OD 20 for further use.
The samples were measured as described for proteoliposomes (section 2.4.4). Transport was initiated by the dilution of cells to an OD of 2 in the reaction mix. The filters used here were cellulose filter with a pore size of 0.45 µm and the time points adjusted to 30, 60, 120 and 180 seconds. Measurement and analysis of the data was performed as for the proteoliposome assay. Activity of the mutants was normalized to the transport activity of wild-type protein.

Table 2.12: Buffers for cell-based transport assays

Cell buffer	pH 7.0 (HCl)
Bistris	20 mM
Acetic acid	20 mM
CholineCl	50 mM

Washing buffer	pH 7.0 (HCl)
Bistris	20 mM
Acetic acid	20 mM
NaCl	50 mM

Reaction buffer	pH 6.0 (HCl)
Bistris	20 mM
Acetic acid	20 mM
NaCl	50 mM
[1,5]^{14}C-citric acid	5 mM

2.5 ITC

2.5.1 CITRATE MEASUREMENTS

Without added citrate in the buffers, 3 mg of purified protein were run over a size-exclusion column (Superdex 200 Increase 10/300 GL, GE Healthcare, Freiburg, Germany) and peak fractions were dialysed twice against ITC buffer to obtain substrate-free protein (1:50 v/v). The protein sample was then sterile filtered, degassed and subjected to the titration. The resulting concentration was between 20-50 µM of monomer. The syringe was filled with ITC buffer supplemented with citrate (0.5 mM). Protein concentration of the final sample was first estimated by absorption at 280 nm and subsequently determined by BCA assay.
A titration was routinely run with a preinjection of 4 µl, followed by 26 injections of 10 µl within 20 sec spacing on a speed of 372 rounds per minute (rpm). Data was analysed using Origin software (OriginLabs, Northampton, MA, USA). A fit curve with a single site binding mode (One Set of Sites) was used to model the data. The Hill coefficient was not a restricted parameter to determine the binding mode.

Table 2.13: Buffers for citrate titrations in ITC measurements

Protein buffer (Citrate)	
Buffer	20 mM
NaCl	100 mM
DM	0.15%
TCEP	1 mM

Injectant	
Citrate	0.5 mM
Buffer	20 mM
NaCl	100 mM
DM	0.15%
TCEP	1 mM

Buffer substances	
MES	pH 5.9 – 6.0
Bistris	pH 6.5
HEPES	pH 7.4

2.5.2 *Sodium-free Samples*

A number of measures had to be taken to ensure a SeCitS sample with sodium concentrations below 1 µM. If a new batch of protein was prepared, the last size-exclusion buffer was altered in composition to only include 75 mM NaCl instead of 150 mM containing additional 75 mM KCl. The sample was then dialysed against sodium-free buffer. Buffer for the dialysis was prepared in plastic cylinders and stored in falcon tubes to avoid sodium contamination by glassware. All buffer components were tested for their sodium concentration by atomic absorption spectroscopy. The titration was carried out in a similar manner to the citrate measurement with 26 injections of 10 µl with 20 sec on a speed of 372 rpm. The syringe was filled with buffer containing 90 mM NaCl. Titrations were carried out with and without citrate in the protein sample in the cell.

Table 2.14: Buffers for ITC sodium binding experiments

Protein buffer (Sodium)	
Bistris pH 6.5	20 mM
CsCl	90 mM
DM	0.15%
TCEP	0.5 mM
(Citrate	0.2 mM)

Dialysis membrane buffer	
Bistris pH 6.5	20 mM
CsCl	90 mM

Injectant	
Bistris pH 6.5	20 mM
NaCl	90 mM
DM	0.15%
TCEP	0.5 mM

Injectant (Citrate)	
Citrate	0.5 mM
Bistris pH 6.5	20 mM
NaCl	17 mM
CsCl	73 mM
DM	0.15%
TCEP	0.5 mM

2.6 Crystallization and Data Processing

2.6.1 *Crystallization Setup*

SeCitS wild-type and mutant protein at 5 mg/ml was mixed with 1% OG. A 24-well plate was used to set up a fine screen of similar conditions of 100 mM MES pH 6.5 with 100-250 mM NaCl and 27-31% PEG 400. Protein samples were diluted 1:1 with reservoir solution as hanging drops (2 µl +2 µl over 400 µl). After one week, different crystals especially long needle-like crystals (400 µm) were visible. The crystals were vitrified in liquid nitrogen using a 50:50 (v/v) mixture of paraffin and silicon oil as cryo protectant. All crystals were checked in the X-ray Beam and datasets collected at the Swiss Light Source (SLS, Paul-Scherrer-Institut, Villingen, Switzerland) on beamline X10SA (PXII).

2.6.2 *Lipid Cubic Phase Crystallization*

For crystallization trials in lipid cubic phase (Caffrey & Cherezov, 2009), SeCitS was first concentrated to 20 mg/ml. Monoolein was thawed at 37°C and transferred to a preheated syringe. Another syringe was filled with protein solution to result in a 3:2 ratio (v:v) of monoolein to protein. The syringes were coupled, and the contents mixed thoroughly while maintaining a constant temperature. The syringes were attached to a mosquito® LV pipetting robot (SPT Labtech, Melbourn, UK). To test a wide range of crystallization conditions, the commercial screens MB Class I (50%, water dilution) and MemGold (70%, water dilution) were used (QIAGEN, Hilden and Molecular Dimensions, Sheffield, UK, respectively). The 96-well plate containing the screen and the LCP glass plate mounted on the pipetting robot. 100 nl of screen solution were added to 10 nl of protein-monoolein mixture. The LCP plate was sealed and kept horizontally at 20.5°C. To find crystals, the plates were checked with white and UV light and crystals with sharp edges and green fluorescence under UV-light were selected. The crystals were retrieved using a glass cutter and were flash-frozen in liquid nitrogen. The crystals were checked at the SLS beamline in the same way as normal crystals.

2.6.3 *Data Processing*

The datasets were processed with XDS (Kabsch *et al.*, 2010) and scaled with *AIMLESS* (Evans & Murshudov, 2013). Molecular replacement with $SeCitS_{WT}$ (pdb: 5A1S) was used for phasing. Phenix (Liebschner *et al.*, 2019) and refmac5 (Murshudov *et al.*, 2011) were used for refinement and model was build in *Coot* (Emsley *et al.*, 2010). To compare ligand occupancy, omit maps were created with and without ligand in a final refinement step. Figures were created with PyMOL 2 (Schrödinger LLC, 2015).

2.7 Lipoprotein Nanoparticle Preparation

2.7.1 *Nanodiscs*

Nanodiscs were formed by using MSP1E3D1 with brain polar lipids and $SeCitS_{His}$. Initial experiments testing different ratios of components were performed by Lisa Klatt (Klatt, 2017). Best results were obtained with mixing all components at a MSP:protein:lipid molar ratio of 2:1:100 and incubation for 1 h at room temperature. The preformed nanodiscs were applied to a 1 ml HisTrap column to separate empty and loaded nanodiscs via the His-tagged SeCitS. Elution was performed with a stepwise imidazole gradient to 200 mM. The pooled peak elution fractions (3-5) were applied to a Superdex200 5/150 column to obtain uniform nanodiscs with HisCitS loaded. The peak fraction was used for freezing grids for cryo-EM so adjacent fractions were used to analyse the sample in a BN page along with samples collected during earlier preparation steps and a sample supplemented with added 1 % SDS.

2.7.2 *Saposin Purification*

The cell pellet of Origami2 *E. coli* cells (Sigma Aldrich, Taufkirchen, Germany) was resuspended in saposin lysis buffer containing DNase I, lysozyme and cOmplete protease inhibitor. After breaking the cells with a microfluidizer, cell debris was removed by centrifugation (30 min at 20 000 g). The supernatant was subjected to a heat shock of 10 minutes at 85°C and, to remove protein aggregates and the sample was centrifuged again. The sample was applied to Ni-loaded chelating sepharose column. After washing, protein was eluted with buffer containing 400 mM imidazole. Supplied with 20 U of thrombin, the sample was dialysed against 2 l buffer overnight in a 4 kDa cut-off membrane. After concentration, the sample was subjected to gel filtration over a Superdex 75 (10/300) column. Peak fractions were collected, flash frozen and stored at -20°C.

2.7.3 *Saposin Nanoparticle Production*

Samples of SeCitS in saposin nanoparticles were tested and optimized by Lisa Klatt (Klatt, 2017). To form nanoparticles of saposin with SeCitS, different lipids, incubation times, temperatures and lipid to protein ratios were tested. The preparation with the best results is described.
DDM-solubilised lipid and saposin were incubated with SeCitS for 60 minutes at a 300:20:1 molecular weight ratio. Afterwards the detergent was removed with the direct addition of Bio-Beads SM-2 for 15 minutes. The sample was run over an appropriately sized Superdex 200 column (either 3.2/300 or 10/300). The peak fractions were used for electron microscopy.

2.8 Electron Micoscopy

2.8.1 *Negative-Stain*

Samples for negative-stain analysis included SeCitS in detergent, in nanodiscs and as saposin nanoparticles and were used at concentrations of about 1-2.5 mg/ml. 3 µl of sample was applied to SPI Super Grids 400 Mesh Copper grids (SPI supplies, West Chester, USA) and incubated for 1 minute. Excess solution was wicked with filter paper and 5 µl uranyl acetate-staining solution (1%) was added. After another 1-minute incubation the excess was wicked away and the sample washed thrice with droplets of water. Samples were stored and later analyzed on a TECNAI Spirit BioTwin 120 keV (FEI, Hillsboro, USA) microscope.

2.8.2 CRYO-EM

SeCitS in nanodiscs was used at a concentration of 1.2 mg/ml. C-Flat CF-2/2-4Cu grids were used, and glow-discharged twice. For plunge-freezing, a Vitrobot (ThermoFisher Scientific) was used. 2 µl of sample were applied to the mounted grids, blotted for 11 seconds with a blot force of -1 and flash frozen in liquid ethane. The grids were transferred to liquid nitrogen for storage. The grids were analysed on a Titan Krios G2 (Thermo Fisher Scientific, Waltham, USA) electron microscope with a K2 camera at a magnification of 200 000 and a pixel size of 1.14 Å. 1500 images with a defocus range of -2 µm to -3 µm were collected with automated data collection (EPU). The dataset was analysed with cisTEM and images were generated with Chimera.

3. Results and Discussion

A broad set of information on the citrate symporter from previous experiments laid the groundwork for this thesis. Based on those findings and with the information obtained from the crystal structure, a set of experimental approaches was conceived.
To gain a deeper understanding of SeCitS dimerization and to study the interdependence and conformational distribution within the transporter, a combined functional and structural approach was applied. Studying the transport activity and the binding of the substrates to SeCitS would deepen the understanding of the properties of the transporter. Using the insights gained from the crystal structure, a set of relevant residues was devised for mutagenesis to study transport properties and for structural analysis.

3.1 Investigating Functional Interdependence within the Dimer

In our previous experiments, no cooperativity of citrate transport activity between the SeCitS protomers was identified (Grötzinger, 2014). Structurally the dimer exhibits a high stability in its multimerization. The crystal structure shows a very tight interaction of the two protomers, featuring a large interface between the monomers. Such a tight interaction could indicate functionality in the dimerization of SeCitS. As no true cooperativity of transport was observed, a functionality regarding the stabilization of the protein or a negative cooperativity could be considered. To gain a better understanding of any potential crosstalk between the monomers within the dimer, variants of the protein aiming at inactivating one monomer were designed. Such an inactivation would lock one monomer in either of the conformations while the transport activity of the other monomer was assessed. This could be achieved by using a double transformation and purification strategy with one monomer (inactivated) being His-Tagged and one functional monomer using a Strep-Tag. By using information from the crystal structure, two residues in close proximity were selected to stop and lock the transporter in one of the two conformation seen in the crystal structure. This was achieved by selecting a lock of an amino acid from the helix bundle to one of the interface domain. This approach was to be used in transport measurements to evaluate the dependence and conformational crosstalk in transport of the two protomers in the dimer.

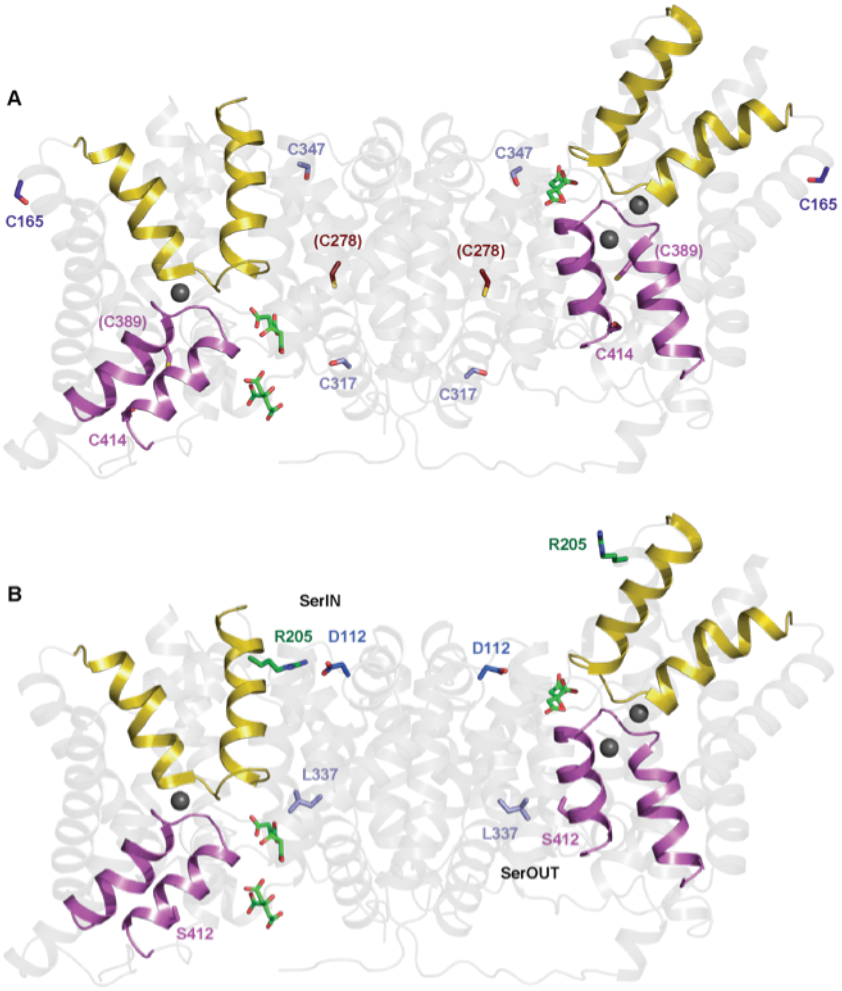

Figure 3.1: Location of mutated residues within the cysteine-cross link-approach. A) sideview of native SeCitS with cysteines highlighted as sticks. Brackets indicate the cysteines that were not mutated to serines. B) For the cross-link of the inward-facing conformation ($SeCitS_{SerIN}$) residues D112 and R205 are highlighted as sticks. L337 and S412 represented as sticks are in close proximity for an outward-facing cross-link ($SeCitS_{SerOUT}$).

The introduction of cysteines for disulfide bridging is a valuable tool in such an approach. SeCitS contains six cysteines (C165, C278, C317, C347, C398, C414, Figure 3.1), with none of them in disulfide bonds under physiological conditions. The first step of the mutagenesis concept was to eliminate native cysteines, which could interfere with any cysteines introduced for the cross-link. The substitution of cysteines C165, C317, C347, and C414 with serines in a protein variant designated $SeCitS_{Ser}$ was to be tested first. The other two cysteines C278 and C398 were not mutated, as their location within the protein was not indicated to interfere with the introduction of new cysteines.

With the $SeCitS_{Ser}$ mutant on hand, selected amino-acids were mutated to cysteines. The positions for the new cross-link sites were determined by the analysis of the crystal

structure. Different pairs of amino acids that showed interaction due to close proximity in the structure were chosen for the inward and the outward conformation to allow a locking of the transporter in either conformation. For the inward conformation, positions D112 and R205 were chosen ($SeCit_{SerIN}$), as they form a salt bridge at the periplasmic surface of the protein. Their Cα distance of 11 Å in the salt bridge increases to 22 Å in the outward-facing conformation. To lock SeCitS in the that conformation ($SeCitS_{SerOUT}$), the selected residues were L337 and S412, which are in close proximity for hydrophobic interactions in the outward conformation at 8 Å Cα distance, but far apart in the inward-facing conformation (23 Å). The newly introduced cross link cysteines could then either be paired with oxidizing agents to form disulfide bonds or by adding mercury to bridge the thiols.

3.1.1 Production of High Amounts of Pure Protein for Analysis

A basis for the structural and functional investigation of a protein is often its preparation in sufficient amounts and at high purity. In order to obtain pure SeCitS for crystallization and functional studies, the protein was heterologously expressed in *E. coli* and the membranes were isolated and solubilized. After affinity chromatography and proteolytic cleavage of the tag, the sample was subjected to a size-exclusion chromatography (Figure 3.2A) to obtain the purified protein. These steps were monitored via SDS-PAGE (Figure 3.2B).

The proteolytic cleavage of the protein from its tag guaranteed a very high purity of the protein, providing optimal conditions for subsequent structural and functional analysis. The yield of the purification procedure was up to 1 mg protein per liter culture volume.

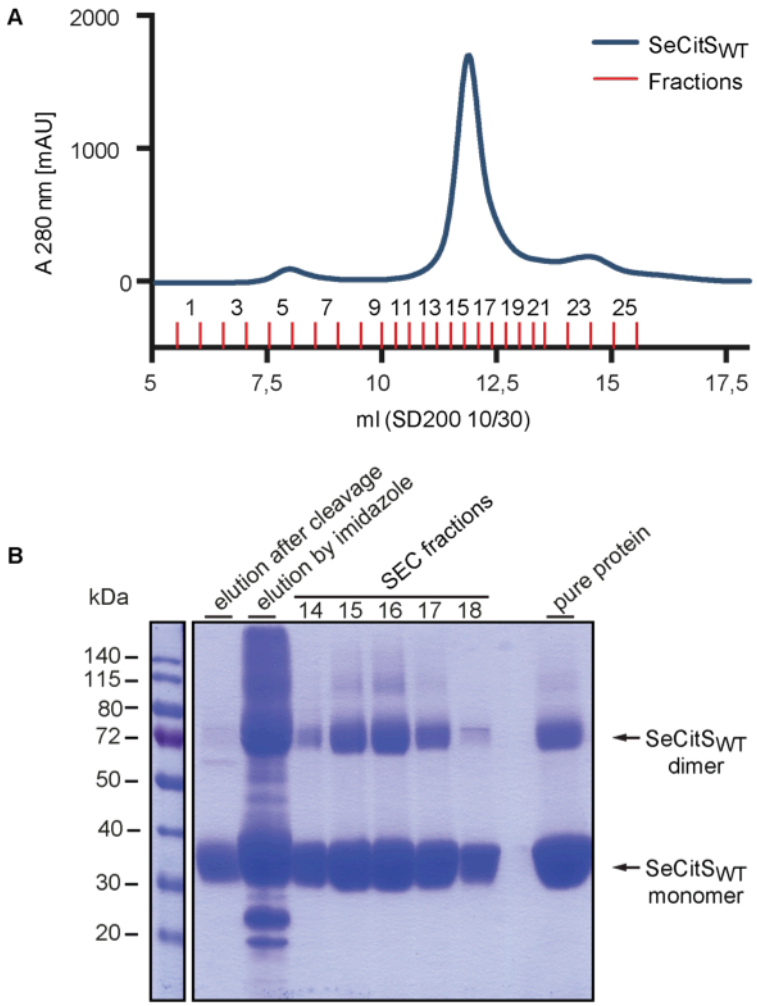

Figure 3.2: SEC elution profile and SDS-PAGE analysis of the SeCitS$_{WT}$ purification. A) The elution profile for the SEC of SeCitS$_{WT}$ after thrombin cleavage off the nickel affinity column showed a monodisperse peak at around 11.6 ml on a Superdex 200 (10/30) column. B) The purification steps (after elution of the cleaved protein, of fractions of the size-exclusion chromatography and of the pooled, concentrated protein) were monitored by SDS-PAGE. The lower band with an apparent molecular weight of 35 kDa represents the monomer, while the upper band of approximately 70 kDa represents the still intact dimer that was not completely denaturated by SDS indicating a strong interaction of the monomers. Additionally, a sample of the residual uncleaved protein on the column eluted by imidazole is shown.

The imidazole eluate from the affinity column after cleavage of SeCitS showed that at least 20% of protein remains on the column. Two bands appear, one at the height of the cleaved SeCitS and one slightly above, which would point to a “heterodimeric” population of one cleaved and one uncleaved monomer in the dimer that remains on the column under normal purification conditions and is only separated during SDS-PAGE.

In addition to the SeCitS$_{WT}$ protein, its variants with serines replacing the cysteines and subsequent mutations were cloned and purified analogous to the wild-type protein. The

base mutant for cross-linking studies ($SeCitS_{Ser}$, Section 3.1.3) with cysteins C165, C317, C347 and C414 mutated to serines were purified at concentrations similar to wild-type SeCitS. As the preparation of protein was always carried out in the same manner, comparisons of the size-exclusion chromatography profiles were a good indicator for the quality of the preparation. After the introduction of cysteines at the designated cross-linking sites, the yield of protein after purification was very low.

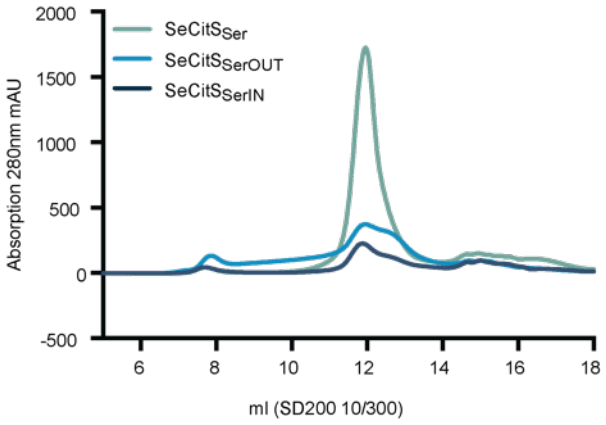

Figure 3.3: Size-exclusion chromatography of cysteine variants of SeCitS. In $SeCitS_{Ser}$, cysteins C165, C317, C347 and C414 were mutated to serines and shows an elution profile comparable to the wild-type protein. Variants with putative cross link pairs introduced ($SeCitS_{SerIN}$ with D112C and R205C and $SeCitS_{SerOUT}$ with L337C and S412C) show a significantly reduced stability under the same preparation conditions.

3.1.2 Reconstitution of SeCitS in liposomes for Transport Studies

For the analysis of membrane transport characteristics, preparation of tight unilamellar liposomes for filter assays was a necessity. Several different techniques for the preparation of vesicles are available. As the preparation of tight liposomes proved to be challenging, an analysis of different preparation procedures was performed. Liposome preparation via freeze-thaw cycles, extrusion and sonication were tested. One tool to evaluate the liposomes was the size determination with Nanoparticle Tracing Analysis to verify the uniformity of vesicles.

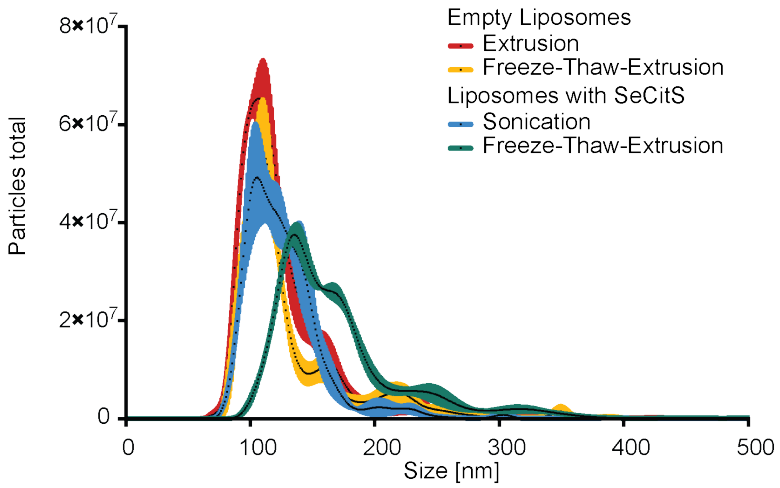

Figure 3.4: Particle size distribution of different liposome preparations. The size of different modes of liposome preparations (freeze-thaw-extrusion, extrusion only and sonification) with and without protein incorporated was evaluated using Nanoparticle Tracing Analysis (NanoSight, Malvern Panalytical).

As extrusion of the lipids was performed with a 400 nm filter, the expected particle size for preparations using extrusion was close to or below that size. Results showed that the average particle size was consistently smaller. The largest particles and the particles with the biggest range in size were obtained by freeze thaw cycles followed by extrusion. The narrowest range in particle size was obtained for the sample that was prepared by extrusion only. This technique was subsequently used in the preparation of proteoliposomes.

Apart from the vesicular dimensions that were assessed, another factor was even more influential. The crucial component in the preparation of good liposomes for the transport assay proved to be the lipids used for the reconstitution. Batches older than 12 months resulted in a significantly reduced stability and high permeability. Extensive testing of different lipid batches was performed by Anne Schieferdecker (Schieferdecker, 2016). The optimal reconstitution protocol established for transport assays with radioactive ^{14}C-citrate is described in Section 2.4.4.

3.1.3 Transport Activity in Mutants for Protomer-dependence

An interdependence of the protomers within the dimer could not be excluded by the lack of a cooperativity in the transport of citrate as previously seen. To assess the suitability of the designed mutations to lock the transporter, the transport activity of the mutants was tested.

The first step of the mutagenesis concept was to eliminate native cysteines, which could interfere with any cysteines introduced for the cross-link replacing them with serines in $SeCitS_{Ser}$. The relative transport activity of the cysteine-to-serine-variant $SeCitS_{Ser}$ was slightly higher than that of $SeCitS_{WT}$ (Figure 3.5), albeit not statistically significant. Subsequent variants for cross-linking contained cysteines reintroduced in positions that showed strong interactions in the native crystal structure: $SeCitS_{SerIN}$ with D112C and R205C for the inward conformation and the pair of L337C and S412C for the outward conformation in $SeCitS_{SerOUT}$. The reintroduction of cysteines in those positions proved to be problematic as they each reduced transport activity by more than 90% compared to the base mutant and the wild-type protein (Figure 3.5).

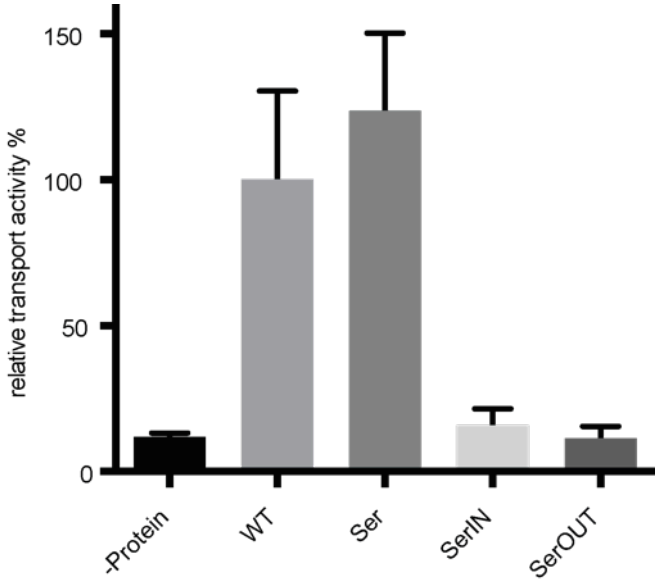

Figure 3.5: Transport activity of mutants for cross-link experiments. The relative transport activity of WT SeCitS was compared with the cysteine-free base mutant ($SeCitS_{Ser}$) and the intended cross-link mutants ($SeCitS_{SerIN}$ and $SeCitS_{SerOUT}$). The liposomes were prepared with reducing agent to prevent the cross-link to cystines. Relative transport activity was at near wild-type level for the base mutant but greatly reduced after the reintroduction of cysteines for the internal cross-links.

The transport activity was routinely normalized to protein content of the liposomes via amido black assay, so a difference in protein concentration did not have an impact on the apparent transport activity.

After obtaining the first promising results that the transport activity was not affected by the introduction of serines to replace cysteines, the subsequent decrease in activity rendered this approach ineffective. As the samples all contained reducing agents in this set of experiments any effects by a bridging of the reintroduced cysteines can be excluded. The main problem was identified in the low stability of the mutants as the purification already proved difficult. The transport activity was always normalized to the amount of protein in the samples, nevertheless it cannot be excluded that, as the protein itself was instable and did not retain its functional form in the membrane, the transport activity was skewed towards even lower rates.

To expand on these results different base mutants and additional transport and cross-link experiments were carried out in conjunction with Anne Schieferdecker and presented in her master thesis (Schieferdecker, 2016). Neither of the tested combinations or options resulted in suitable protein variants to obtain unambiguous results. Consequently, any further investigation regarding the transport codependence could not be performed with this approach.

3.2 Electron Microscopy as Tool to Quantify Dimer States

An important parameter of secondary active transporters is their conformational state in dependence of their environmental conditions such as pH, substrate concentration, lipid composition, or presence of other molecules. However, as the quantification of the tight dimerization and its effects on the conformational states of the monomers within the dimer of SeCitS by functional assays did not succeed, an approach of using cryo-EM to determine the conformational state was chosen. With the advances in the cryo-EM field, significantly impacted through the use of direct detectors, the option of studying smaller proteins opened up. In combination with improved computational capabilities, an evaluation of different conformational states is now within the realm of possibilities. The freezing process for proteins retains the conformational ensemble within the sample. If a sufficient number of particles is selected this representative set allows for a statistical analysis of different states of the protein. This approach of using cryo-EM was taken for the evaluation of statistical distribution of conformations within SeCitS.

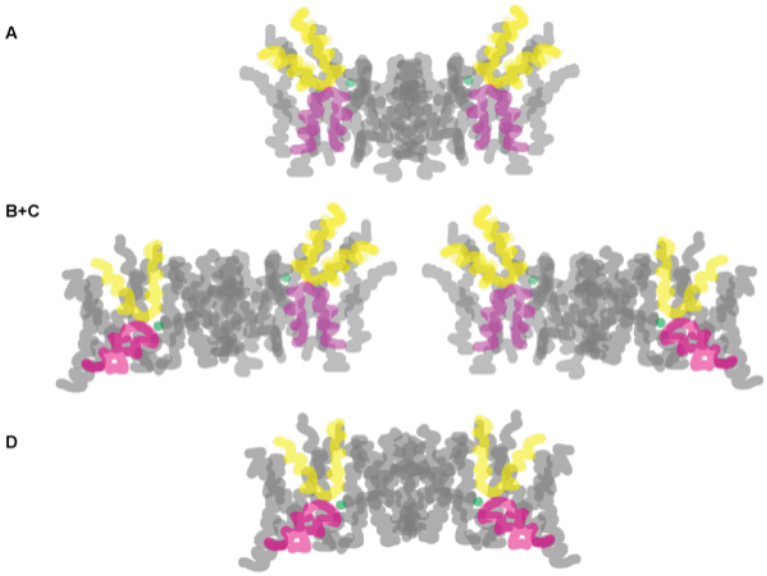

Figure 3.6: Visualization of possible states within the dimer. A and D represent symmetric dimers, either with both protomers outward-facing or inward-facing, while B and C are virtually identical by rotational symmetry within the membrane plane, but are shown in either asymmetric iteration to represent a stochastic distribution of the conformations.

It can be assumed that the most prominent states the protomers can take on are either outward-facing or inward-facing. Transition states are energetically unfavorable and would thus only exist for a short time, consequently making up only a small portion of the state the dimer can be in. If the distribution between inward-facing and outward-facing conformation was stochastic and the protomers within a dimer adopted those conformations completely independently, the following distribution would present itself: half of the dimers would adopt symmetric conformations with a 25% being in the all outward-facing conformation and 25% as all-inward-facing dimers. The other 50% would be present as asymmetric dimers (Figure 3.6).

As the energy levels of the two confirmations are not identical, the distribution between inward-facing and outward-facing is not stochastic. Likewise, a codependence of the two protomers within the dimer could not be ruled out by the previous experiments.
In the crystal structure of the native SeCitS, both dimers within the unit cell assume an asymmetric conformation. In contrast the crystal lattice of the seleno-methionine variant $SeCitS_{SeMet}$ of the citrate transporter used for experimental phasing contained one asymmetric and one symmetric dimer with both protomers facing inwards. Neither of those crystals contained symmetric outward-facing dimers. Within a crystal there it is a highly organized environment, which may itself already force the proteins to adopt a certain

conformation after the initial nucleation. To allow an unbiased and native-like environment, flash-freezing for cryo-EM presented a suitable opportunity to examine those conditions.

3.2.1 SeCitS Sample Preparation and Evaluation using Negative-stain EM

In preparation for the experiments, it was thought to be important to provide the most native-like environment to the protein, to ensure as little interference with the conformational distribution as possible. Lipid environments like nanodiscs and saposin nanoparticles would provide this prerequisite. Even though it is often favorable to cleave the purification tag, in this approach, the uncleaved His-tagged version $SeCitS_{His}$ allowed further purification during the preparation of the lipid particles. For purification, the protein was eluted from the affinity chromatography column with an imidazole buffer, without thrombin cleavage. After dialysis to eliminate the imidazole), a size-exclusion chromatography was performed. $SeCitS_{His}$ had a shorter retention time on the gel filtration column (Figure 3.7). The cleavage site and the His-tag add 2,6 kDa to the protein, which results in an increased hydrodynamic radius of the protein compared to the cleaved protein, especially as tag and cleavage site are not close to the rest of the protein but adds an unfolded tail.

To investigate the protein in a near-native environment, SeCitS was reconstituted into different lipid environments. The two systems used were saposin nanoparticles, which was optimized in the bachelor thesis of Lisa Klatt (Klatt, 2017), and conventional nanodiscs. For the preparation of nanodiscs, $SeCitS_{His}$ was used as it allowed the separation of SeCitS reconstituted in nanodiscs from empty nanodiscs via affinity chromatography (Figure 3.7A). The peak fraction of a size-exclusion chromatography, with highest concentration and homogeneity, was used for EM grids.

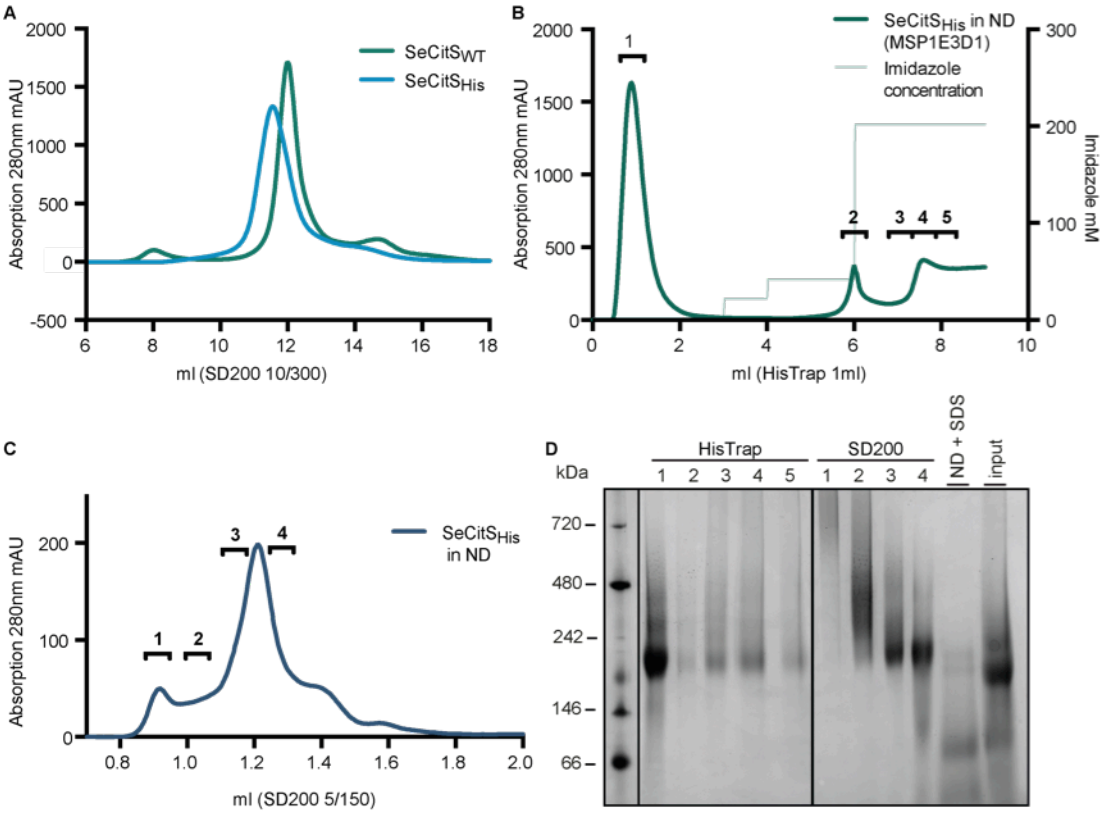

Figure 3.7: Preparation of nanodiscs for EM. A) Chromatogram of SeCitS$_{His}$, that shows a shorter retention time on the column (SD200 10/300) in comparison to the cleaved protein. B) Elution profile of SeCitS$_{His}$-loaded nanodiscs from a HisTrap 1 ml column. Elution was performed with a stepwise imidazole gradient to 200 mM. C) Size-exclusion chromatography profile (SD200 5/150) of pooled fractions 3-5 (B) to obtain uniform Nanodiscs. The peak fraction was used to freeze grids for cryo-EM so adjacent fractions 3 and 4 (C) were used to analyze the sample. D) Blue native page of ND samples collected during preparation, including a sample with added SDS and the Nanodisc reaction mixture.

Negative-stain electron microscopy was used to test if samples of SeCitS in different hydrophobic environments were suitable for high resolution cryo-EM. Samples of the transporter in DM and reconstituted into saposin nanoparticles and nanodiscs were tested.

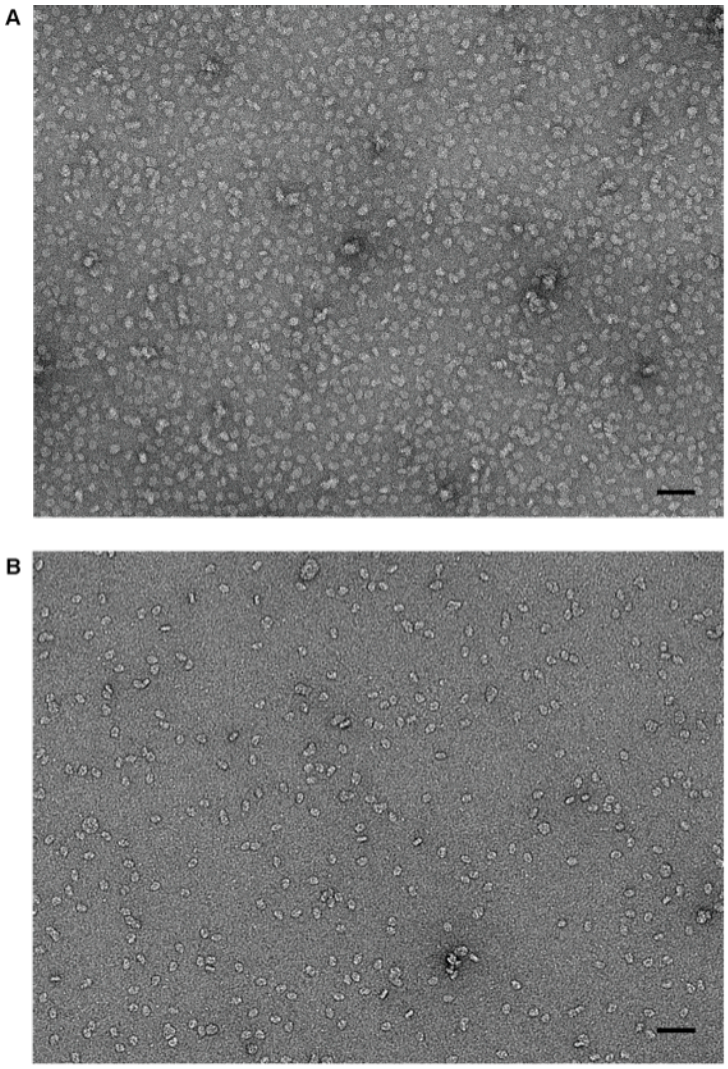

Figure 3.8: Negative-stain images of SeCitS. Uranyl acetate-stained samples of SeCitS in DM (A) and SeCitS in saposin nanoparticles (B). Images were acquired on a Spirit Biotwin 120 keV microscope by Simone Prinz. Scale bars represent a length of 50 nm.

The image of SeCitS in DM shows a high concentration of particles of approximately the expected size of 7-10 nm. Unfortunately, the particle proximity was too high, therefore leading to insufficient separation, which hinders structural analysis in negative-stain-EM. The high concentration also led to increased aggregation of the particles on the grid, as multiple darker areas with protein clusters are visible (Figure 3.8A).

The other sample of SeCitS in saposin nanoparticles had a more even distribution of its particles. The particles do not appear to be as uniformly shaped as in the DM sample, as more elongated, rounded and bigger particles are visible. Aggregation does not seem to be as prevalent as in the samples with DM (Figure 3.8B).

Samples of SeCitS in nanodiscs were also analyzed and show a more even size distribution compared to the other nanoparticle sample with saposin. The particles were evenly distributed over the grid and did not show any clustering due to aggregation.

3.2.2 Cryo-Electron Microscopy of Nanodisc Sample for Statistical Analysis

As the preparation of SeCitS in saposin proved to result in a very low yield and a larger variation in particle size, the acquisition of cryo-EM images was done using SeCitS in nanodiscs. Acquisition of 1500 images was carried out on a Titan Krios equipped with a K2 camera at a magnification of 200 000 and a pixel size of 1.14 Å in a defocus range of -2-3 µm. The particles in the images were well distributed and of homogeneous size. The particle shapes were oval or roughly rectangular.
As a control, a small set of 100 images was collected of a sample of empty nanodiscs to ensure correct attribution of particles to SeCitS.

The images of SeCitS in nanodiscs were processed in cisTEM and 510 000 particles were extracted. A 2D classification was performed. During the processing and classification of 2D stacks, top views of particles with a distinctly different shape than that of SeCitS appeared. Even when only good-looking classes were selected and reclassified, a prominent subset of classes again with particles not matching the top view appeared. Also, in the side views of the particles, two independent subgroups could be identified by eye only. One group showed an even distribution of intensity across the particle. The other one had a dark spot in the center of the molecule indicating a low electron density in this region. This did not correlate to what was expected of side views of the citrate transporter, as it has no large central cavity.

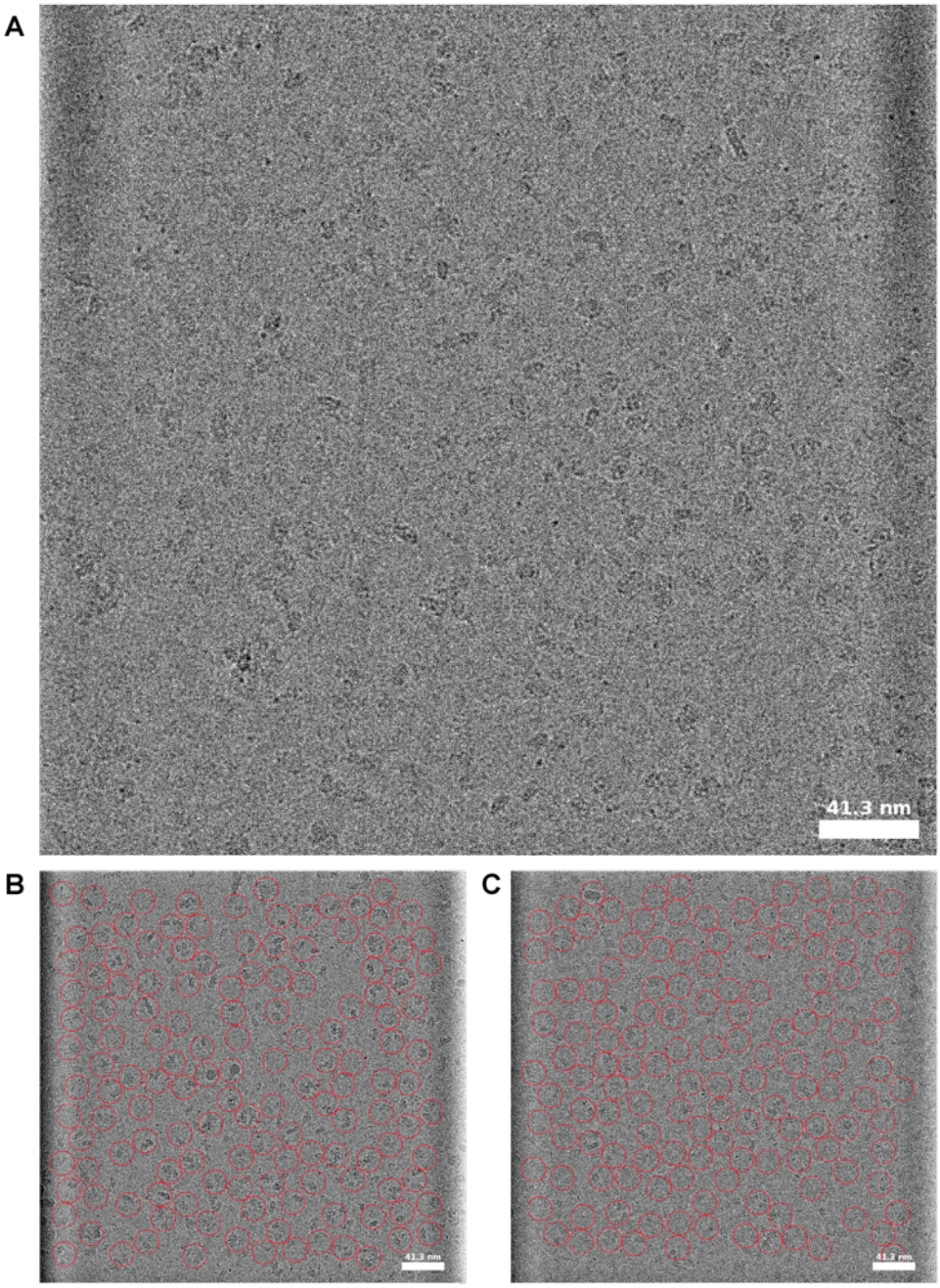

Figure 3.9: Cryo-EM of SeCitS in nanodiscs. Representative cryo-electron microscopy micrographs of SeCitS prepared in nanodiscs (A) with red circles indicating the picked particles (B and C).

The sample used for freezing the grids was analyzed by mass spectrometry (performed by Imke Wüllenweber). In Table 3.1, the results were ranked by the most abundant peptides. Apart from the expected proteins, e.g. SeCitS, MSP (identified as apolipoprotein A) and common contaminations such as keratin and hemoglobin, the most prominent protein was a maltose binding protein MalP of *E. coli*.

Table 3.1: Mass Spectrometry analysis of a sample of SeCitS in nanodiscs. The Results are ranked by relative occurance of matches of peptides. Besides the expected SeCitS and MSP (here identified as Apolipoprotein A-I precursor), the usual contaminations with Keratin can be found as well as a dominant population of MalP (in two isoforms).

Confi-dence	Accession	Description	Protein Name	Cover-age [%]	Pep-tides	Nbr. AAs	MW [kDa]
High	902845795	Maltose phosphorylase [Salmonella enterica]	MalP	31	23	797	90.2
High	554014442	Maltodextrin phosphorylase [Salmonella enterica]	MalP	30	23	797	90.1
High	564511182	Citrate:sodium symporter [Salmonella enterica]	**CitS**	35	18	446	47.6
High	P12763	Alpha-2-HS-glycoprotein precursor [Bos taurus]	BSA	30	8	359	38.4
High	P04264	KRT1 Keratin, type II cytoskeletal 1	Keratin	31	19	644	66
High	P13645	KRT10 Keratin, type I cytoskeletal 10	Keratin	22	14	593	59.5
High	P35527	KRT9 Keratin, type I cytoskeletal 9	Keratin	21	10	623	62.1
High	P05787	KRT8 Keratin, type II cytoskeletal 8	Keratin	26	11	483	53.7
High	P01966	Hemoglobin subunit alpha [Bos taurus]	Hemoglobin	46	4	142	15.2
High	818426190	Glutamine-fructose-6-phosphate aminotransferase [Salmonella enterica]		27	10	609	66.8
High	564497500	Molecular chaperone DnaK [Salmonella enterica]	DnaK	15	10	638	69.2
High	P02769	Bovine serum albumin precursor [Bos taurus]	BSA	20	9	607	69.2
High	1020368955	Transcriptional regulator Crp [Salmonella enterica]		43	9	210	23.6
High	Q3T052	Inter-alpha (Globulin) inhibitor H4 [Bos taurus]		12	8	916	101.4
High	Q04695	KRT17 Keratin, type I cytoskeletal 17	Keratin	22	9	432	48.1
High	P15497	Apolipoprotein A-I precursor [Bos taurus]	**MSP**	22	6	265	30.3
High	660592426	Aerobic glycerol-3-phosphate dehydrogenase [Salmonella enterica]		23	9	507	57.4
High	P15636	Protease I precursor Lysyl endopeptidase Achromobacter lyticus		16	5	653	68.1
High	Q3KNV1	KRT7 keratin 7	Keratin	20	8	469	51.4
High	Q2UVX4	Complement C3 precursor [Bos taurus]		8	7	1662	187.2

The monomer has 90.5 kDa and forms a dimer with a parallelepiped shape of 60 Å by 100 Å and 120 Å. The dimensions of the soluble dimer were comparable to the size of the SeCitS dimer embedded in its lipid environment in the nanodiscs. The low-resolution volume of the intruding protein was reconstructed in 3D and fitted the crystal structure of MalP (pdb: 2ECP) (Figure 3.10D).

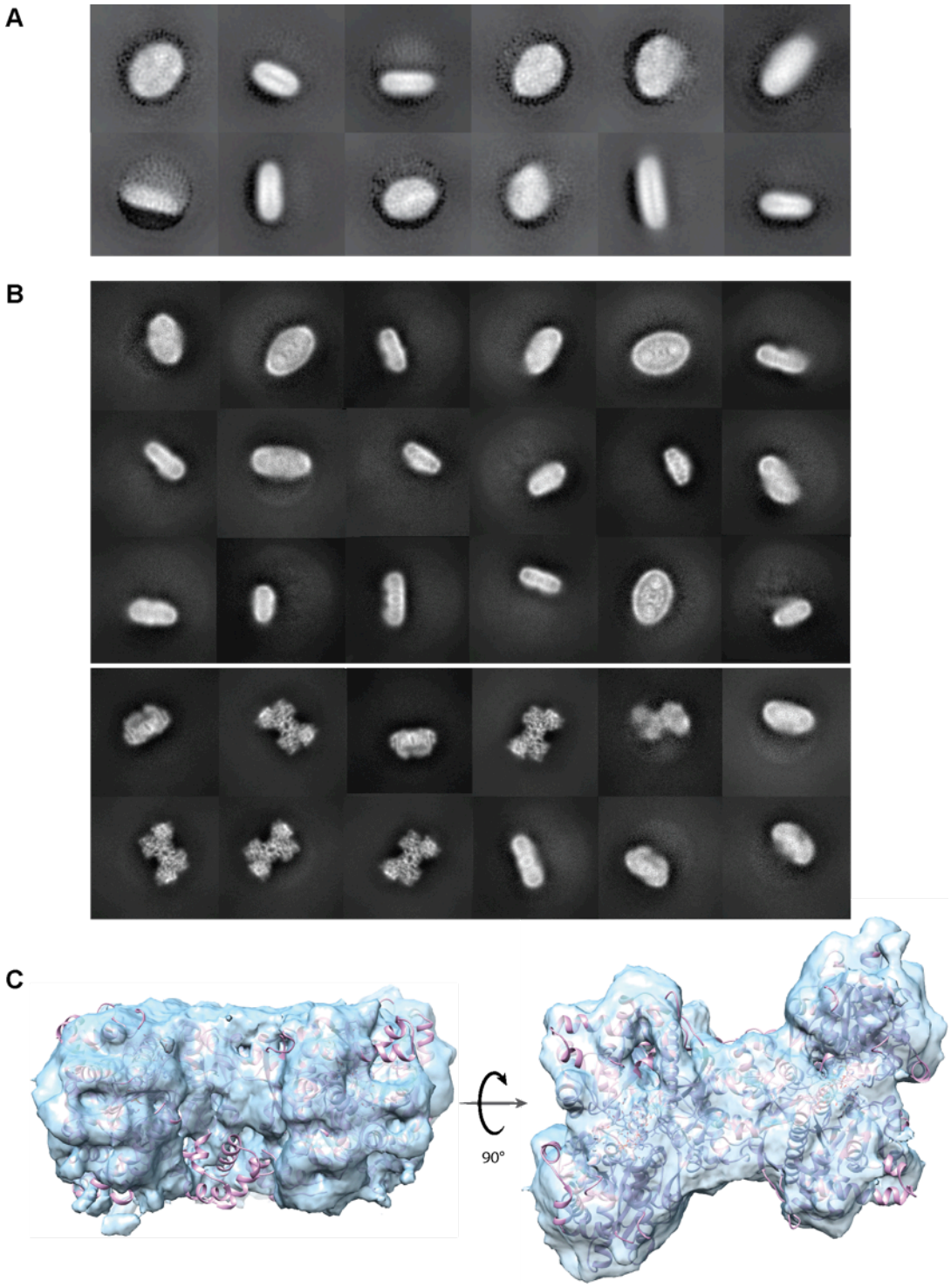

Figure 3.10: 2D classes of cryo-EM samples of nanodiscs without and with SeCitS and a 3D reconstruction of MalP. A) 2D classes of empty nanodiscs. B) A variety of 2D classes of the SeCitS in nanodiscs sample generated from 510 000 particles. The shape and resulting density pattern of SeCitS can be detected in a number of classes, especially in top views. 2D classes that do not fit SeCitS, but resemble MalP are subgrouped in the two lower rows. C) A coarse 3D reconstruction of the 2D classes assigned to MalP (blue) with a fit of the MalP crystal structure (pdb: 2ECP, pink).

The majority of particles were allocated into classes that could be assigned to SeCitS. In those classes, especially in the top views, a distinction of the dimer interface domain and the flanking transport domains was already possible (Figure 3.10B). But as the side view of MalP and SeCitS were indistinguishable in 2D classes it was not possible to eliminate the contaminating particles computationally. It was thus not possible to obtain a 3D reconstruction of SeCitS from this sample and dataset. The general quality of the data is sufficient to identify the protein and desired classes. A different sample preparation strategy, avoiding the affinity chromatography, which lead to the adverse concentration of MalP in the sample, was devised but could not be tested within the scope of this thesis. Under improved conditions an assessment of SeCitS using cryo-EM should be feasible. The project is being continued by Saskia Mehlmann and shows first promising results.

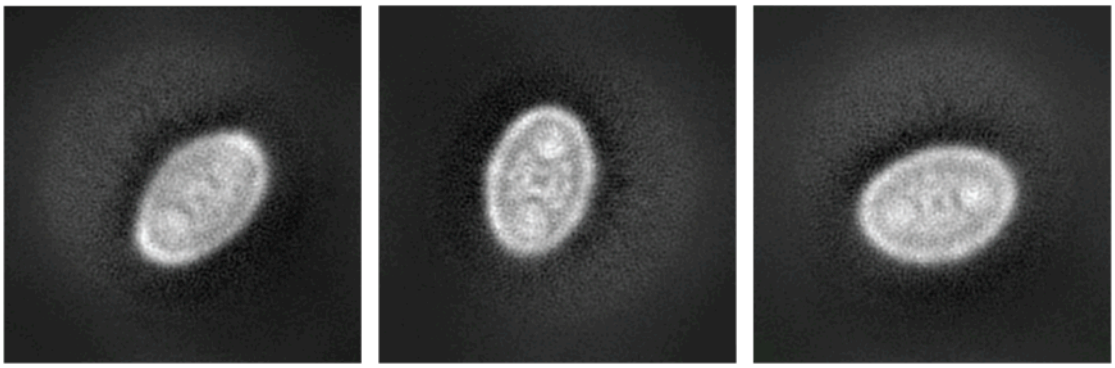

Figure 3.11: Selected 2D top-view classes of SeCitS. The three best classes of top-views already allow a distinction between the interface domain and the transport domain.

Using cryo-EM to elucidate the basic structure of proteins and protein complexes is only one part of the versatility of this technique. Flash-freezing protein conserves the structural multitude of conformations within the protein mixture. If substates of the protein can be computationally distinguished, it is possible to snapshot the conformational variance of the protein. We wanted to use this technique to evaluate the natural distribution between the different conformational states of the transporter. Prerequisite for this investigation was to obtain a suitable sample of SeCitS. A native-like lipid environment was provided by the nanodiscs to allow an unbiased distribution. In the first trials, the comparison of 2D classes of SeCitS in nanodiscs and with empty nanodiscs revealed that the protein was clearly visible. The features of the transporter that derive from the crystal structure were distinctly recognizable in the comparison of the 2D classes. The helix bundle was identified by the interface domain.

Although the 2D classification of particles provided the first look at top views, a number of particle classes emerged that could not be assigned to SeCitS, but were identified to be MalP. The soluble protein MalP was previously also identified as a minor contaminant in a sample of purified SeCitS in DM as detergent (Schieferdecker, 2016). The huge abundance of MalP in the Nanodisc sample can only stem from the preparation of the SeCitS nanodiscs. A probable cause is the nickel affinity chromatography separating the empty nanodiscs from SeCitS loaded nanodiscs. During this step, an enrichment of MalP probably occurred as it is a soluble protein, thus not reliant on detergents or lipids, and displays some histidines on its surface, that would allow for chelation. Meanwhile, a substantial amount of SeCitS was lost to aggregation as not all detergent was efficiently replaced by the hydrophobic environment of the nanodiscs.

As the contamination with MalP was too prominent and could not be excluded by skillfull classification, for further such attempts, an improved purification strategy will be required to provide samples that allow the determination of the main distribution of conformations in solution. SeCitS would then add itself to the ever-increasing list of small membrane proteins that are structurally assessable to cryo-EM. The advances that this technique experienced within the last decade make it a powerful tool in answering complex biological and structural questions.

3.3 Functional Analysis of Substrate Selectivity

The main functional characteristics of a transporter are the binding and transport of its substrates. In previous experiments, transport activity of SeCitS at different substrate concentrations and pH values has been tested (Grötzinger, 2014). To expand our knowledge, the transport properties of SeCitS, especially towards alternative substrates besides sodium and citrate, were tested. As understanding binding is a part in the puzzle that is the transport cycle of the protein, quantifying the substrate binding to the transporter through thermodynamic parameters was a central aspect of the experiments conducted.

3.3.1 *Influence of Ions and other Substrates on Transport Activity*

To test the activity of SeCitS, radioactively labelled citrate was used as a reporter to detect the transport of citrate into the proteoliposomes. The setup includes the protein with no substrate reconstituted into unilamellar vesicles being diluted into reaction buffer containing the radioactive citrate and additional components. First, the ability of different ion gradients to energize transport was tested in the transport assays. The vesicles with SeCitS were prepared with choline chloride as a non-transportable ion. The tested ions for the outside reaction buffer were sodium, potassium and lithium with choline as a control. The results show that only sodium can drive transport of citrate. Neither lithium nor potassium were able to achieve transport activities above background level (Figure 3.12A).

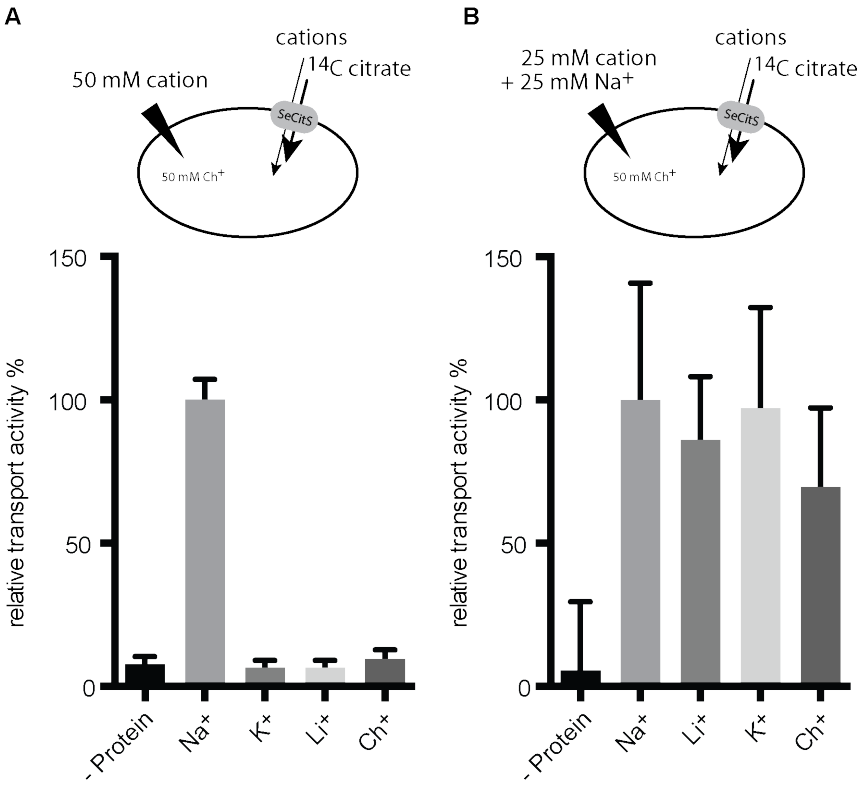

Figure 3.12: Influence of ions on citrate uptake by SeCitS. A) Dependence of citrate uptake in the presence of cations. SeCitS-mediated uptake of ^{14}C-citrate into proteoliposomes was measured in the presence of Na^+, Li^+, K^+ or choline (Ch^+) ions at 50 mM. B) Competition of sodium-dependent uptake by other ions. SeCitS-mediated uptake of ^{14}C-citrate into proteoliposomes was measured in the presence of Na^+ ions at 25 mM. The effect of presence of additional ions (Li^+, K^+ and choline) when added at 25 mM was recorded. Normalization was based on sodium-dependent transport. Error bars show standard deviation.

In addition, the competition of other ions in the presence of sodium ions was measured with the reaction buffer containing 25 mM sodium and 25 mM of an additional ion. The results show only a slight reduction in activity in the presence of lithium and choline, whereas the activity in the presence of potassium remains unchanged. The competitor with the highest efficiency (approximately 40% reduction versus control) was choline. In other experiments, this cation is used to replace sodium in buffers, as the comparably large size does not allow its transport by SeCitS (Figure 3.12B).

In order to analyze the impact of different, structurally related compounds on the transporter, a competition assay was performed. A 1000-fold excess of unlabeled citrate led to a complete inhibition of ^{14}C-citrate uptake, as only the more abundant non-radioactive ^{12}C-citrate was transported. Similarly, isocitrate and malate were able to block transport. α-Ketoglutarate showed an inhibition of 50%. In contrast, the effects of succinate, glutarate, and tricarballate were marginal. As expected, the uptake of ^{14}C-citrate in the absence of SeCitS in the proteoliposomes was negligible at the level of measurement certainty.

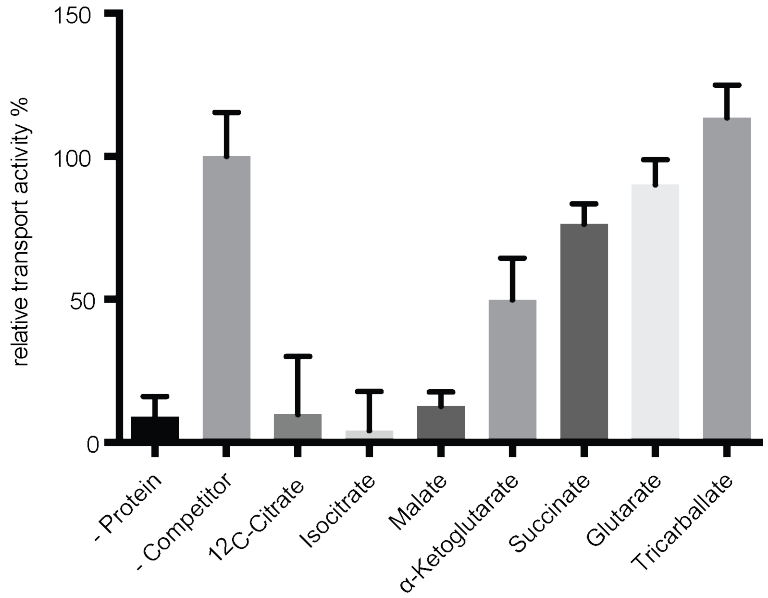

Figure 3.13: Influence of substrate competition on citrate uptake by SeCitS. SeCitS-mediated uptake of ^{14}C-citrate (5 µM) into proteoliposomes was measured in the presence of a 1000-fold excess of structurally similar compounds. In addition, a sample without SeCitS protein and a sample with a 1000-fold excess of natural citrate (^{12}C-citrate) were analyzed. Transport activity in the absence of any compound was set to 100%. Error bars show standard deviation.

Determining the transport properties is one of the main objectives when working with a membrane transporter. Depending on the substrates and the mode of transport, very different setups can be used to study the transport. SeCitS, as a symporter with its two substrates citrate and sodium, demanded an assay with radioactive citrate, as, due to the small size of citrate, ability to act as a buffer and general abundance, other systems with coupled dyes or reporter-dependent assays were not an option.

Transport experiments on the ion specificity showed again the high selectivity of the transporter towards sodium as the driving force in the transport. In contrast to other transporters that coordinate and transport sodium, lithium is not observed to compete with sodium (Wöhlert *et al.*, 2014). In a highly structured binding environment as is provided by the protein structure, competition is only possible for ions of similar hydrodynamic radius. Consequently, the potassium ions were not able to bind at either of the ion binding sites due to the different size. Interestingly, choline showed the highest competition and thus reduction in transport activity compared to the other tested ions. This cation is often used instead of sodium in transport experiments as it is unable to be transported due to its larger size, but overall mimics sodium as a relatively compact mono-ionic cation. Although it may not be transported, choline still proved to be able to occupy the ion binding site and thus inhibit the transport by sodium ions.

In the transport competition assay, only citrate, the structurally similar and similarly-sized isocitrate and malate were able to inhibit uptake of ^{14}C-citrate into liposomes reconstituted with SeCitS. Other potential dicarboxylic substrates like succinate, with a shorter carbon backbone, or glutarates did not compete with citrate. Propane-1,2,3-tricarboxylic acid is fully ionized under neutral pH conditions (pK1: 3.49; pK2: 4.58; pK3: 5.83). Most likely due to these three ionic functions in this molecule, tricarballate, although only lacking the hydroxyl group compared to citrate, was unable to compete with citrate transport. Those results show that not only the chemical structure of the substrate itself but also the ionization state of the substrate is a significant factor in the binding and transport of substrate to the citrate transporter.

In contrast to those findings that emphasise the high specificity of SeCitS, other related citrate transporters, which primarily function as exchangers, demonstrate higher substrate promiscuity e.g. during citrate-glucose co-metabolism for citrate versus lactate. In CitP of *Lactococcus lactis*, a wide variety of mono- and dicarboxylates has been demonstrated to be transport-competent (Pudlik & Lolkema, 2012).

It is important to note that this kind of experiment as conducted here only indicates an inhibition of citrate transport. This inhibition indicates that there is a binding event of the alternative substrate that then blocks transport of the main substrate citrate. Assessing the two modes of inhibition in this context for SeCitS it is clear that although an allosteric inhibition is theoretically possible, it is very unlikely, as there is limited accessibility because the protein is embedded in the membrane. A competitive inhibition at the citrate binding site does not equate a transport of the competitive substrate.

3.3.2 *Calorimetrically determined Thermodynamic Parameters of Citrate Binding to $SeCitS_{WT}$*

ITC measurements can be employed to gain information on the energetics of molecular interactions at constant temperatures. The heat dissipated or absorbed by a binding event can be recorded. Analysis of this concentration-dependent binding allows the distinction of enthalpic and entropic contributions of the energy change in the system. The results also include the dissociation constant of the observed binding. A prerequisite for proper measurements is the reduction of heating effects caused by dilution and stirring of the solutions.

As SeCitS was able to retain some bound citrate during the routine purification, additional purification steps, e.g. exclusion of citrate in all buffers after solubilization and dialysis against citrate-free buffer, were included to ensure consistent measuring conditions with no citrate remaining in the protein as well as a well-defined buffer composition. Samples prepared with citrate in the last purification step were subjected to an additional run over a size-exclusion column with citrate-free buffer. To ensure minimal dilution heat in the reference titration, buffer prepared in the same batch as the dialysis buffer was used for the preparation of the injectant.

A representative titration of wild-type SeCitS is shown in Figure 3.14. The protein concentration was routinely set between 20 µM and 50 µM (Figure 3.14: 22.7 µM) with the citrate concentration in the injectant at 0.5 mM. As a control, a reference titration to measure the dilution heat prefaced every titration (Figure 3.14A). Only with a low heat change, the titration with protein was carried out. Raw data show the heat change of the system with the spikes indicating each injection of ligand.

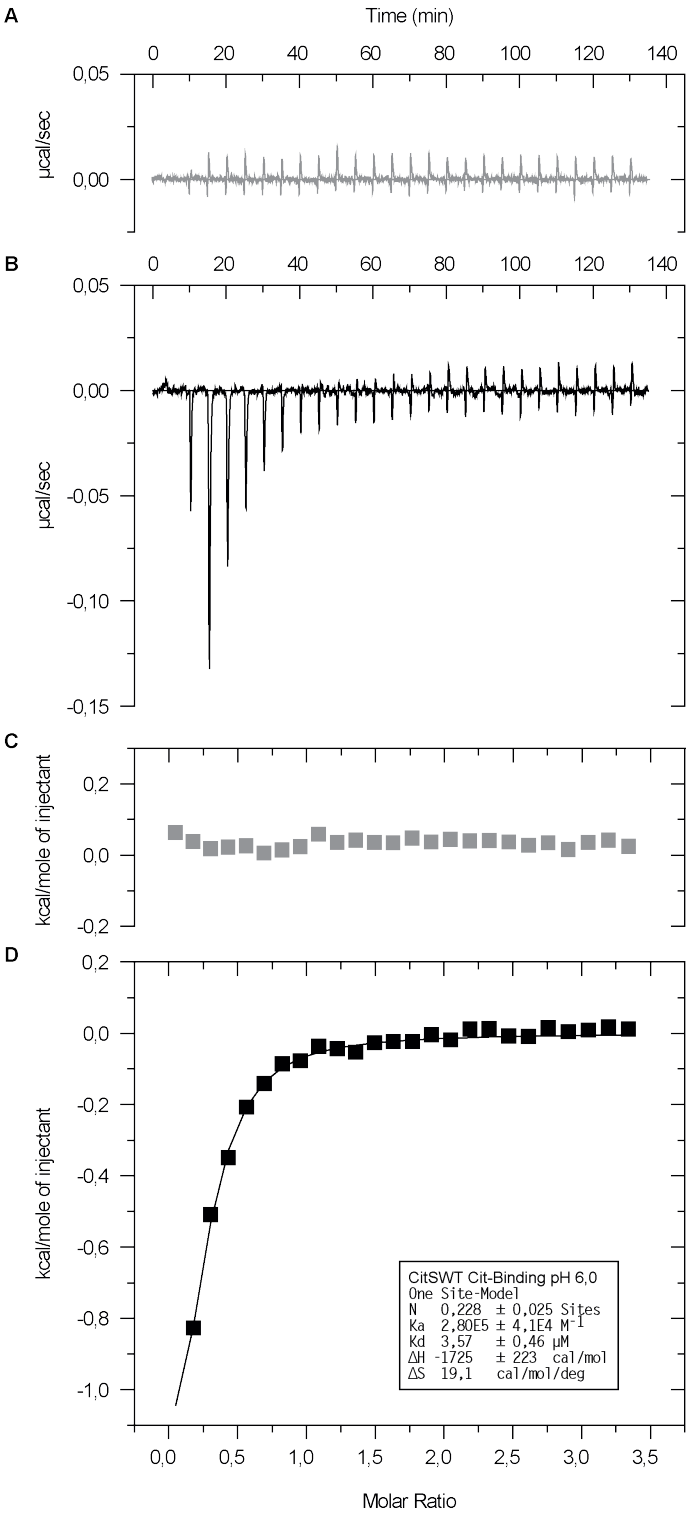

Figure 3.14: Citrate titration with reference titration. A) Dilution heat was measured in a reference titration of citrate injectant to protein buffer. B) SeCitS at 22.7 µM (monomer) was titrated with 0.5 mM citrate. The raw data shows a heat change for every injection that decreases in intensity as the titration progresses. C) Integrated heat of the reference titration with no significant overall change. D) The integrated heat adjusted to the molar ratio of protein and ligand is shown as squares. A fit curve using a one-site binding model (Origin 7 for MicroCal-Systems) was added with its resulting parameters displayed in the inset box.

The results of the citrate-to-protein titration show an exothermic binding event that rapidly converges to zero (Figure 3.14D). The results show a low change in energy in the system, as the measured single changes are only ~1 kcal/mol of citrate at the beginning of the titration. The ideal titration curve for evaluation would be of sigmoidal shape with multiple signals along the sloped part. Adjustment of the concentrations of ligand and protein relative to one another and in absolute numbers would allow for the curve progression to be adjusted. The ideal curve could also be obtained if the affinity were higher. However, the system here with SeCitS and citrate as the ligand could not be optimized to that ideal curve. This also proved to be a challenging factor during the evaluation process of the measurements. As it was determined previously that a single high-affinity binding site is present per monomer, a one-site binding model was used. The resulting fit curve is shown as a line (Figure 3.14D). The parameter values were calculated within the fit function and are listed in the box inset.

The first parameter resulting from this analysis is the Hill coefficient N, which represents the number of binding sites for the ligand on the protein. In all titrations of SeCitS, the Hill coefficient is consistently below 1 and in most cases around or even below 0.5. Here, N is at 0.228 indicating a low stoichiometry of ligand to protein. To ensure that the reason for this low apparent stoichiometry was not an imprecise determination of protein concentration, the protein samples were routinely analyzed using the BCA assay. To validate the concentration one sample was also analyzed via amino acid analysis performed by Dr. Peter Hunziker (University/ETH Zurich, Functional Genomics Center Zurich). The results were within a 6% error of the concentration measured by BCA, which in turn confirmed the molar ratio and thus the Hill coefficient of the measurement. Other fit parameters are the affinities, with the K_D being the inverse of K_A. The affinity was determined to be in the micromolar range (3.57 µM). Repeated titrations resulted in very similar measurements. The titration analysis also revealed that the process of citrate binding to the protein is an exergonic and exothermic reaction. The binding is favored by the contributions of negative enthalpy and positive entropy. The measured change in enthalpy ΔH was at -1.725 kcal/mol. The temperature-dependent entropy ΔS change was determined to be 19.1 cal/(mol K).

ITC was used to determine thermodynamic parameters as a means to study the binding of citrate. The main challenge was the relatively low signal-to-reference ratio. In a lot of cases a strategy used to overcome this problem in other ITC experiments is to increase the concentration of protein in the cell. This approach was tested, but the amount of protein needed and the high increase in concentration proved to create secondary problems. The

limitation in the work presented here was the concentration of protein. The maximum concentration used in the experiments was 72 µM. Trying to increasing the protein concentration via concentration centrifugation was subsequently also paralleled by an uneven concentrating of the detergent which led to a slight destabilization of the protein. Thus, the measurements had to be carried out in less-than-ideal conditions, leading to not completely unambiguous results.

The strategic approach to obtain optimal sigmoidal titration curves is the preevaluation using the c-value as reference. The c-value is the reciprocal of concentration of the receptor and the expected affinity given by the dissociation constant (Wiseman *et al.*, 1989). The value should ideally be in the range of 5 - 100 for an optimal retrieval of plateaus and data points on the slope of the curve. Smaller c-values result in shallow curves that may not even be suitable for evaluation to discern no binding from low affinity binding. On the other hand very high c-values lead to a sudden transition from plateau to plateau which results in a lack of data points during transition so determining the affinity derived from the width of the transition and the stoichiometry based on the inflection point of the curve (Rajarathnam & Rösgen, 2014). Leveraging the affinity measured for transport at 4 µM a c-value of a relatively ideal 50 would only be achievable with a protein concentration of 200 µM. Such high concentrations were not in the realm of experimental possibilities as described above.

The binding affinity of the citrate to the protein measured in ITC titrations correlates very well with the affinity measured in transport experiments. The ITC-measured K_D is 3.57 µM and thus in the same order of magnitude as the value measured in transport with a K_M of 4.1 µM. This is in good correspondence with the K_D of the well-studied prototype transporter of this family *Klebsiella pneumoniae* CitS, which shows an affinity of 10 µM at a pH range between 5.5 and 6.5 (Sobczak & Lolkema, 2005*a*).

The K_D as dissociation constant as a thermodynamic parameter is the true affinity of ligand binding to a protein as opposed to the Michaelis constant as a kinetic parameter. So under usual conditions the K_D represents the ligand concentration at which half of the protein molecules have ligand bound, whereas the K_M gives the substrate concentration at which half of the maximum enzymatic reaction rate is attained. This value is thus not only determined by the substrates binding affinity, but also by how quickly the enzyme-substrate complex is turned over into product. Following the definitions of K_D and K_M one can deduct that for conventional enzyme-ligand system ($E+S \rightleftarrows ES \rightarrow E + P$) with a k_{off} significantly larger than k_{cat} that the K_D equals the K_M. This approximation is only true if the system assumes a

rapid equilibrium. If k_{cat} is not significantly slower than k_{off}, the K_M will be larger than the K_D (Canela *et al.*, 2019). Those theoretical calculations do not completely translate for transporter systems as for example the substrate is removed from the system, though not by a chemical reaction. Also the experimental settings need to be considered here. Although the attempt to maintain generally comparable conditions concerning buffer and salts was made, the ITC measurements are conducted with detergent embedded SeCitS whereas transport assays are performed with proteoliposomes.

3.3.3 pH-Dependency of Citrate Binding

In previous experiments it has been shown that stability and transport activity of SeCitS were influenced by pH, with highest activity and least aggregation around pH 7 (Grötzinger, 2014). This pH-dependence of activity also needs to be considered in the context of changing availability of the substrate, as citrate was shown to be transported as the monohydro-dianionic species. As the highest pKs value of citrate is 6.4, the relative concentration of citrate in the different protonation states changes around physiological pH value. To learn more about citrate binding, titrations of citrate against SeCitS at different pH values were performed (Figure 3.15).

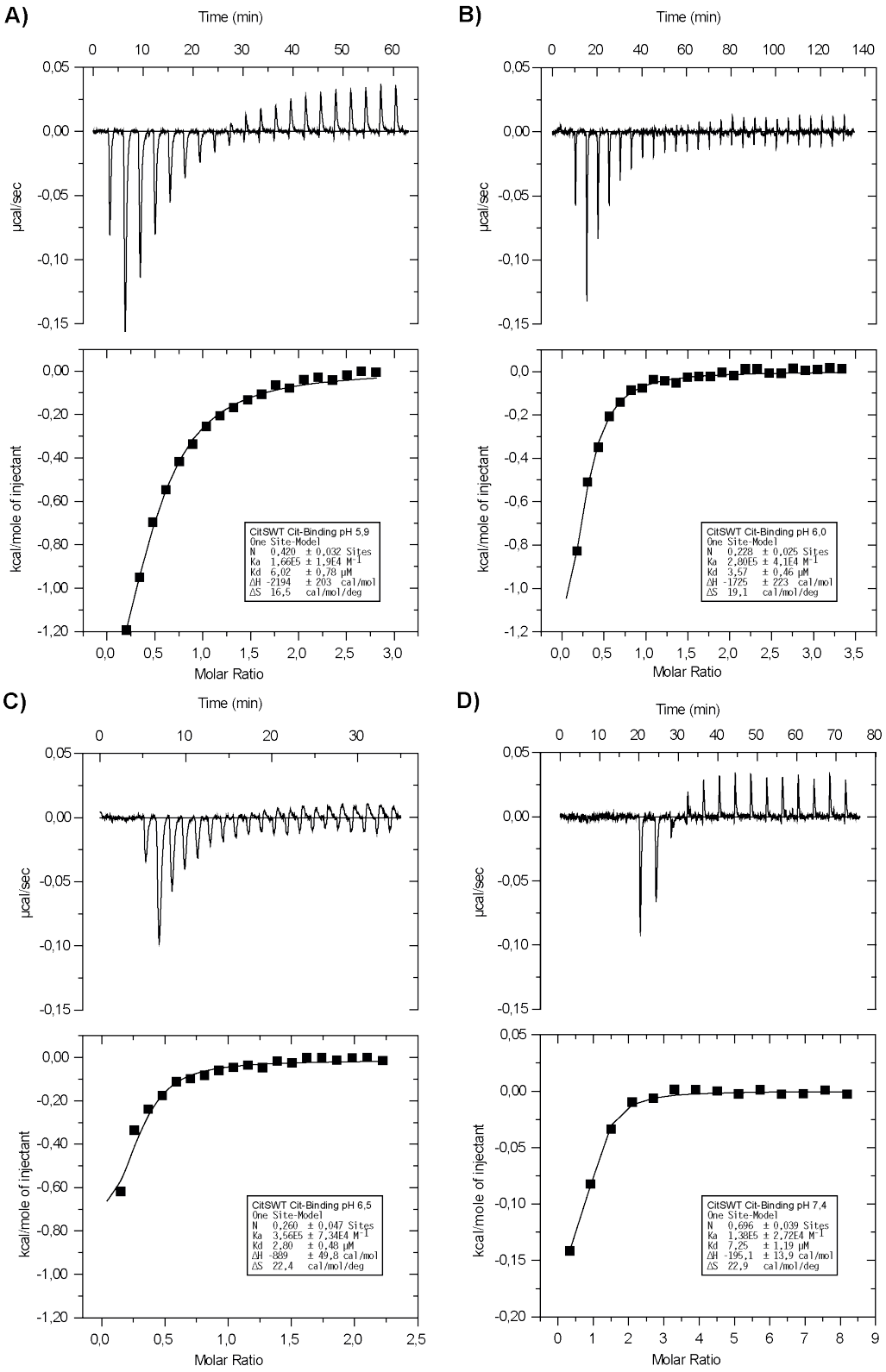

Figure 3.15: Citrate titrations at different pH between pH 5.9 and 7.4. The titrations for pH 5.9 (A), pH 6.0 (B), pH 6.5 (C) and pH 7.4 (D) are shown (upper plots: raw data, lower plots: integrated data). The curves all indicate a similar binding pattern. The curves were fitted with a one-site binding model; the parameters of each titration are listed in the box insets. For better comparability, the scaling was kept constant for all data in A) - C).

The data shown were recorded at pH 5.9, pH 6.0, pH 6.5 and pH 7.4. The general pattern of citrate binding at different pH values was found to be very similar. The binding shows initial exothermic binding. As more citrate is titrated to the protein and full saturation of the protein is achieved, the binding events evoke smaller exothermic reactions that then plateau.

The comparison of citrate measurements at different pH (Table 3.2) reveals that the effective binding affinity of citrate to SeCitS does not change over a pH range of the 1.5 units investigated. The K_D value was approximately 5 µM with a standard deviation of 2.1 µM and was thus consistent over the measured range of pH. In contrast, the enthalpic contribution in the binding decreases greatly from lower (pH 5.9) to higher (pH 7.4) values. The change in ΔH was of one order of magnitude from -2.2 kcal/mol to -0.2 kcal/mol. Subsequently there was also a change in the entropic contribution of the binding. The ΔS increases accordingly over the measured range of pH. The other parameter of the titrations was the Hill coefficient quantifying the binding stoichiometry. The value did not allow an estimation of a trend of pH-dependence. The values ranged from 0.7 to 0.23, again indicating a low stoichiometry of citrate to the monomer.

Table 3.2: pH-dependence of citrate binding parameters. Thermodynamic parameters obtained in different ITC measurements of citrate to SeCitS were compared by pH value.

pH	**N** (Hill)	**K_D** (µM)	**ΔH** (cal/mol)	**ΔS** (cal/(mol*K))	**Buffer substance**
5.9	0.420	6.02 ± 0.78	-2194 ± 203	16.5	MES
6.0	0.228	3.57 ± 0.46	-1725 ± 223	19.1	MES
6.5	0.260	2.81 ± 0.48	-889 ± 50	22.4	BisTris
7.4	0.696	7.25 ± 1.19	-195 ± 14	22.9	HEPES
post isocitrate titration					
5.9	0.499	9.26 ± 1.10	-1910 ± 671	16.6	MES
post sodium titration					
6.5	0.233	6.41 ± 1.26	-1143 ± 209	19.9	BisTris

The table also includes two additional parameter sets. The first one was obtained in a titration of citrate to a sample that was previously titrated with isocitrate (see Section 3.3.5). Similarly, the second set was obtained from a sample, which was previously titrated with sodium (see Section 3.3.4). The measurement conditions were thus slightly different, so the results are presented separately. Nevertheless, the results of both titrations are in line with observations made for citrate-only titrations. The affinity for citrate after the isocitrate measurement is slightly lower than other titrations, but still within the same order of magnitude. Similarly, the change in enthalpy measured for the citrate titration following the sodium titration is slightly higher than the parameter obtained at the same pH value in the citrate titration.

It is remarkable that over a pH range of 1.5 units the affinity of the transporter stays in a very narrow margin within its order of magnitude. From a physiological standpoint it can be advantageous for the bacterial cell to maintain the binding affinity to a nutrient as to be versatile in terms of less than ideal growth conditions and changing environments.
The consistency of affinity over a larger pH range can only happen if the system did not experience any impact of the pH change, or as seen in this case there is a compensation between the changes in enthalpy and entropy. The change in enthalpy is most significant at a lower pH. It can be assumed that a substantial contribution for the enthalpic component originates from the formation of ionic and hydrogen bonds from citrate to protein. Previous results show that citrate is transported by the protein as its mono-hydrogenated species. It can be assumed that the preferred protonation state for binding correlates to that and is also the single protonated citrate. The relevant pKs is 6.4 so at the lowest tested pH values the proportion of monohydro-citrate is larger than at higher pH values. The high availability of the right protonation state allows a direct binding of the substrate to the protein. Higher pH values require the additional protonation of the citrate molecule, which is energetically less favorable and leads to a reduction in free enthalpy gain during the binding event. This protonation of citrate and its subsequent formation of ionic and hydrogen bonds present the biggest contributors to the change in enthalpy. Solely based on this information one could assume that a change in pH to higher values would lead to a reduction in affinity between citrate and the transporter. But the results show that an enthalpy – entropy compensation takes place and renders the change in affinity relatively small. This phenomenon of compensation is well known for systems of proteins with different but similar ligands or other small permutations in the protein-ligand system (Fox *et al.*, 2018). In the end, this results in a thermodynamic trade-off between a tighter binding – an

enthalpically favorable state – and the resulting conformational constraints – entropically unfavorable. Correlated with crystallographic B factors in conjunction with ITC data it was shown that the entropic penalty inflicted could be attributed to conformational restrictions within the hydrogen bonds of the protein-ligand complex (Lafont *et al.*, 2007). A similar phenomenon may happen in the case of SeCitS where the transport rate is pH-dependent with a maximum transport rate between pH 6-7, but the pH has a lesser effect on the binding affinity.

An interesting observation is that the Hill coefficient (N) representing the relative number of binding sites is consistently low in all titrations (see Table 3.2-Column N (Hill)). The number details the amount of citrate molecules bound to the transporter made up of the two monomers. This means Hill coefficients below 0.5 indicate that only one citrate molecule is bound to a dimer. One has to bear in mind that the Hill coefficient is the parameter in the analysis of the titration that most depends on the completeness of the titration curve and thus may experience the highest uncertainty as the titrations lack an initial baseline phase as part of their sigmoidal curve. Nevertheless the data clearly indicate that the stoichiometry is not higher than one citrate per dimer. This is an interesting observation as the transport experiments (Section 1.6.1) showed no cooperativity with respect to citrate. This lack of cooperativity includes positive and negative cooperativity, whereas a Hill coefficient unequal to 1 represents either. This can for example mean that the transport is completely independent in both protomers. In the context of the binding results by ITC here it is more plausible that the second binding site in the second protomer may not be available for binding. The reason for this would be an asymmetric configuration of the protomers in the dimer. Here one of the protomers would be inaccessible as the citrate binding site is buried between the domains of the transporter in its inward-facing conformation.

3.3.4 Investigation of Sodium Binding

As information on the citrate binding parameters was gathered, the question arose if collecting a similar set of data for the second type of substrate of the transporter, the sodium ions, would be possible. ITC can be used to measure the binding of a wide range of binding partners. Yet, as the prerequisite of an effective titration is the absence of the target substrate it requires a different level of preparation. Hence, a system to measure the

binding of sodium ions to the protein was developed. Due to the abundance of sodium in almost all commonly available chemicals, the preparation of samples for those measurements with sodium in the injection syringe proved to be challenging. Several optimization steps were required to identify the right strategy for freeing the protein solution of residual sodium ions and adjusting the buffer conditions to reduce the dilution heat. After pretests, the optimal conditions used for the experiments were found to be 90 mM CsCl as main salt in the protein solution and 90 mM NaCl in the injectant solution. The dilution heat of this setup never exceeded 0.025 µcal/s. The concentration of sodium in all buffers was determined with the help of atomic absorption spectroscopy. The measurements ensured that no buffer contained more than 1 µM sodium ions.

The first set of experiments was a sodium and citrate-free protein solution with sodium as injectant. All measurements of sodium binding to SeCitS were low in overall signal intensity. The intensity of the injections of the titrations were above the range of signals of the reference titrations, indicating that the contribution was indeed due to binding and not only the dilution heat of mixing of the different salts. The titration curve shows a biphasic binding with an initial endothermic and subsequent exothermic component. Based on the present structural data, a 2:1 ratio of sodium ions to monomers in the SeCitS dimer was assumed and a sequential binding model applied to the titration analysis in MicroCal. As the endpoints of the titrations were not well defined, as in a full saturation, the analysis could not give unambiguous values, especially for the determination of the first binding component. The latter few of the titrations all show a significant negative ΔH that represents the exothermic binding.

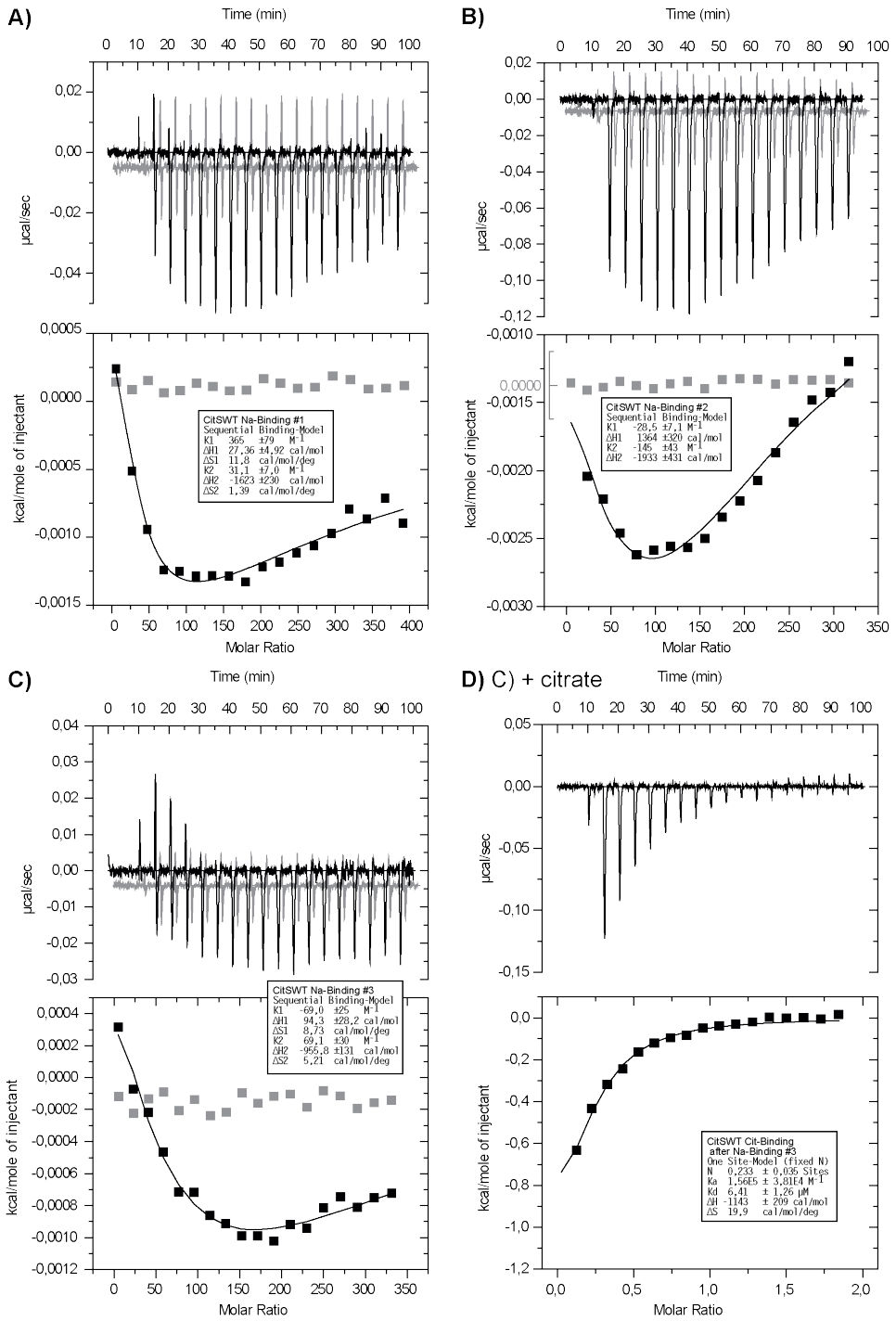

Figure 3.16: ITC titrations of SeCitS with sodium as injectant. Sodium-free protein in 90 mM CsCl buffer was titrated with 90 mM sodium. The experiment was repeated thrice with different protein concentrations (A 50 µM, B 55 µM and C 20 µM). The reference titration of 90 mM sodium into the CsCl buffer is shown in grey with the raw data slightly offset for easier visualization, while maintaining the scaling. The relative scaling was kept consistent within the three experiments. D) To verify the titration, a consecutive titration with citrate as injectant was performed. The buffer composition of the injectant was adjusted to the final concentrations of the previous sodium titration.

The sodium titrations were verified by a subsequent titration with citrate, as presented in Figure 3.17D following the titration of Figure 3.17C. The buffer composition was adjusted exactly to the salt concentrations after the final sodium injection, resulting in 13.3 mM NaCl in the CsCl buffer. The citrate titration shows a similar binding to all previous citrate titrations. The exothermic and exergonic binding (ΔH: -1143 cal/mol, ΔS: 19.9 cal/mol/deg) had a K_D of 6.41 µM. In comparison to the enthalpy at pH 6.5 measured earlier (ΔH: -889 cal/mol) the value for this titration was slightly higher. But along with the other parameters also the Hill coefficient at 0.233 is in the range of previous experiments.

A second experiment with sodium as the injectant was carried out in the presence of citrate at 1 mM in the sodium-free protein solution. The titration shows a significantly higher change in heat throughout the titration compared to the citrate-free samples. The shape of the heat curve, and thus the mode of binding was found to be different in this second titration. The background measurement titration of the injectant with 90 mM sodium to the buffer containing 90 mM CsCl and citrate depicted in grey rules out any negative effect of the experimental setup. Interestingly the enthalpic contribution of each injection increases up to a molar ratio of ~300 before showing a typical saturation behavior (Figure 3.17). Consequently, the binding of citrate to the protein seems to contribute significantly to the overall binding energy measured. The curve shape indicates more than one binding event. A fit with a sequential binding model results in two affinities of 4.7 mM and 9.9 mM.

The results for all sodium titrations show a titration curve that is not simply a sigmoidal curve or a part of one. One can appreciate that multiple individual curves added together result in the curve shape shown in Figure 3.16. in the later part of the titration a shallow sigmoidal curve whereas the initial titration includes a steep decay. This general type of curve indicates that the binding of sodium to SeCitS is not a simple binding but includes multiple components and possibly even sequential processes. Correlating the titration curves to the reference curves, it can be deducted that the complete saturation through the titration is not reached. The asymptotic convergence to the reference level was not completed with the amount of sodium added within the titration.

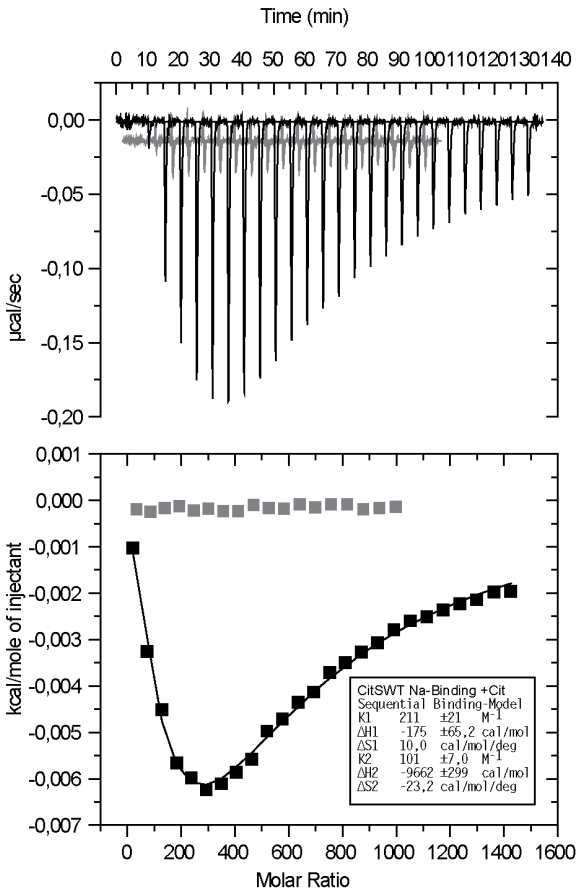

Figure 3.17: ITC titration of sodium to SeCitS with citrate. Protein with 1 mM citrate in the buffer was titrated with 90 mM sodium. The titration shows a significantly higher binding effect than samples without citrate. In a sequential binding model, the parameters for binding are listed in the inset box with an affinity of the sequential binding events of 4.7 mM and 9.9 mM. The reference titration of 90 mM sodium to the CsCl/citrate buffer is shown in grey with the raw data slightly offset for visualization purposes. The reference titration was stopped after 18 injections as a consistent baseline was visible.

The shape of the curve does not allow a simple evaluation of binding, so the thermodynamic parameters, which could be calculated for citrate binding, are not available in the case for sodium. An evaluation with a simple sequential binding model resulted in nonsensical parameters. The affinity given by K1 or K2 is calculated to be a negative value, which is not possible. Also evaluations with a two site binding model did not yield reasonable results. Generally it can be useful to consider the fit values obtained from an analysis of the data with different models. For example, when there is a competition for the metal ion, the one-site or two-sites models can provide accurate values for the binding enthalpy but the competition model is needed to obtain an accurate binding constant. When the isotherm contains two binding events, a comparison of the fit values with the one-site, two-sites and sequential binding models may provide evidence for an interaction between the two sites (Carpenter & Wilcox, 2014). In this setup it is not unsurprising to obtain a more complicated

ITC thermogram considering the structural circumstances of sodium binding. The first aspect to consider is that two sodium ions can be found within the monomer of the transporter. The binding sites for sodium are also in close proximity to one another and bridged by a structural water molecule. Together with the binding curve observed for sodium this indicates a dependence in the form of cooperativity in sodium binding. The expectation for the binding of sodium to the protein was an exothermic process, with the binding of the positively charged sodium ion compensating the negative charge of side chains in the binding site (Thomson & Ladbury, 2004). But as the overall change in heat is a composite of the heat contributions of all processes during the binding event, the effect of charge compensation is only one component in heat change measured in this binding event. Additionally to this charge compensation, other processes of the binding event, like a displacement of clustered water molecules, an opening of the sodium binding site to allow for entry and binding of the ions, and a loss in conformational degree of freedom of the protein upon binding to sodium ion, contribute to the overall change in heat in the system and thus a biphasic, initially endothermic then exothermic, reaction can be observed.

One aspect to consider is that since the proton is also a Lewis acid, metal ions, including sodium, will often compete with protons when binding to a protein. The pH of the solution and relevant pKa values will impose a sizable effect by defining certain concentrations of the basic form of the buffer, the protonation state of involved amino acids and other (de)protonations that interacts during the binding. These will have an impact on the experimentally measured binding equilibrium and particularly the binding enthalpy when there is a coupled (de)protonation of the buffer (Quinn *et al.*, 2016). The experimental enthalpy from ITC measurements would contain not only the heat associated with the sodium ion binding to the protein, which often displaces one or more protons, but also the dissociation of the buffer from the ion and association of any displaced protons to the buffer. It might be possible to exploit those pH-dependent changes to obtain improved binding curves, which allow a better evaluation, but this was not feasible within the scope of this thesis.

The titration curve of the titration of sodium to a mixture of citrate and protein resulted in a overall similar curve compared to the sodium-only titration. An endothermic part is followed by an exothermic component of the binding process. But it is remarkable that even though the concentrations of protein and sodium are kept the same, the change in heat is significantly more pronounced with single injection intensities over five times their relative sodium-only mount. This is a clear indication that there are additional contributions by other modes of binding. As citrate is now present in the mixture, an additional binding of citrate

could be made possible by the binding of sodium to the protein. The binding sites as determined in the wild-type structure allow for the assumption of a sequential binding of the substrates. The sodium ions seem to necessarily bind first in their respective binding site, also maintaining a defined order in their binding. Afterwards the citrate molecule can now bind in its now readily formed binding site, which occludes the sodium ions. This concept is substantiated by the fact that a significant change in heat, which can be correlated to an additional binding event, does occur when citrate is present for a sodium titration. Concluding the binding of sodium ions to the protein could either facilitate the formation of the citrate binding site or otherwise enable the binding of citrate which results in an additional contributions in the heat change which is substantially larger than the binding of sodium ions alone.

As the titration curve for the sample with citrate present has a more defined shape by an improved signal to noise ratio (grey vs. black curves), an evaluation using a sequential binding model was possible. The results for binding affinities are then calculated to be 4.7 mM and 9.9 mM. Those results are intriguing as those dissociation constants are in the same order of magnitude as the number determined during transport experiments at 3.3 mM. This results creates confidence that this approach in gaining knowledge about the binding mode of sodium is viable, albeit challenging in its experimental condition.

3.3.5 Calorimetric Study on Isocitrate Binding and Competition

Isocitrate was one of the most notable compounds tested during the transport experiments measuring the competition potency against citrate (see Section 3.3.1). As isocitrate was able to completely block the transport of citrate (Figure 3.12), the capacity of SeCitS to bind isocitrate was tested by measuring the effect of binding in the ITC.

The titration of SeCitS with isocitrate shows no significant binding (Figure 3.18A) even at an isocitrate concentration of 5 mM. The dissipated heat was nearly constant across the entire titration and within the range of background dilution heat. A subsequent titration with citrate shows the typical binding effect of citrate to the protein, demonstrating proper function of the protein. Citrate shows an exothermic binding to the protein. The evaluation of the binding curve with a one binding site model reveals binding parameters that are in accordance to other citrate-only titrations (compare Table 3.2). The K_D was calculated to

9.26 µM and is thus slightly lower but still within the same order of magnitude compared to other titrations. The Hill coefficient is 0.499, again corroborating the low stoichiometry of citrate to the transporter. The change in enthalpy and entropy, ΔH at -1910 cal/mol and ΔS 16.6 cal/(mol*K) integrate well into previous data analyzing the effect of pH on the citrate binding (Section 3.3.3)

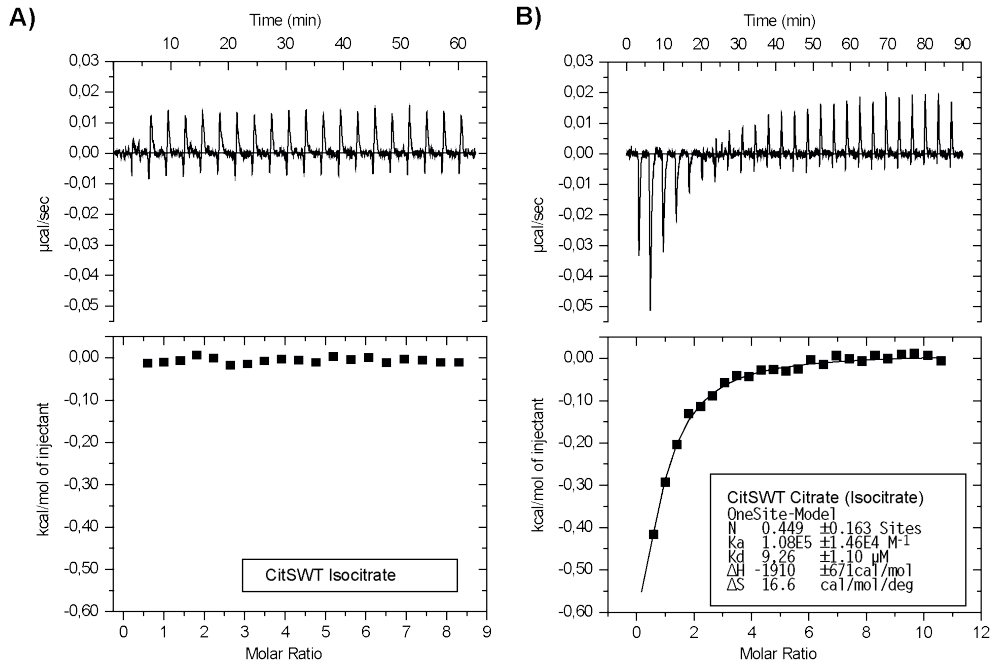

Figure 3.18: ITC titration with isocitrate as substrate for SeCitS. Citrate-free SeCitS was titrated with isocitrate at 5 mM without any significant binding observed (A). To determine the binding capacity to the original substrate, the sample was subsequently subjected to another titration with citrate (0.5 mM), revealing a binding event comparable to previous titrations (B). The scaling was kept consistent with other citrate measurements.

Concerning isocitrate as a possible alternative substrate it can be derived that although isocitrate is able to inhibit citrate transport the affinity has to be in the very high micromolar range or above as the ITC measurements did not allow an evaluation of the titration leading to either the conclusion that it does not bind, which would contradict the transport competition experiment or the c-value of the system (as described in section 3.3.2) is below 5, small enough to flatten the titration curve into not being analyzable. Even extrapolating at an ideal protein concentration of around 100 µM the maximal affinity measurable with ITC would only be a K_D of 30 µM.

Unfortunately, neither of the experiments using isocitrate as an alternative substrate allows a distinct conclusion if isocitrate is indeed transported by SeCitS. The results show that isocitrate is certainly able to loosely occupy the citrate binding site. This is reflected in the

inhibition by a thousand-fold competition of isocitrate to the native substrate citrate, which even with a low affinity reduced the apparent transport rates of SeCitS. This finding is seemingly contradicted by the results of ITC binding experiments, which show no binding of isocitrate to the transporter. Nevertheless the validity of the ITC results is limited to a certain range of affinity. As concluded by c-value estimation the ITC results add that the affinity is at least 10-15 times lower than that of citrate.

3.4 Role of Substrate-Coordinating Residues in SeCitS

Comparing the structure of citrate and isocitrate it is interesting that such a small structural difference may result in severely altered binding behaviors to the transporter. This is especially intriguing as other members of the 2HTC family have a much broader specificity range. Within the family of 2HTC transporters, which also includes some exchangers, there is a wide variety of substrates. To accommodate the different substrates the binding site of the transporter feature some different amino acid make-ups in the substrate binding sites. To understand why the specificity of SeCitS is constrained while other proteins of the family are more promiscuous in their substrate selection a mutagenesis approach was taken. As it is a common method to explore functional intricacies within proteins the key residues of the binding site were selected for point mutations. Through the comparison of wild-type and mutant SeCitS, a better understanding of the protein in terms of binding, transport and structure can be achieved. The crystal structure served as a valuable basis to design SeCitS mutants. The target amino acids were varied from simple alanine replacements to changing the length or the charge of the side chain. The mechanics of the transporter dictate that the high-affinity binding site for citrate is in the outward-open conformation. Along with the overview in the structure (Figure 3.20), the interacting amino acids and their respective contributions to the binding of this conformation were visualized to assist with the generation of mutations in SeCitS (Figure 3.19) (Laskowski & Swindells, 2011). Citrate is tightly coordinated by a number of amino acids that were chosen to be targets of single point mutations. The most obvious variants were amino acids R402 and R428 that coordinate the citrate directly by ionic interactions.

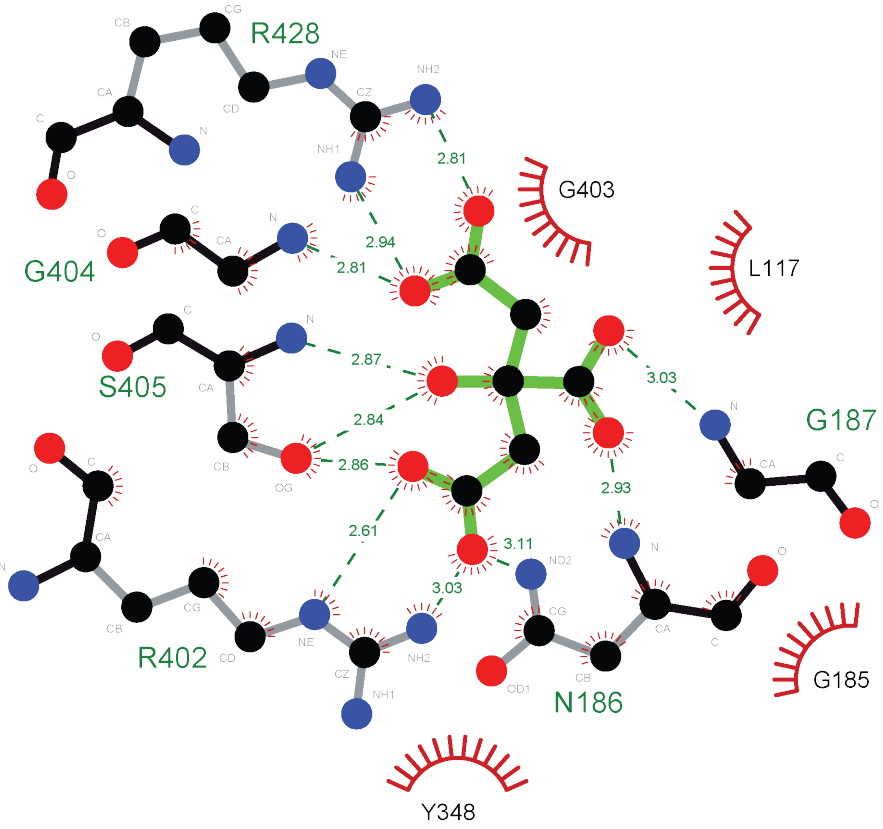

Figure 3.19: Interaction of citrate in the outward-facing conformation. Citrate is coordinated mainly by ionic interactions to the side chain of R402 and R428. (LigPlot+ of pdb 5A1S).

R428 is the residue with a high conservation within the family of 2HCT. This residue is involved in citrate binding in both conformations of the transporter. To investigate if transport activity or binding capacity depend on this moiety, both a mutation to retain and to invert the charge were chosen, with the conservative mutation of R428K and R428E inverting the charge of the residue, alongside a simple alanine mutant R428A.

In the crystal structure, R402 contributes two coordinating interactions, one hydrogen bond and an ionic interaction to the binding of citrate in the outward-open position. In other members of the 2HCT family, this residue is not a positively charged amino acid. In CitP of *Leuconostoc mesenteroides* and MleP of *Lactococcus lactis* the amino acid in this position is methionine, whereas CimH of *Bacillus subtillis* and CitW of *Klebsiella pneumoniae* feature a glutamine. Those transporters are also capable of transporting other substrates than citrate, such as malate and acetate. In addition with an alanine mutation, those comparisons gave rise to R402A, R402M and R402Q.

Other interesting targets for mutations were the amino acids in the hairpin loops. The hairpin loops contain the GGXG motive that enables tight turns of the hairpin loops and also binding of sodium. The single other amino acid within the hairpin loop H6 is an asparagine. Comparing this position to other family members of the 2HTC family methionine (MleP) and valine (CimH, CitW, CitP) were found in this position. The mutants N186A, N186M and N186V were thus chosen to be investigated.

D407, an amino acid flanking the GGXG of the hairpin loop H12, and subsequently also within the periphery of the tips of the hairpin loops, was investigated as it is involved in sodium binding within the transporter. This amino acid was identified to feature an asparagine in CitP and MleP and consequently a D407N mutant was devised.

In addition, R205 was chosen as it forms a salt bridge with D112 in the inward-facing conformation. This salt bridge is formed in every transport cycle and disrupted for the back cycling into the outward conformation. A mutation to the opposing charge (R402E) would prevent the formation of that salt bridge and could even lead to an increase in the speed of the transport cycle.

Based on sequence and structural analysis, molecular dynamics simulations of the ligand selectivity suggested double and triple mutants: R402M/N186M, R402L/N186I, R402M/N186M/L337T (Ahmadreza Mehdipour, personal communication). The involved amino acids were also tested as single mutants. These mutations, in combination, should change the ligand binding by decreasing the selectivity towards citrate and increasing the affinity for malate and lactate.

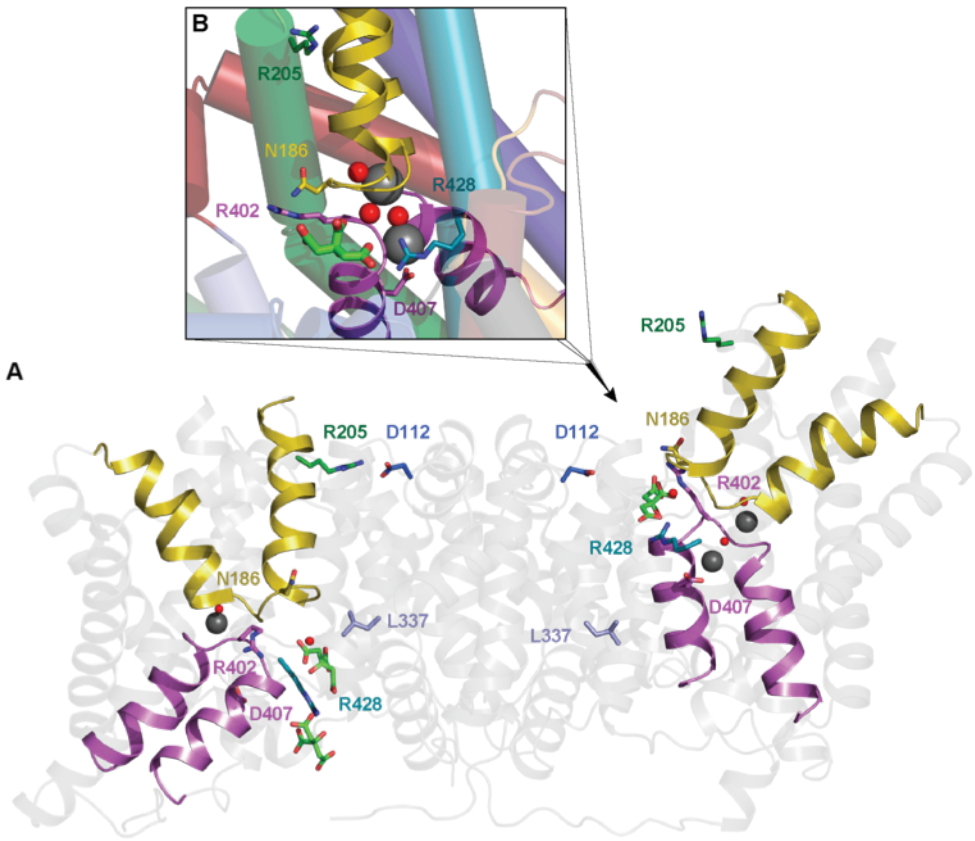

Figure 3.20: Overview of the residues selected for mutation in SeCitS. In addition to ionic interactions by the two aforementioned arginines, hydrophilic contacts of residues from both helix hairpins contribute to the tight citrate binding. Each helix hairpin contains the GGxG sequence motif (GGN186G and GGS403G).

The crystal structure shows two locations where citrate can be found in the inward-facing conformation, marking its trajectory leaving the transporter, but neither of those positions features coordination of the citrate, which could be used for creating other mutations in that region.

With a number of SeCitS variants with point mutations designed, functional studies were done to investigate the effects of the mutations. The overexpressed point mutation variants of SeCitS was purified according to the $SeCitS_{WT}$ strategy. Some of the mutants showed purification results very comparable to the wild-type protein, both with regard to the relative amount of purified protein and the shape of the size-exclusion profile (Figure 3.21), whereas others mutants did not yield as much pure protein.

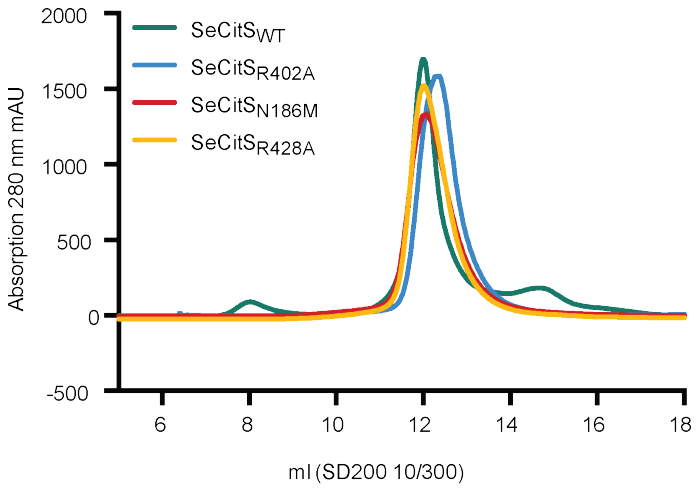

Figure 3.21: Size-exclusion chromatography of variants of SeCitS. Profiles of selected point mutants show an elution profile comparable to the wild-type protein in size and yield.

All mutants were expressed and purified to be tested in crystallization trials and in the transport assay. While for example the shown mutants purified analogous to the wild type, the yield of stable protein was very low in a few of the tested mutants. Instead of following the liposome reconstitution approach, cell-based transport was measured and normalized to the protein quantity. This also allowed for a higher throughput and the inclusion of mutants that were unstable when purified.

3.4.1 Transport Activity of Mutant SeCitS

All tested mutants showed a reduced transport activity when compared to the wild-type protein (Figure 3.22). The mutants of R402 (SeCitS$_{R402A}$, SeCitS$_{R402M}$ and SeCitS$_{R402Q}$) and R428 (SeCitS$_{R428A}$, SeCitS$_{R428E}$ and SeCitS$_{R428K}$) showed a near total loss in transport activity. N186 mutations differ in activity depending on the new amino acid, with SeCitS$_{N186A}$, and SeCitS$_{N186M}$ retaining about 65% of transport activity, while SeCitS$_{N186V}$ activity is only at about 10%. Also, combinations of different mutations of N186 and R402 (SeCitS$_{N186I-R402L}$, SeCitS$_{N186M-R402M}$, and SeCitS$_{N186M-L337T-R402M}$) follow the pattern of R402 mutations as the transport activity is below 10% wild-type level. The highest relative activity level was observed for SeCitS$_{R205E}$ with about 80% transport activity compared to the wild-type protein. A mutation in D407 (SeCitS$_{D407N}$) also stalled the transport.

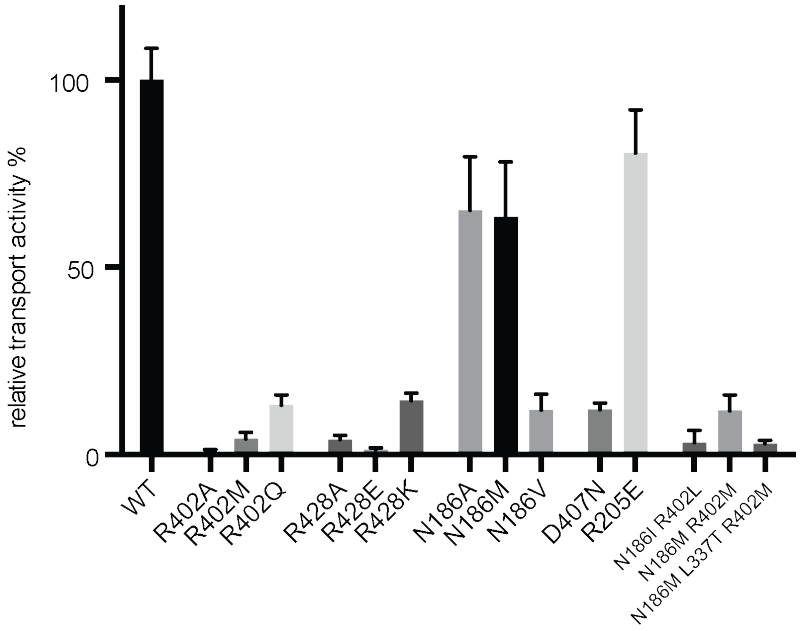

Figure 3.22: Transport activity of SeCitS mutants. Uptake of ^{14}C-citrate into live *E. coli* BL21 C43 cells after expression of wild-type or mutant SeCitS was measured. Measurements were corrected for different expression levels of mutant protein as determined by quantitative Western blot analysis. Transport activity of wild-type SeCitS was set to 100%.

In the outward-open position citrate is bound by two ionic interactions with R402. The transport rates of mutants of this residue are greatly reduced. In comparison to both other mutants ($SeCitS_{R402A}$ and $SeCitS_{R402M}$) the exchange to glutamate still shows the highest retention of activity.

The highly conserved R428 is involved in citrate binding in both conformations of the transporter. The exchange of this arginine abolishes citrate transport. Even the very conservative mutation to a lysine reduces the activity to 10%.

The interaction of N186 with the substrate is mainly mediated by the backbone of the polypeptide chain. Subsequently the mutation to alanine or methionine only reduces the activity to 80%. Interestingly the mutation to valine reduces the activity to below 10%.

A combination of mutations in R402 and N186 were proposed as those amino acids are in close proximity and correlated. All tested combinations exhibit the same reduced activity as single mutants of R402. The presence of a N186 mutation cannot rescue the activity.

After testing different mutations in the citrate binding site, D407 involved in sodium binding was measured. Both sodium atoms in their outward conformation are mostly coordinated by the backbone in the hairpin loops of the helix bundle. Elimination of the negative charge needed for coordination of sodium Na2 by mutation of D407 to asparagine abolishes citrate transport.

A near wild type activity is observed for R205E. This residue forms a salt bridge with D112 in the inward conformation. A disruption of this salt bridge does not seem to significantly alter the activity of the transporter.

3.4.2 Measuring Substrate Binding to SeCitS Mutants

Different mutants of SeCitS were tested by ITC titration for their citrate binding capacity. Most of the mutations targeted amino acids that are in direct contact with the citrate in the outward conformation (Section 3.4). As purification and stability of some of the mutants proved to be challenging, not all mutants that were used for transport measurements could be used for binding experiments in the ITC, due to the high protein concentration required. Mutants tested in the ITC were all variants of R402, namely R402A, R402M and R402Q. Furthermore, N186M was tested as well as R428A and R428K. The measurements were set up analogously to the citrate titration in Figure 3.16. The protein was subjected to two steps of dialysis against a citrate-free buffer and a size-exclusion chromatography to obtain a homogeneous sample. The concentration of protein was adjusted to approximately 20 µM, ranging from 16.7 µM to 24.1 µM, depending on the mutant. Citrate was again used at a concentration of 0.5 mM to maintain comparability. The results of the six tested mutants are shown in Figure 3.23. The scaling was chosen to be in line with previous wild-type experiments as presented in Figure 3.15.

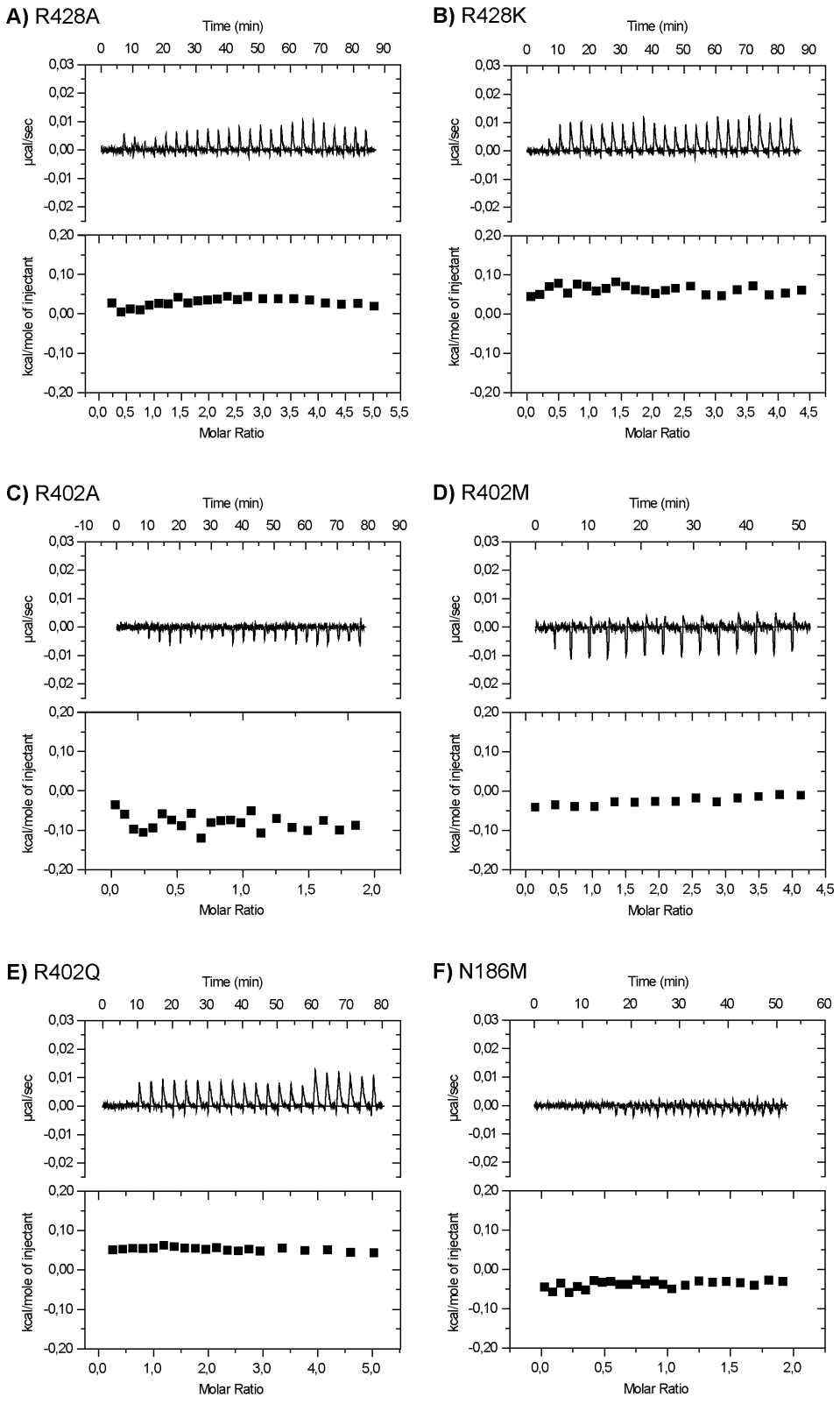

Figure 3.23: ITC-Measurements of different SeCitS mutants. SeCitS mutants A) R428KA, B) R428K, C) R402A, D) R402M, E) R402Q, F) N186M were titrated with 0.5 µM citrate. For comparison, the same scale as in WT measurements was used to plot the data. For none of the mutants a measurable binding was observed.

In all experiments of the mutants, the heat change was comparable to background mixing effects. The resulting changes in integrated heat were constant across the range of titrations. From those results it is apparent that in neither of the mutants a binding event was detected.

To see if a change in specificity was achieved through a mutation of an amino acid in the citrate binding site, an experiment with isocitrate as target substrate was tested. Analogous to the wild-type SeCitS, the mutant $SeCitS_{R402M}$ was tested for its respective binding of isocitrate. To validate the results of the isocitrate binding, the titrated protein was subsequently used for a citrate binding titration.

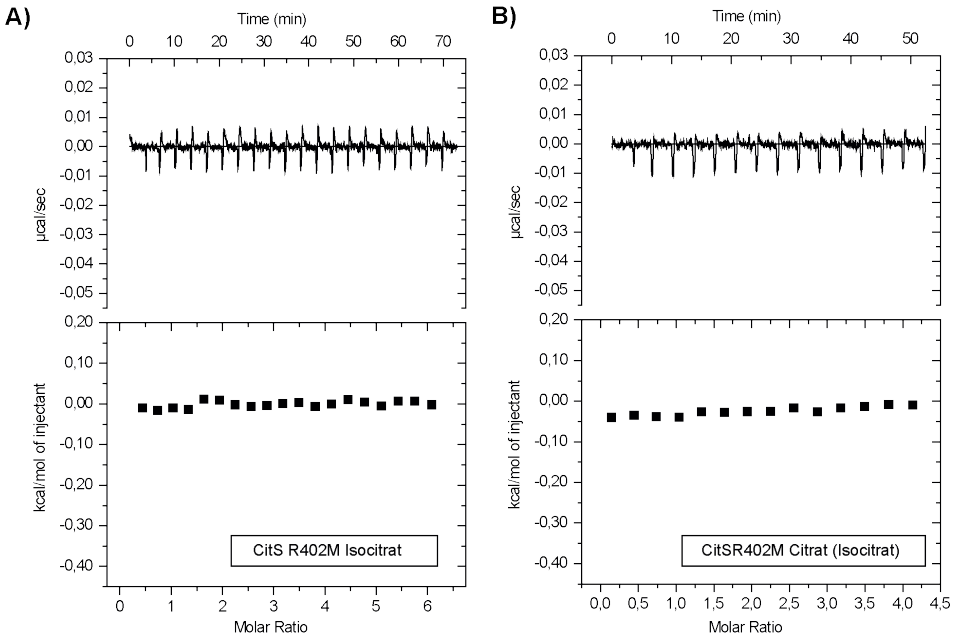

Figure 3.24: ITC titration with isocitrate as substrate for SeCitSR402M. A) Citrate-free SeCitSR402M was titrated with isocitrate at 5 mM without any significant binding observed. B) Subsequent subjection to another titration with citrate (0.5 mM), the sample did not show any binding to citrate either. The scaling was kept consistent with other citrate measurements.

In the isocitrate titration with $SeCitS_{R402M}$, a similar titration pattern as in the wild type (Figure 3.18) was observed. The lack of change in integrated heat shows that there is no measurable binding of isocitrate to the mutated protein. In contrast to the wild-type protein, the subsequent titration with citrate shows also no binding to the protein.

The choice of mutations applied to SeCitS was derived from some basic principles. All tested mutations can be classified into three groups of mutations: alanine substitutions, conservative substitutions and sequence alignment derived substitutions and present their unique value concerning the mutation results. The details of the transport data of the single mutants and their role in citrate binding are discussed below.

R402

One of the two main arginines involved in the high-affinity binding of citrate in the outward conformation is located at the tip of the second helix hairpin (H12). Neighbouring glycines contribute interactions to the sodium ions. As seen in the crystal structure, the side chain not only provides a positive charge to compensate for the charge of the citrate but it also directly coordinates the citrate via two hydrogen bonds. One of the hydrogen bonds is provided by one of the η-nitrogens, whereas the second bond is provided by the ε-nitrogen. This interaction is one of the closest interactions with the substrate at 2.61 Å. So when those interactions are disturbed by a non-ideal coordination of the citrate the transport and also the binding are hindered for mutation of R402.

R428

It was previously shown that arginine R428 plays an important role in the binding of substrates in the entire family of 2HTC transporters (Bandell & Lolkema, 2000). This is also reflected by the high conservation of this residue. Thus it is not surprising that the replacement of the positive charge to a negative (R428E) completely abolishes any transport activity. Similarly, also the elimination of any charge trough the introduction of alanine (R428A) does not allow any transport of citrate. Interestingly the very conservative mutation to a lysine (R428K) is already enough to reduce the transport activity to less than 15% compared to the wild type. This allows for the hypothesis that a very close coordination of the citrate is essential for the start of transport.

N186V

Two mutations at N186 only showed a reduction in activity to 60% compared to the wild type. In N186 the backbone and the δ-nitrogen are involved in the binding of citrate. A mutation to the smaller alanine and the slightly polar methionine interfere little with the transport, as the main coordination of the citrate via R402 and R428 enables proper binding. The interesting mutation is the replacement of the aspargine with valine (as in CitH/W/P, see Section 3.4) which leads to a near complete inhibition of the transport. In the outward

conformation the amino acid is solvent-exposed and not restricted by neighbouring side chains. In contrast, the inward conformation has the residue buried between helices 3, 7, and 10. This might also explain why a mutation to the beta-branched valine reduces the transport activity. Here it might form a hydrophobic cluster, which could energetically favour the inward conformation. Reexposing the hydrophobic valine to the solvent in the outward-facing state would present as an energetic barrier that prevents the transporter to return to its outward position to start another transport cycle.

D407N

The aspartate at position 407 is widely conserved within the 2HTC family. The main exceptions are proteins that are substrate/product exchangers like CitP and MleP, which have an asparagine in its place. The transport activity of the respective mutation is effectively abolished. This is intriguing as the suspected opening of the specificity was not accompanied by a loss of activity towards the transport of citrate, especially as one of the exchangers used as reference for the mutation has citrate as one of its substrates.

R205E

In the inward conformation the crystal structure shows a salt bridge on the periplasmic side of the transporter (D112-R205). The idea behind a R205E mutation was the disruption of the salt bridge to enables a faster return to the outward conformation within the transport cycle, which is assumed to be the rate-limiting step. Within the framework of the presented data this hypothesis cannot be supported for this mutant. As the general turnover of the protein is relatively low (1.2/minute per protomer at pH6 and 25°C) it can be assumed that this timeframe would allow for the salt bridge to form and open multiple times. As the activity of the mutant is close to the activity of the wild-type protein it could also be suspected that compensating effects come into play, where the disruption of the salt bridge enable a faster transition but is hindered at a different stage.

In ITC measurements there was no apparent binding of citrate to any of the tested mutants. This is in some cases contradicting the results from the transport experiments. The main reasons for no apparent binding to the protein were the limitations of the technique itself. ITC experiments rely on strong endothermic or exothermic events during binding. The maximal affinity that can be measured depends strongly on the concentration of the protein in the cell and is in this case limited to affinities in the µM range as described above (section 3.3.2). As membrane proteins present a challenging target, especially concerning amount of

purified protein and stability in highly concentrated solutions, this presents an inherent obstacle. This is especially true for the variants of SeCitS tested in this work as the purification and stability were impacted negatively by the mutations. Following those limitations it can still be concluded that the affinity for any of the mutants retaining a relative activity above 15% can be in the high micromolar range or above. That means that already a reduction in affinity by a factor of 10 may lead to non-detectable binding curve in the ITC under non-ideal setup conditions. Those results again show the complexity of ITC measurements concerning the c-value and its implications on the affinity range that can be identified with this technique. Given the previous results that demonstrated a high specificity for SeCitS, even a minor change in the system of interactions for citrate binding may be sufficient to alter and gravely reduce the affinity towards its substrate.

3.5 Structural Investigation of SeCitS and its Variants

Along with a functional characterization of the mutants, structural investigation was used to gain insight into SeCitS and its variants. The structure of a protein is invaluable to help understand the function and mechanism of proteins and formulate new questions in regard to those properties. The crystals structure of native SeCitS was used to propose mutations within the citrate binding site. This is not only helpful for functional studies as above but also would allow a better understanding of the information obtained in the binding and transport studies and may help better understand the path of the citrate within the protein during its transport cycle.

3.5.1 Crystallization and Crystal Growth

In crystallization trials, the highly concentrated protein was set up as hanging drops. For each preparation of protein, a fine screening around the initially obtained conditions was performed to ensure optimal crystal growth. Wild-type SeCitS crystallized under conditions of 100 mM MES pH 6.5 with 150-200 mM NaCl and 28-30% PEG 400 in different shapes, mainly long needles, rod-shaped with a broad base and as flat crystals (Figure 3.25).
To find additional binding sites to be able to better map the path of citrate, crystallization setups also included the wild-type protein supplemented with an excess of citrate. Crystals

prepared with a high concentration of citrate (more than 10 mM) were difficult to retrieve from the droplet. The ones that were tested in the X-ray beam never showed high diffraction (resolution not better than 10 Å) if crystals were still viable. At the other end of the spectrum SeCitS, void of residual citrate, crystallized but showed the same result with insufficient resolution to obtain datasets. In an effort to crystalize sodium-free SeCitS, as prepared for ITC measurements, different crystallization screens were tested. As dedicated sodium free screens were not available the selection of suitable conditions was difficult and subsequently did not result in crystals suitable for data collection.

As the conventional crystallization approach did not yield good-diffracting crystals, a different approach using the lipid cubic phase (LCP) method was taken. For this method, the protein is mixed with monoolein, which leads to the formation of different multidimensional phase systems with continuous membranes and enables crystal growth in a membrane environment. This kind of crystallization proved to be helpful in obtaining crystals and structures of numerous different membrane proteins (Caffrey & Cherezov, 2009). The protein-monoolein-mix was regularly checked under a light microscope and with the help of UV light, as protein crystals appear as a fluorescing spots with sharply defined edges. The overall amount of crystals found in the screens was low, with only 2-8 hits per 96-well setup. All LCP crystals were harvested and tested in the X-ray beam, but only one third of the tested loops did contain protein crystals that diffracted; the others either contained salt crystals or seemed to be LCP matrix only. For those protein crystals, diffraction never provided a resolution better than 10 Å. After testing a variety of screening tests and plate setups it was deemed more efficient to continue an optimization of crystals obtained by the hanging drop method.

Crystallization of SeCitS mutant proteins was tested under similar conditions as the wild-type protein. The most prevalent shape of crystals was similarly a 200-400 µm long rod-shaped crystal (Figure 3.25F). The diffraction of the rod-shaped crystals, when tested in the X-ray beam, was weak with spots only reaching a resolution of up to 4-8 Å. This resolution was not deemed high enough for a reasonable structural analysis. The cubic shaped crystals that were obtained for the analysis of the wild type as described earlier (Wöhlert *et al.*, 2015) could not be reliably reproduced.

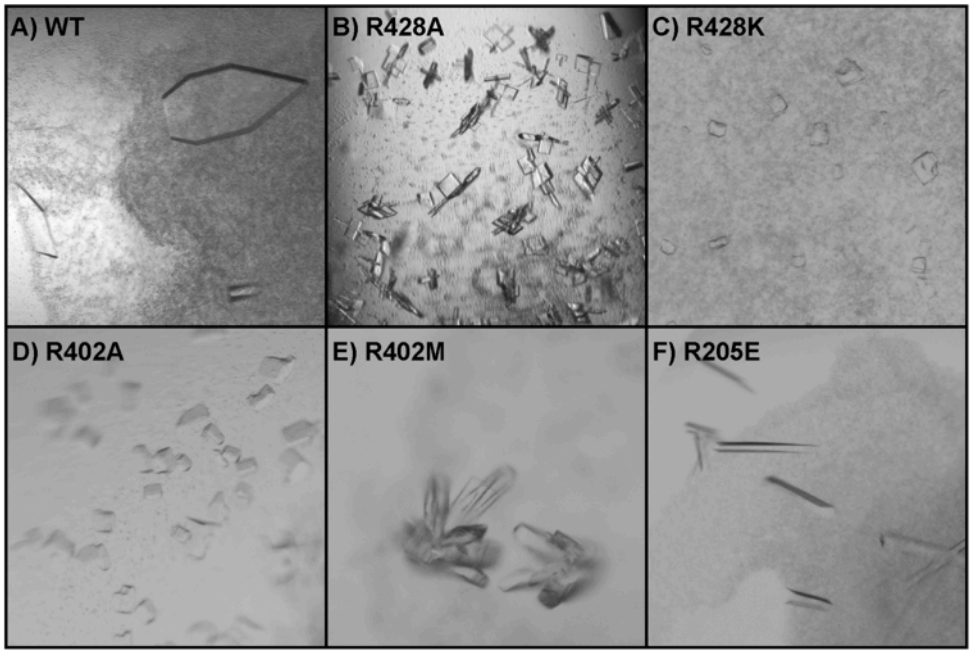

Figure 3.25: Crystals of SeCitS and single point mutants. Wild-type SeCitS (A) and single point mutants of SeCitS (B-F) were prepared in hanging drop crystallization setups and gave crystals of different shapes.

An assortment of different crystals tested is presented in Figure 3.25. The test images collected to assess the diffraction of the crystal were used to perform an initial indexing of the data. As the resolution of the crystals was often low and the initial assignment of a space group relied on only three images the results indicate a potential space group (Table 3.3).

Table 3.3: List of tested crystals with their highest resolution and suggested space group. The last two rows indicate the two previously deposited structures of native and seleno-methionine SeCitS.

Crystal	Resolution (best)	Space-group	a	b	c	α	β	γ
WT (high citrate)	5 Å	P4	89.9	89.9	155.5	90.0	90.0	90.0
R428A	7 Å	P4	89.7	89.7	154.7	90.0	90.0	90.0
R428A	7 Å	P222	87.6	162.1	189.4	90.0	90.0	90.0
R428K	3.3 Å	P4	89.2	89.2	152.3	90.0	90.0	90.0
R402A	15 Å	P1	111.3	156.7	217.8	105.4	100.2	85.2
R402M	10 Å	P4	88.8	88.8	165.3	90.0	90.0	90.0
R402M	8 Å	C222	177.5	326.6	90.5	90.0	90.0	90.0
R402Q	10 Å	P222	93.0	111.4	118.2	90.0	90.0	90.0
R205E	5.5 Å	P4	90.5	90.5	154.1	90.0	90.0	90.0
N186A	4.5 Å	P1	85.1	87.9	90.2	89.9	113.3	98.5
N186A	10 Å	P4	92.0	92.0	160.9	90.0	90.0	90.0
WT	2.5 Å	P1	86.4	89.9	91.8	90.4	113.8	99.5
SeMet	3.9 Å	P2	90.9	168.8	97.9	90.0	91.0	90.0

The majority of crystals presented as tetragonal P4 crystals. The most prevalent space group was represented in nearly all the tested mutants. The general unit cell size was around 90 Å by 90 Å by 155 Å with all angles at 90°. Orthorhombic P222 crystals also formed, but did not yield high-resolution diffraction.

The data of the crystals that were used to solve the published $SeCitS_{WT}$ crystal structure are listed as well. The space group of the native SeCitS cube-shaped crystals was P1, while the seleno-methionine crystals were P2 with a rod-shaped appearance. As the third angle in the SeMet crystals were close to 90.0° a misassignment to P4 was seen, if only few images of the SeMet dataset were chosen. The same effects were observed in a lot of cases where a P4 symmetry is suggested as the other parameters of the unit cell after very similar to the unit cell observed for the SeMet crystal. This is especially true as $SeCitS_{R428K}$ is proposed to be a P4 symmetry, but during processing (Section 3.5.2) the space group was identified to be P2. In crystals of $SeCitS_{N186A}$ a P1 symmetry was found. The interesting aspect is that the crystal has one of the highest resolutions compared to the other ones tested and displays the same parameters in space group dimension as the wild-type crystals that diffracted to ~2.5 Å. Those cubic-shaped crystals were very rare. This observation combined with the information that only those crystals contained two asymmetric dimers whereas the P2 crystals of SeCitS with seleno-methionine contained only one asymmetric and one symmetric inward-facing monomer could suggest that the asymmetric conformation is a stable but not completely favorable conformation for the dimer.

3.5.2 Data Collection, Processing and Refinement

The highest resolution obtained for a mutant SeCitS was $SeCitS_{R428K}$ with a resolution of 3.4 Å. Data was collected at the X-ray beamline PXII at the Swiss Light Source (Paul-Scherrer-Institute, Switzerland) equipped with a PILATUS 6MF detector. Two datasets originating from one crystal were collected with offset starting angles (30° and 80°) to achieve high completeness of the data. The sets of 960 and 720 images were collected at an increment of 0.25° oscillation per image. As the space group of the crystal with the highest certainty was suggested to be P2 (P 1 2_1 1), this covered the range of essential diffraction angles and led to a multiplicity of 4.4. A representative diffraction image is shown in Figure 3.26 with the spots extending to 3.3 Å. Data collection statistics can be found in Table 3.4.

Table 3.4: Data collection statistics of SeCitS$_{R428K}$.

SeCitS R428K	
Beamline	SLS PXII
Wavelength	0.979
Spacegroup	P 1 21 1
Cell dimensions a, b, c (Å) alpha, beta, gamma (°)	 87.3, 152.9, 90.4 90.0, 90.6, 90.0
Resolution (Å)	48.68-3.45 (3.64-3.45)
R_{pim}	0.049 (0.655)
I/sigma I	12.0 (1.5)
CC*	1.000 (0.571)
Completeness (%)	99.5 (98.3)
Multiplicity	4.4 (4.3)

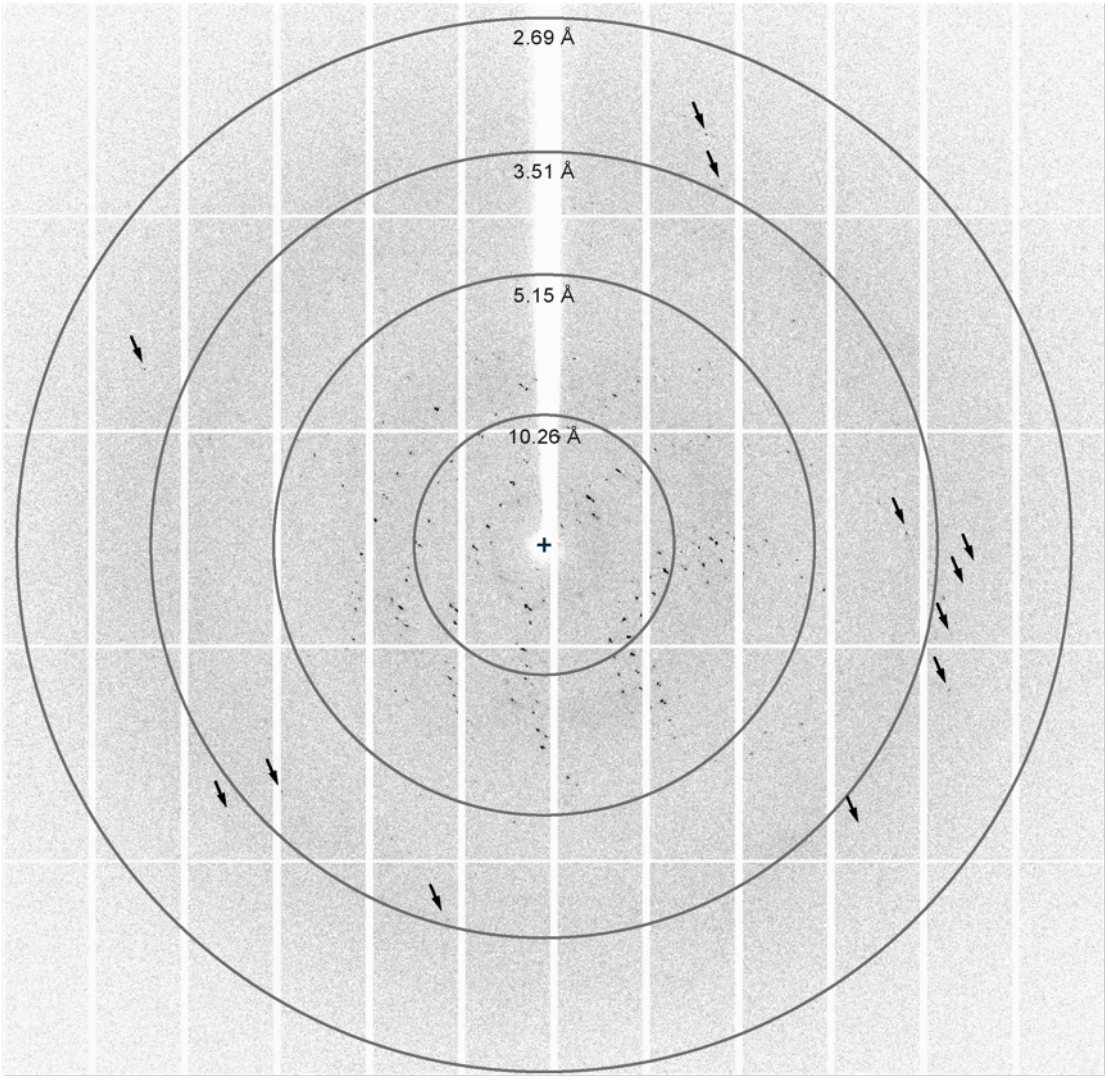

Figure 3.26: Diffraction image of SeCitS$_{R428K}$ crystal. The crystal diffracted up to a resolution of 3.3 Å. Data was processed to a resolution of 3.4 Å.

The data set was processed to a resolution of 3.45 Å. The structure was solved by molecular replacement using the wild-type structure as search model. The initial separate processing of the two datasets was performed with XDS and the data was combined and scaled in AIMLESS. Automated refinement was initiated with refmac and resulted in a model with a R_{work} of 36.0 and a R_{free} of 37.3. Iterative manual model building in coot and intermittent refinement with phenix could improve the model to a R_{work} of 27.2 and R_{free} of 31.7. The refinement statistics can be found in Table 3.5.

Table 3.5: Refinement statistics of SeCitS R428K.

SeCitS R428K	
Resolution (Å)	48.68-3.45 (3.50-3.45)
Unique reflections	60526
Reflections in test set	2942
Rwork/Rfree	27.23/31.73 (39.09/42.13)
CCwork/CCfree	0.873/0.879 (0.494/0.392)
Average B-Factor ($Å^2$)	143
No. Atoms in AU	12882
Protein	12661
Ligand	208
Water	13
r.m.s. deviations Bond lengths (Å) Bond angles (°)	 0.002 0.762

Of all amino acids in the refined structure, torsion angles of 94.56% of the residues were in preferred regions. In additional 4.13% of the residues ϕ and ψ angles are in allowed regions and outliers make up only 1.32% of the residues. A visual representation of those results is shown in the Ramachandran plot (Figure 3.27).

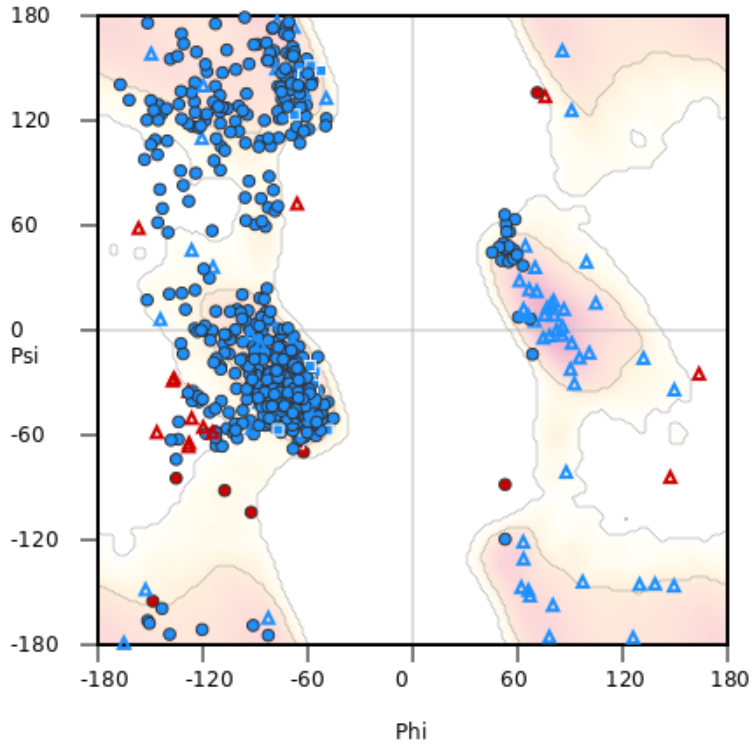

Figure 3.27: Ramachandran plot of the SeCitS$_{R428K}$ structure. The representation of the peptide bond angles for all amino acids in the unit cell indicates that 94.56% of the residues are in preferred regions. Another 4.13% of the residues are in allowed regions and 1.32% of the residues show outliers in their ϕ and ψ angles. The Ramachandran plot includes glycine residues (triangles) and prolines (squares).

Solving the structure of SeCitS$_{R428K}$ with the given structural information was readily solved using the wild-type structure as a search model for molecular replacement. The most challenging part was identifying the relevant conformations as the conformational configuration of the SeCitS$_{R428K}$ mutant was different to the wild-type structure (further discussed in section 3.5.3). Previously solving the structure of SeCitS$_{WT}$ was only possible through the use of single-wavelength anomalous scattering using a crystal of a seleno-methionine sample of SeCitS and then expanding the resolution by molecular replacement using the native crystal dataset.

3.5.3 R428K STRUCTURE

The crystal structure of $SeCitS_{R428K}$ contains four molecules per unit cell arranged in two homodimers per unit cell. The dimers are offset against another by 90 degrees. One of the dimers consists of two inward-facing monomers, whereas the other one is asymmetric with one inward-facing conformation and one outward-facing conformation (Figure 3.28). The difference to the outward-facing conformation is higher than 6.2 Å. Most of the residues could be fitted into electron density, while the resolution limited the exact placement of some flexible loops, for example around amino acids 260-300.

Within the protein, several citrate binding sites were identified, as additional electron density matched the placement of citrates in the wild-type protein (Figure 3.29, Figure 3.30). The resolution was not sufficient to identify separate densities for the sodium ions or structural waters. Additional densities that could not be covered by the protein sequence could partially be assigned to other molecules carried over from the purification and from the crystallization setup, like MES, the buffer used for crystallization. Density between the interfaces of the two monomers was interpreted as an alkyl chain, which was also present in the wild-type structure and could either be a lipid or a detergent molecule filling a very hydrophobic elongated cavity in the middle of the dimer. Additionally density for two detergent molecules was found in the periphery of the protein.

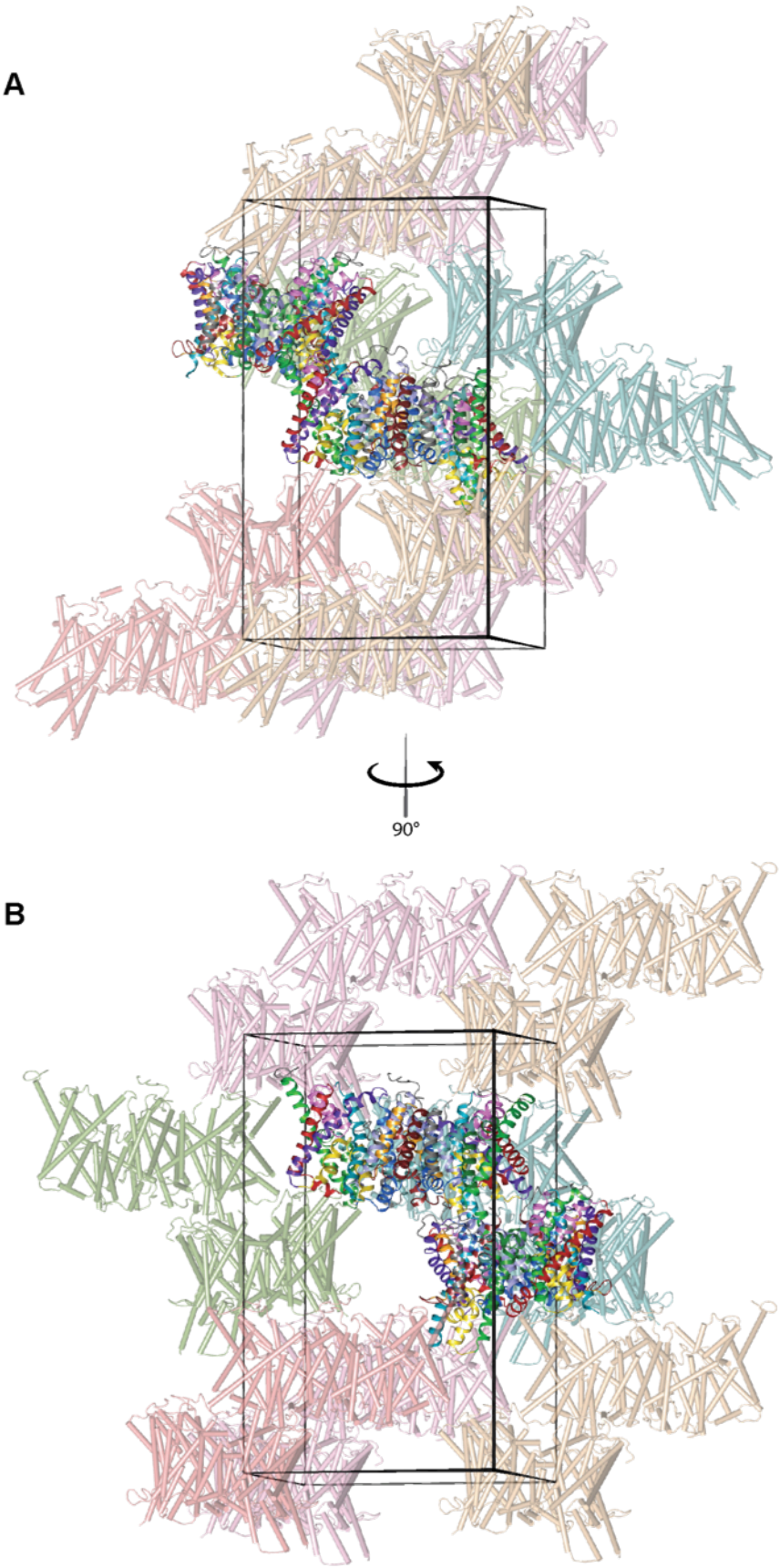

Figure 3.28: Overall structure of SeCitS$_{R428K}$ and arrangement of dimers in the unit cell. The unit cell contains two dimers in total. One is a symmetric dimer with both its protomers in the inward-facing conformation and the other one is asymmetric. The dimers are rotated by about 90°C from another in A) to B).

Comparing the wild-type structure to the structure of $SeCitS_{R428K}$, the overall RMSD of the asymmetric dimers is 0.52 Å. Effectively the mutation only results in a very small structural variation from the wild-type protein. As the electron density is not as defined compared to the wild-type structure, it could not be determined where the sodium ions are located.

The substrate binding site in the outward-facing conformation overlays well to the wild-type structure (Figure 3.29). The resolution of the structure does not allow identification of the sodium ions, nor any structural waters in the binding site. The biggest difference is in the orientation of the side chain of the mutated arginine. Mutated to a lysine, the residue is able to reach a bit higher, due to an elongated alkyl chain and binds the citrate carboxylate in a different angle.

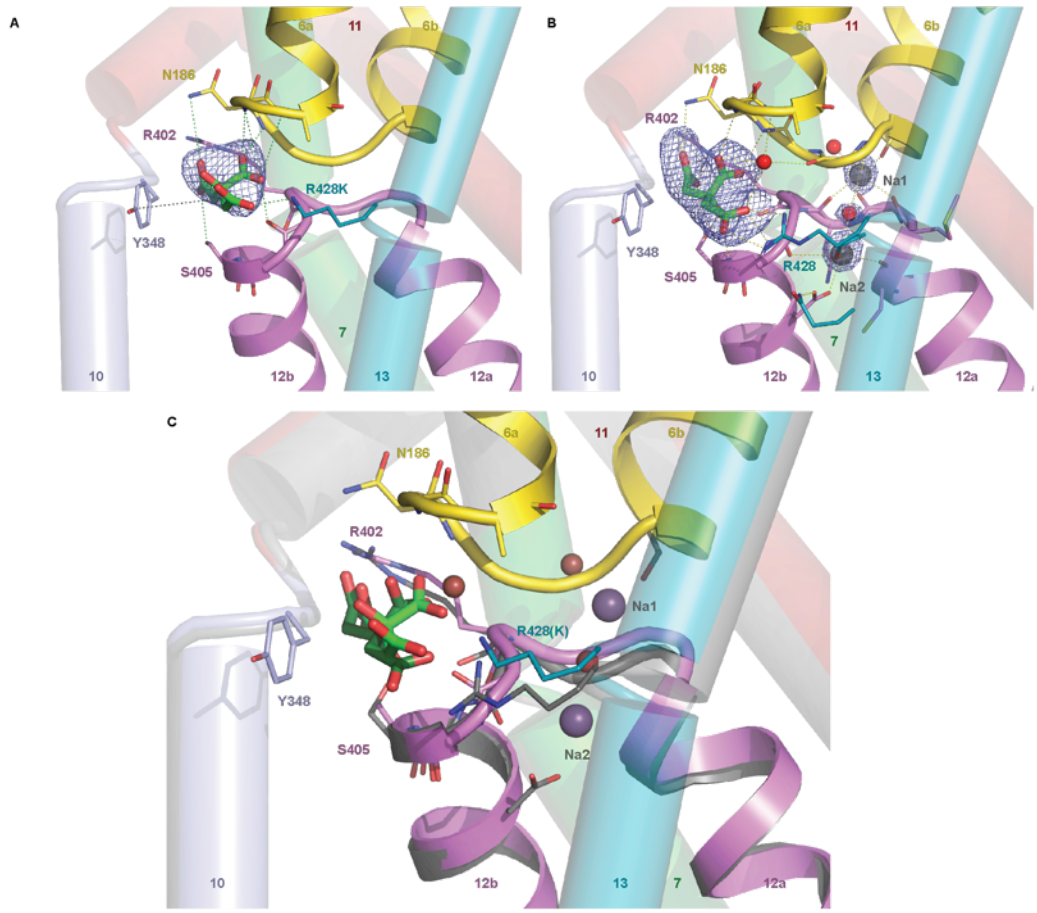

Figure 3.29: Outward-facing citrate binding site of $SeCitS_{R428K}$ compared to the wild type. The top panels show the outward-facing citrate binding site of $SeCitS_{R428K}$ (A) and in $SeCitS_{WT}$ (B) with electron density for the substrates depicted as a mesh. The overlay of both structures (C), with the wild-type structure colored in grey, shows very little deviation between the structures.

In the inward-facing structure, the general overlay of the two structures is very similar (Figure 3.30). The helices and the location of the citrate superimpose between the wild-type structure and the SeCitS$_{R428K}$. The differences are in the orientation of side chains. The citrate in the first binding site seems to be more tightly coordinated in the native structure. This aligns with the observation that R402, which is also involved in coordinating the citrate in the outward-facing conformation, is angled in a different way not interacting with S405 but still coordinating the citrate. The mutated residue R428K is oriented in a downward manner compared to the wild-type protein. This might also be the reason that no secondary binding site of the citrate was observed for this structure.

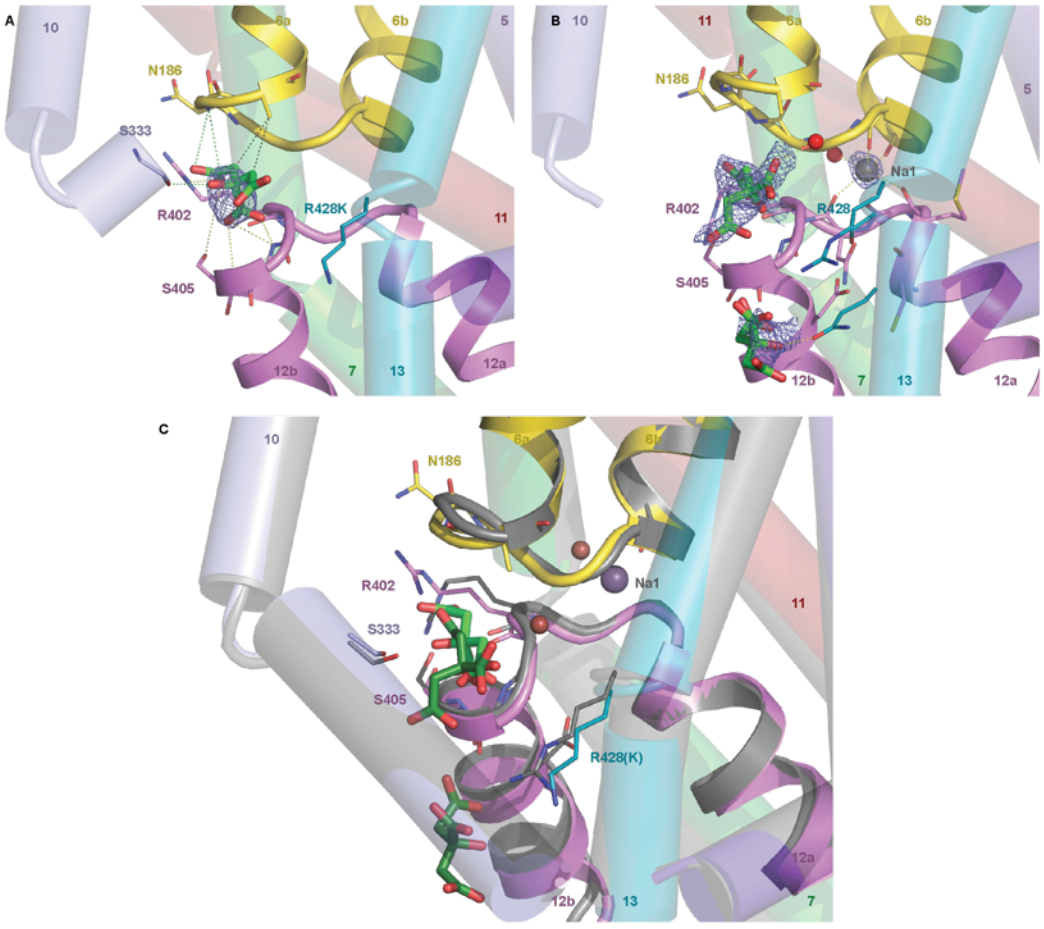

Figure 3.30: Citrate binding site of SeCitS$_{R428K}$ in the inward-facing conformation and its comparison to SeCitS$_{WT}$. The upper panels show the two citrate binding sites of SeCitS$_{R428K}$ (A) and SeCitS$_{WT}$ (B) with their respective electron densities for the substrates in the inward-facing conformation. The overlay (C) shows the slight shift of citrate out of the binding site in SeCitS$_{R428K}$ compared to the wild type. A secondary citrate, as seen in the wild type, is not unambiguously identified in the SeCitS$_{R428K}$ crystal structure.

The overall configuration of the dimers in the crystal is different from the wild type with one dimer in the symmetric inward conformation and one asymmetric dimer in a perpendicular arrangement to the other dimer. The difference to the wild type is the number of protomers in the outward- vs. inward-facing conformation, as the wild type has two asymmetric dimers in a unit cell. The interesting aspect is that this most prominent crystals packing for all mutants, represented here by $SeCitS_{R428K}$, is also present in SeMet SeCitS (Wöhlert *et al.*, 2015) and in KpCitS (Kim *et al.*, 2017). Considering that the crystal packing with both dimers in an asymmetric confirmation was rare for the native crystal, this finding begs the question if the transporter has a higher propensity towards a symmetric inward-facing conformation compared to an asymmetric confirmation as a resting state.

The crystal structure of $SeCitS_{R428K}$ compares in a number of properties to the wild-type protein. When only the same conformation (either inward- or outward-facing) are regarded, the RMSD is only about 0.52 Å between protomers of the mutant and the wild-type protein. There is also a certain degree of uncertainty concerning differences, as the overall resolution of the mutant structure is lower than the structure of the wild-type transporter. Nevertheless it is clear that the general arrangement in both conformations is very similar. In most cases the orientation of amino acids was the same as in the wild-type structure. There is a stretch of amino acids interconnecting the two domains of the protein that cannot be fitted into electron density, but the same stretch in the sequence is also missing in the wild-type structure. Several bound molecules were identified in both proteins such as a hydrophobic ligand at the interface between the protomers of the dimer, buffer substances on the periphery of the protein and the main substrate citrate binding in the general location that was also identified for the wild-type protein as described above. Deriving from the orientation of side chains and the backbone of the protein in the sodium binding site it is probable that the sodium ions may be bound in the same manner in the mutant as in the wild type. But a distinct electron density for neither the sodium ions nor the coordinated water could be identified in the refinement of the crystal structure.

The central aspect in the comparison of the two crystal structures is the substituted amino acid in position R428. The replacement of arginine by lysine does not result in a change in the overall charge of the sidechain, but brings along a change in the formation of hydrogen bonds extending from the positively charged nitrogen. This mainly results in a reduction in the amount of available sites for hydrogen bonds, as the delocalisation of the positive charge in the guanidinium moiety allows a multitude of binding opportunities. Additionally,

as the sidechain is also a little more extended compared to the arginine, the amine of the lysine might interact with other possible partners as well, which would occupy the possible citrate binding sites and thus not allow the binding of citrate in its intended manner. The citrate might still be able to bind the lysine, but would be too far out to be bound by N186, which would facilitate a proper coordination and alignment of the substrate for transport. The electron density for citrate in the mutant structure is not as well defined as in the wild-type protein, yet it is clear that the orientation of the citrate itself is different from the binding displayed in the native protein. In this respect it needs to be considered that concentration of citrate in the crystal is relatively high, so a binding at a local energetic minimum within the crystal structure does not equate with an ideal binding necessary for an initiation of transport.

4. CONCLUSION

In this work a combined structural and functional approach in gaining insights into the secondary active citrate transporter SeCitS of *Salmonella enterica* is taken to address different aspects of the transporter and its innate properties. Based on previous results concerning the transport properties and the crystal structure of the wild-type protein, a set of experiments was devised. One point of attention was the tight dimerization of the protein and its role in interdependence of the protomers and conformational distribution of the transporter. As the central aspect of this protein is its binding of the substrates citrate and sodium and their transport properties, experiments were devised to expand on this aspect. The crystal structure served as a valuable basis to select relevant residues for mutagenesis and explore their properties concerning structure and function.

Determining the binding and transport properties is one of the main objectives when working with a membrane transporter. The type of substrate of the transporter determines the experimental setup that can be employed to measure transport rates. SeCitS with citrate as its main substrate was measured with radioactively labeled carbon in the citrate in a filter assay. The main obstacle was the preparation of the proteoliposomes, which was overcome with rigorous monitoring of the lipids in the preparation process. The advantage in using this filter assay was the versatility in testing different conditions to allow a testing of a broad range of substances.

Isothermal titration calorimetry can be a powerful method to determine thermodynamic parameters of binding events (Freire, 2008). In this thesis, ITC was used as a means to study the binding of citrate and more specifically its pH-dependency as well as the binding of sodium as the second binding partner for SeCitS. The main challenge faced in all ITC experiments was the relatively low signal-to-reference ratio. In a lot of cases a strategy used to overcome those problems is to increase the concentration of protein in the cell. This approach was tested, but in the end led to a destabilization of the protein. The measurements had to be conducted under suboptimal conditions, leading to some vague results.

The ideal titration curve obtained during a measurement is sigmoidal, which features data points at both plateaus and also multiple points on the transition. This allows a very precise interpretation of the data as the inflection point can be precisely determined. The inflection

point represents the molar ratio indicating the stoichiometry of the binding, while the slope equates to the affinity in dependence of relative concentrations. The ratio of protein concentration and affinity is defined as the c-value, which allows an initial estimation of the quality of the titration (Turnbull & Daranas, 2003). Some titrations carried out in this thesis were limited by the protein concentration accompanied by low affinities to result in a too shallow course of the titration curve. In this light, the definitive result that can be deducted from the titrations of wild-type protein with isocitrate is that the affinity is below 200 µM. The same is true for the mutants measured with citrate and isocitrate. The titration curve of SeCitS with sodium and especially with a subsequent citrate titration showed a very intriguing result in terms of binding mode. Considering structural details on the sodium binding sites, such as the presence and close proximity of two sodium ions within the monomer and the occlusion of the binding sites by a citrate binding in its high-affinity binding site, this underlines the dependence in sodium and citrate binding within a protomer. Furthermore the low Hill coefficient in citrate titrations shows a certain interdependence within the dimer.

Another part of the thesis addressed the potential dependence of the protomers on one another. The experimental approach included a mutation strategy where the deactivation and halting of one protomer could shed light on the activity of an isolated protomer. An independent transport of substrates would have been able to prove or disprove interdependence within the dimer, but as the experimental limits were reached no certain answer was possible here.

In light of the results from Section 3.1, it could be interesting to combine the results obtained from the mutation studies with the question for the transport activity of the isolated monomer. To tackle the question of interdependence in a functional way a similar approach to the cross-link strategy employed in this thesis in forming a semi-functional, albeit conformationally undefined, heterodimer could be used. One protomer in the dimer could be exchanged for one of the inactive point mutants tested in this thesis ($SeCitS_{R428A}$/$SeCitS_{R402A}$), while the other protomer retains its wild-type sequence. A co-transformation of the wild type and a mutant with no transport activity to obtain hybrid dimers could help in understanding if the monomers act individually or in a concerted manner, depending on the relative transport activity of the hybrid dimer being above or below 50% compared to a wild-type dimer.

The crystal structure of $SeCitS_{R428K}$ was solved at 3.3 Å in this thesis. The wild-type structure was solved to 2.5 Å. Overall, the comparison of the two structures indicates that there is only a very subtle difference between the two forms. The RMSD is low at only 0.52 Å. The central differences are the orientation of some amino acids, especially in locations where the electron density at the present resolution leaves room for variance and in the binding site where the mutation is located. The general arrangement of the substrate binding sites is similar with the exception of the relatively longer lysine, which also moves the citrate from its position in the wild-type protein into a different arrangement. This is true for the high-affinity binding site in the outward-facing conformation and the inward-facing conformation where no clear electron density is found for the citrate.

The observation that the crystal structures are so similar gives rise to the question why the transporter shows such a dramatic change in transport and in binding of its substrate although it is a very conservative mutation as the charge of the amino acid is not changed. The reason has to lie in the geometry by which the substrate is bound when the bulkier guanidinium tail in arginine is exchanged to the slightly extended amine in lysine. It is possible that the change in orientation in the citrate, with the hydroxyl group switching from facing towards its binding site to outwards, changes the significant interactions in the same way that isocitrate in high concentrations is able to occupy the citrate binding site and inhibit citrate transportation.

As detailed in Section 3.5, the high-level difference between the crystal structures of the mutant and the wild-type protein was the conformational distribution. The crystal structure of the wild type was solved with both dimers in the unit cell in asymmetric conformations with each one outward-facing and one inward-facing protomer. On the other hand the crystal structure of the R428K mutant crystalized with one symmetric inward-facing dimer and one asymmetric dimer. The same applies to the SeMet-SeCitS protein used for phasing of the native structure, other mutants as predicted by space group and unit cell dimensions and the crystal structure of the KpCitS. This observation could suggest that the asymmetric conformation is a stable but not completely favorable conformation for the dimer.

There is a number of examples of proteins in general and transporters specifically that show how multimerization of proteins offers a number of structural and functional opportunities. The assembly of protomers allows for better stability, the formation of substrate-binding sites or translocation channels, regulation of function and trafficking (Alguel *et al.*, 2016). In

SeCitS it can be speculated that the dimerization contributes substantially to the stability of the transporter within its membrane environment. The conformational change is relatively large with a movement of 31° around an axis perpendicular to the membrane. The movement of the domains relative to one another, as observed in other elevator-type transporters, is either smaller or the relative movement of the domains against one another is different (Garaeva & Slotboom, 2020). In other monomeric and multimeric transporters that employ an elevator-type mechanism some strategies to avoid breaching the boundaries of the lipid bilayer are described. An underlying aspect is the more limited extent of the movement itself in alike transporters and thus the issue of protrusion is not as prominent. Nevertheless, avoidance strategies of the protrusion from the membrane include a motion not limited to the transport domain, but the static domain also shifts in a compensatory motion (Zhou *et al.*, 2014), the tilting and thinning of the adjacent membrane that can go as far as a distortion of the surrounding membrane (Drew & Boudker, 2016), or a higher oligomeric state as a trimer that could compensate for the movement of one of its protomers without impacting the protomer independence (Erkens *et al.*, 2013).

This information leads to another objective of this thesis, namely the elucidation of conformational distribution of protomers within the dimer in a near-native environment. In the end this was not possible, due to experimental restrictions that could not be overcome. Even though cryo-EM of smaller proteins proves to be a powerful method in a number of questions related to structure and structural changes within a protein, it is not without challenge. Relevant results emerge from the interplay of careful sample preparation, deliberate parameter selection for image acquisition and skilful computational analysis. In the case of SeCitS it is still open whether the isolation of different conformations through computational classification is possible as the protruding part from the membrane is small in relation to the whole protein. Here it may be advantageous for achieving the initial that the transition motion of SeCitS is comparably large.

Nevertheless it is possible to speculate on the distribution and the relative stability, as a number of experimental results contribute to a working hypothesis of how the transporter dwells and operates in the membrane. Beside the structural indications towards a preference for the symmetric inward-facing conformation, the main pointer in this direction was the low Hill coefficient in all determinations. With the numbers consistently low, the experiments show that not even half of the available protomers bind a citrate molecule in their respective high-affinity binding site in the outward-open conformation. Given that this

high-affinity binding site is only available and accessible in half of all protomers, it is clear that the symmetric outward-open state is improbable. Therefore it is a valid hypothesis that this occurs as the protein is predominantly present in the asymmetric form or even as the idle symmetrical inward-facing conformation. Only one protomer would go through a transport cycle while the second protomer would serve as an elaborate membrane anchor.

Besides the potential ways forward already mentioned, this re-emerging hypothesis could be tested by molecular dynamics simulation of the dimer in a lipid bilayer. This approach was taken to analyze Glt_{Ph} in a lipid environment (Zhou *et al.*, 2019). There, the bilayer adapts differently around the protein depending on the conformation of the protomer within the trimer. While the outward-facing conformation induces only small membrane deformation, the inward-facing protomers strongly bend the membrane around the protein. It is not yet elucidated how the energetic impact of such a deformation would be balanced. Based on the results in this thesis, an initial worst-case consideration could be the modeling of the symmetric outward-facing protein embedded in the membrane. With an appropriate level of coarse graining in the setup of the model, the stability of this configuration of the protomers in the dimer could be challenged. Those results would have to be compared to the equivalent system with an asymmetric model and the symmetric inward-facing protein in a membrane.

The three aspects of study investigated in this thesis were binding, transport and structure. The results for binding parameters, transport activities and the correlation to structural investigations paints a more detailed picture of the citrate transporter SeCitS, which provide additional data in painting a cohesive picture of the transport cycle in secondary active transporters and beyond.

REFERENCES

Abramson J & Wright EM (2009). Structure and function of Na+-symporters with inverted repeats. *Current Opinion in Structural Biology* **19:** 425–432.

Alguel Y, Cameron AD, Diallinas G & Byrne B (2016). Transporter oligomerization: form and function. *Biochemical Society Transactions* **44:** 1737–1744.

Bakheet TM & Doig AJ (2009). Properties and identification of human protein drug targets. *Bioinformatics* **25:** 451–457.

Bandell M, Ansanay V, Rachidi N, Dequin S & Lolkema JS (1997). Membrane Potential-generating Malate (MleP) and Citrate (CitP) Transporters of Lactic Acid Bacteria Are Homologous Proteins. *Journal of Biological Chemistry* **272:** 18140–18146.

Bandell M & Lolkema JS (2000). Arg-425 of the Citrate Transporter CitP Is Responsible for High Affinity Binding of Di- and Tricarboxylates. *Journal of Biological Chemistry* **275:** 39130–39136.

Bott M, Meyer M & Dimroth P (1995). Regulation of anaerobic citrate metabolism in Klebsiella pneumoniae. *Molecular Microbiology* **18:** 533–546.

Busch W & Saier MH (2004). The IUBMB-Endorsed Transporter Classification System. *Molecular Biotechnology* **27:** 253–262.

Caffrey M & Cherezov V (2009). Crystallizing membrane proteins using lipidic mesophases. *Nature Protocols* **4:** 706–731.

Canela EI, Navarro G, Beltrán JL & Franco R (2019). The meaning of the Michaelis-Menten constant: K m describes a steady-state. *bioRxiv*608232.

Carpenter MC & Wilcox DE (2014). Thermodynamics of formation of the insulin hexamer: Metal-stabilized proton-coupled assembly of quaternary structure. *Biochemistry* **53:** 1296–1301.

Chen Y-J, Pornillos O, Lieu S, Ma C, Chen AP & Chang G (2007). X-ray structure of EmrE supports dual topology model. *Proceedings of the National Academy of Sciences* **104:** 18999–19004.

Cho I, Jackson MR & Swift J (2016). Roles of Cross-Membrane Transport and Signaling in the Maintenance of Cellular Homeostasis. *Cellular and Molecular Bioengineering* **9:** 234–246.

Dobrowolski A & Lolkema JS (2009). Functional Importance of GGXG Sequence Motifs in Putative Reentrant Loops of 2HCT and ESS Transport Proteins. *Biochemistry* **48:** 7448–7456.

Drew D & Boudker O (2016). Shared Molecular Mechanisms of Membrane Transporters. *Annual Review of Biochemistry* **85:** 543–572.

Emsley P, Lohkamp B, Scott WG & Cowtan K (2010). Features and development of Coot. *Acta Crystallographica Section D Biological Crystallography* **66:** 486–501.

Engel A & Gaub HE (2008). Structure and Mechanics of Membrane Proteins. *Annual Review of Biochemistry* **77:** 127–148.

Van Den Ent F & Löwe J (2006). RF cloning: A restriction-free method for inserting target genes into plasmids. *Journal of Biochemical and Biophysical Methods* **67:** 67–74.

Erkens GB, Hänelt I, Goudsmits JMH, Slotboom DJ & van Oijen AM (2013). Unsynchronised subunit motion in single trimeric sodium-coupled aspartate transporters. *Nature* **502:** 119–123.

Evans PR & Murshudov GN (2013). How good are my data and what is the resolution? *Acta Crystallographica Section D Biological Crystallography* **69:** 1204–1214.

Fairman JW, Noinaj N & Buchanan SK (2011). The structural biology of β-barrel membrane proteins: a summary of recent reports. *Current Opinion in Structural Biology* **21:** 523–531.

Forrest LR, Krämer R & Ziegler C (2011). The structural basis of secondary active transport mechanisms. *Biochimica et Biophysica Acta (BBA) - Bioenergetics* **1807:** 167–188.

Fox JM, Zhao M, Fink MJ, Kang K & Whitesides GM (2018). The Molecular Origin of Enthalpy/Entropy Compensation in Biomolecular Recognition. *Annual Review of Biophysics* **47:** 223–250.

Freire E (2008). A new era for microcalorimetry in drug development. *American Pharmaceutical Review*.

Garaeva AA & Slotboom DJ (2020). Elevator-type mechanisms of membrane transport. *Biochemical Society Transactions* **48:** 1227–1241.

Gopal E, Miyauchi S, Martin PM, Ananth S, Srinivas SR, Smith SB, Prasad PD & Ganapathy V (2007). Expression and functional features of NaCT, a sodium-coupled citrate transporter, in human and rat livers and cell lines. *American Journal of Physiology-Gastrointestinal and Liver Physiology* **292:** G402–G408.

Goswami P, Paulino C, Hizlan D, Vonck J, Yildiz Ö & Kühlbrandt W (2011). Structure of the archaeal Na + /H + antiporter NhaP1 and functional role of transmembrane helix 1. *The EMBO Journal* **30:** 439–449.

Gouaux E & MacKinnon R (2005). Principles of selective ion transport in channels and pumps. *Science* **310:** 1461–1465.

Grant T, Rohou A & Grigorieff N (2018). CisTEM, user-friendly software for single-particle image processing. *eLife*; DOI: 10.7554/eLife.35383.

Grötzinger MJ (2014). Biochemical Characterization of the secondary Transporter SeCitS from Salmonella enterica (Thesis). *Max-Planck-Institut für Biophysik*.

Hanahan D (1983). Studies on transformation of Escherichia coli with plasmids. *Journal of Molecular Biology* **166:** 557–580.

Hedin LE, Illergård K & Elofsson A (2011). An introduction to membrane proteins. *Journal of Proteome Research* **10:** 3324–3331.

Hinz A & Tampé R (2012). ABC transporters and immunity: Mechanism of self-defense. *Biochemistry* **51:** 4981–4989.

Ter Horst R & Lolkema JS (2012). Membrane topology screen of secondary transport proteins in structural class ST[3] of the MemGen classification. Confirmation and structural diversity. *Biochimica et Biophysica Acta - Biomembranes* **1818:** 72–81.

Huard K et al. (2015). Discovery and characterization of novel inhibitors of the sodium-coupled citrate transporter (NaCT or SLC13A5). *Scientific Reports* **5:** 17391.

Hucho F & Weise C (2001). Ligand-gated ion channels. *Angewandte Chemie - International Edition* **40:** 3100–3116.

Inoue K, Zhuang L & Ganapathy V (2002). Human Na+-coupled citrate transporter: primary structure, genomic organization, and transport function. *Biochemical and Biophysical Research Communications* **299:** 465–471.

Ishiguro N, Izawa H, Shinagawa M, Shimamoto T & Tsuchiya T (1992). Cloning and nucleotide sequence of the gene (citC) encoding a citrate carrier from several Salmonella serovars. *Journal of Biological Chemistry* **267:** 9559–9564.

Jardetzky O (1966). Simple Allosteric Model for Membrane Pumps. *Nature* **211:** 969–970.

Jencks WP (1989). [7] Utilization of binding energy and coupling rules for active transport and other coupled vectorial processes. In *Methods in Enzymology*, pp. 145–164.

Jiang T, Wen P-C, Trebesch N, Zhao Z, Pant S, Kapoor K, Shekhar M & Tajkhorshid E (2020). Computational Dissection of Membrane Transport at a Microscopic Level. *Trends in Biochemical Sciences* **45:** 202–216.

Kabsch W, T. BA, K. D, A. KP, K. D, S. M, G. RRB, P. E, S. F, K. W, W. K, W. K, W. K, W. K, P. K & S. WM (2010). *XDS*. *Acta Crystallographica Section D Biological Crystallography* **66:** 125–132.

Kebbel F (2013). Structural and Functional Characterization of the Integral Membrane Proteins CitS and CCR5 by Electron Microscopy. Inauguraldissertation (Thesis). *Universität Basel*. https://edoc.unibas.ch/27823/1/PhD_Thesis_Fabian__Kebbel.pdf

Kebbel F, Kurz M, Arheit M, Grütter MG & Stahlberg H (2013). Structure and substrate-induced conformational changes of the secondary citrate/sodium symporter CitS revealed by electron crystallography. *Structure* **21:** 1243–1250.

Kebbel F, Kurz M, Grütter MG & Stahlberg H (2012). Projection structure of the secondary citrate/sodium symporter CitS at 6 Å Resolution by electron crystallography. *Journal of Molecular Biology* **418:** 117–126.

Kim JW, Kim S, Kim S, Lee H, Lee J-O & Jin MS (2017). Structural insights into the elevator-like mechanism of the sodium/citrate symporter CitS. *Scientific Reports* **7:** 2548.

Klatt L (2017). Strukturelle und funktionelle Charakterisierung von SeCitS über LCP-Kristallisation und isothermale Titrationskaloriemetrie (Thesis). *Max-Planck-Institut für Biophysik*.

Krishnamurthy H, Piscitelli CL & Gouaux E (2009). Unlocking the molecular secrets of sodium-coupled transporters. *Nature* **459:** 347–355.

Lafont V, Armstrong AA, Ohtaka H, Kiso Y, Mario Amzel L & Freire E (2007). Compensating enthalpic and entropic changes hinder binding affinity optimization. *Chemical Biology and Drug Design* **69:** 413–422.

Laskowski RA & Swindells MB (2011). LigPlot+: Multiple Ligand–Protein Interaction Diagrams for Drug Discovery. *Journal of Chemical Information and Modeling* **51:** 2778–2786.

Li C & Wang W (2017). Molecular biology of aquaporins. In *Advances in Experimental Medicine and Biology*, pp. 1–34. *Springer New York LLC*.

Liebschner D et al. (2019). Macromolecular structure determination using X-rays, neutrons and electrons: Recent developments in Phenix. *Acta Crystallographica Section D: Structural Biology* **75:** 861–877.

Lolkema JS (2006). Domain Structure and Pore Loops in the 2-Hydroxycarboxylate Transporter Family. *Journal of Molecular Microbiology and Biotechnology* **11:** 318–325.

Lolkema JS, Enequist H & van der Rest ME (1994). Transport of citrate catalyzed by the sodium-dependent citrate carrier of Klebsiella pneumoniae is obligatorily coupled to the transport of two sodium ions. *European Journal of Biochemistry* **220:** 469–475.

Lolkema JS & Slotboom DJ (1998). Estimation of structural similarity of membrane proteins by hydropathy profile alignment. *Molecular Membrane Biology* **15:** 33–42.

Luckey M (2008). Proteins in or at the Bilayer. In *Membrane Structural Biology*, pp. 68–101. *Cambridge University Press*, *Cambridge*.

Mancusso R, Gregorio GG, Liu Q & Wang D-N (2012). Structure and mechanism of a bacterial sodium-dependent dicarboxylate transporter. *Nature* **491:** 622–626.

Martens S & Fracchiolla D (2020). Activation and targeting of ATG8 protein lipidation. *Cell Discovery* **6:** 23.

Morth JP, Pedersen BP, Buch-Pedersen MJ, Andersen JP, Vilsen B, Palmgren MG & Nissen P (2011). A structural overview of the plasma membrane Na+,K +-ATPase and H+-ATPase ion pumps. *Nature Reviews Molecular Cell Biology* **12:** 60–70.

Murshudov GN, Skubák P, Lebedev AA, Pannu NS, Steiner RA, Nicholls RA, Winn MD, Long F & Vagin AA (2011). REFMAC5 for the refinement of macromolecular crystal structures. *Acta Crystallographica Section D: Biological Crystallography* **67:** 355–367.

Pao SS, Paulsen IT & Saier MH (1998). Major Facilitator Superfamily. *Microbiology and Molecular Biology Reviews* **62:** 1–34.

Perez C, Khafizov K, Forrest LR, Krämer R & Ziegler C (2011). The role of trimerization in the osmoregulated betaine transporter BetP. *EMBO reports* **12:** 804–810.

Pettersen EF, Goddard TD, Huang CC, Couch GS, Greenblatt DM, Meng EC & Ferrin TE (2004). UCSF Chimera - A visualization system for exploratory research and analysis. *Journal of Computational Chemistry* **25:** 1605–1612.

Pos KM, Bott M & Dimroth P (1994). Purification of two active fusion proteins of the Na+-dependent citrate carrier of Klebsiella pneumoniae. *FEBS Letters* **347:** 37–41.

Pos KM & Dimroth P (1996). Functional properties of the purified Na+-dependent citrate carrier of Klebsiella pneumoniae: Evidence for asymmetric orientation of the carrier protein in proteoliposomes. *Biochemistry* **35:** 1018–1026.

Pudlik AM & Lolkema JS (2012). Substrate Specificity of the Citrate Transporter CitP of Lactococcus lactis. *Journal of Bacteriology* **194:** 3627–3635.

Quinn CF, Carpenter MC, Croteau ML & Wilcox DE (2016). Isothermal Titration Calorimetry Measurements of Metal Ions Binding to Proteins. In *Methods in Enzymology*, pp. 3–21. *Academic Press Inc.*

Rajarathnam K & Rösgen J (2014). Isothermal titration calorimetry of membrane proteins - progress and challenges. *Biochimica et biophysica acta* **1838:** 69–77.

Reyes N, Ginter C & Boudker O (2009). Transport mechanism of a bacterial homologue of glutamate transporters. *Nature* **462:** 880–885.

Saier MH (2000). A Functional-Phylogenetic Classification System for Transmembrane Solute Transporters. *Microbiology and Molecular Biology Reviews* **64:** 354–411.

Schieferdecker A (2016). Site Directed Crosslinking Studies on the SeCitS Transport Mechanism (Thesis). *Max-Planck-Institut für Biophysik*.

Schrödinger LLC (2015). *The PyMOL Molecular Graphics System, Version 2.0*.

Smith AW (2012). Lipid-protein interactions in biological membranes: A dynamic perspective. *Biochimica et Biophysica Acta - Biomembranes* **1818:** 172–177.

Sobczak I & Lolkema JS (2005*a*). The 2-Hydroxycarboxylate Transporter Family: Physiology, Structure, and Mechanism. *Microbiology and Molecular Biology Reviews* **69:** 665–695.

Sobczak I & Lolkema JS (2005*b*). Loop VIII/IX of the Na + -Citrate Transporter CitS of Klebsiella pneumoniae Folds into an Amphipathic Surface Helix. *Biochemistry* **44:** 5461–5470.

Stillwell W (2013). Membrane Lipids. In *An Introduction to Biological Membranes*, pp. 43–56. *Elsevier*.

Thomson JA & Ladbury JE (2004). *Biocalorimetry 2*ed. Ladbury JE & Doyle ML. *John Wiley & Sons, Ltd*, *Chichester, UK*.

Tsai CJ & Ziegler C (2010). Coupling electron cryomicroscopy and X-ray crystallography to understand secondary active transport. *Current Opinion in Structural Biology* **20:** 448–455.

Turnbull WB & Daranas AH (2003). On the Value of c : Can Low Affinity Systems Be Studied by Isothermal Titration Calorimetry? *Journal of the American Chemical Society* **125:** 14859–14866.

Wei Y, Guffanti AA, Ito M & Krulwich TA (2000). Bacillus subtilis YqkI is a novel malic/Na+-lactate antiporter that enhances growth on malate at low protonmotive force. *Journal of Biological Chemistry* **275:** 30287–30292.

White S (2020). *mpstruc* https://blanco.biomol.uci.edu/mpstruc/

Willmes DM & Birkenfeld AL (2013). The role of INDY in metabolic regulation. *Computational and Structural Biotechnology Journal* **6:** e201303020.

Winn MD, Ballard CC, Cowtan KD, Dodson EJ, Emsley P, Evans PR, Keegan RM, Krissinel EB, Leslie AGW, McCoy A, McNicholas SJ, Murshudov GN, Pannu NS, Potterton EA, Powell HR, Read RJ, Vagin A & Wilson KS (2011). Overview of the CCP4 suite and current developments. *Acta Crystallographica Section D: Biological Crystallography* **67:** 235–242.

Wiseman T, Williston S, Brandts JF & Lin LN (1989). Rapid measurement of binding constants and heats of binding using a new titration calorimeter. *Analytical Biochemistry* **179:** 131–137.

Wittig I, Braun HP & Schägger H (2006). Blue native PAGE. *Nature Protocols* **1:** 418–428.

Wöhlert D, Grötzinger MJ, Kühlbrandt W & Yildiz Ö (2015). Mechanism of Na+-dependent citrate transport from the structure of an asymmetrical CitS dimer. *eLife* **4:** e09375.

Wöhlert D, Kühlbrandt W & Yildiz Ö (2014). Structure and substrate ion binding in the sodium/proton antiporter PaNhaP. *eLife*; DOI: 10.7554/eLife.03579.

Wright EM (1993). The Intestinal Na+/Glucose Cotransporter. *Annual Review of Physiology* **55:** 575–589.

Zhou W, Fiorin G, Anselmi C, Karimi-Varzaneh HA, Poblete H, Forrest LR & Faraldo-Gómez JD (2019). Large-scale state-dependent membrane remodeling by a transporter protein. *eLife*; DOI: 10.7554/eLife.50576.

Zhou X, Levin EJ, Pan Y, McCoy JG, Sharma R, Kloss B, Bruni R, Quick M & Zhou M (2014). Structural basis of the alternating-access mechanism in a bile acid transporter. *Nature* **505:** 569–573.

LIST OF TABLES

LIST OF FIGURES

CONTRIBUTIONS

Except where stated otherwise by reference, acknowledgment or in the following section, the work presented was generated by myself under the supervision of my advisors during my doctoral studies.

During my doctoral studies I supervised two bachelor students Laura Matzner and Lisa Klatt and one master Anne Schieferdecker. Project design and planning were done by me. The experiments performed within the scope of their thesis were performed by them and analyzed and interpreted together. The constructs used in this study were designed by me, with the exception of the wild-type SeCitS, which was provided by David Wöhlert. Cloning, expression and purification was performed by me or by students at the time. Transport assays were performed by me, except for cysteine mutants by Anne Schieferdecker as mentioned in 3.1.3. Optimization of Saposin and Nanodisc reconstitution was performed by Lisa Klatt. Negative stain EM final staining and imaging was performed by Susann Kaltwasser. Cryo-EM was performed in collaboration with Arne Möller who prepared the grids and did the data collection. Analysis of the datasets was performed by me. Initial ITC trials were performed by Laura Matzner. Optimization of sodium titrations was performed by Lisa Klatt. Mutants of SeCitS were partly crystallized by Laura Matzner. Crystal data collection, processing and refinement were performed in close guidance of Özkan Yildiz.

Whenever a figure, table or text is identical to a previous publication, reference is given and copyright permission has been obtained.

Parts of the thesis have been previously presented as poster “Functional and structural insights into the citrate transporter CitS” (10th Transport Colloquium, GBM, 2016, Rauischholzhausen) and published in “Mechanism of Na^+-dependent citrate transport from the structure of an asymmetrical CitS dimer” (Wöhlert D, Grötzinger MJ, Kühlbrandt W & Yildiz Ö, 2015, eLife 4: e09375).